UNIVERSITÀ DEGLI STUDI DI PARMA

Facoltà di Scienze Matematiche Fisiche Naturali

Dipartimento di Fisica

$L1_0$-Ordered Systems and Exchange-Spring Magnets with Perpendicular Anisotropy

Thesis submitted for the award of the degree of Ph.D. in Physics

Dottorato di Ricerca in Fisica

Roberta Ciprian

Supervisor:

Prof. Massimo Carbucicchio

XXI Ciclo - Parma, January 2009

Contents

Introduction

Nanostructured magnetic films and multilayers display peculiar properties which proved to be very interesting from both theoretical and technological points of view. The possibility of tailoring the magnetic properties of such materials through the microstructure and growth engineering at the nanometric scale gives new challenges in the field of material science.

In particular, in the field of micro-electromechanical systems (MEMS), permanent magnets and recording devices, particular attention is addressed to the development of systems constituted by exchange-coupled soft and hard magnetic phases, showing a single phase magnetic behaviour. Combining the high coercivity of the hard phase and the high value of the saturation magnetization of the soft one it is possible to strongly enhance the maximum energy product $(BH)_{max}$.

A considerable research activity has been addressed to investigate the structural and magnetic properties of nanocomposites where $L1_0$-ordered films of FePt, FePd, or CoPt, constitute the hard phase. In effect, these intermetallic compounds are characterized by a high temperature structural transformation that determines a distortion of the lattice from cubic to tetragonal ($L1_0$ phase) with the appearance of a strong magnetocrystalline anisotropy along the contracted axis (*c*-axis). If grown in the form of thin films, the use of particular substrates, bufferlayers and the optimization of growth parameters can induce a preferred orientation of the *c*-axis along the normal to the surface, giving rise to a strong perpendicular magnetic anisotropy. Thanks to this strong anisotropy, that induces a high thermal stability, the $L1_0$-ordered phase is very useful for the development of *perpendicular exchange-spring type magnets.*

The subject of this thesis is the preparation and characterization of FePt and FePd thin films showing a strong perpendicular anisotropy thanks to the establishing of a good chemical $L1_0$ order. Starting from these hard films, exchange-spring magnets in the form of bilayers and trilayers have been grown and studied.

The main points investigated during the Ph.D. period concerns:

- The comparison of different growing techniques, the rf sputtering and the e-beam evaporation, for the development of FePt and FePd films showing a strong perpendicular anisotropy.
- The effects, on the magnetic and structural properties of FePt and FePd films, of the annealing processes performed during or after the grown, of a Pt underlayer and of the alloy thickness.
- The growth of $L1_0$-ordered FePt and FePd ultra-thin films using the e-beam evaporation technique. In this ultra-thin regime, the magnetic properties are strongly influenced by interface and surface phenomena, which can be exploited for the development of perpendicular exchange-spring magnets with high soft/hard thickness ratio.
- The possibility to grown exchange-coupled hard/soft bilayers, using different growing techniques, i.e. the rf sputtering for the deposition of the hard phase and the e-beam evaporation technique for the growth of the soft one.
- The study of hard/soft interface phenomena and their relation with the development of a strong exchange coupling between different magnetic phases.

Chapter 1

Basic Ideas of Magnetism

In ferromagnetic materials, individual atoms have a net magnetic moment due to the unbalanced electron spins, as for the paramagnetism. Below a critical temperature, the Curie temperature T_c, cooperative interatomic exchange forces maintain neighbouring atoms parallel, giving rise to a spontaneous magnetization without inducing a macroscopic magnetization. In effect, the material arranges itself in a domain structure, i.e. regions spontaneously magnetized to the saturation value M_s, each one having a different orientation of the magnetization vector. This domain structure is a direct consequence of the balance among the various contributions to the energy: exchange, anisotropy, and magnetostatic[1-3].

1.1 Exchange Energy

The existence of a spontaneous magnetization with a particular direction can be explained only through the presence of a spin-spin exchange interaction having quantum-mechanical origin that is a direct consequence of the *Pauli Exclusion Principle*. In effect the requirement that the electronic wave functions be antisymmetric makes the energy eigenvalues depending on the relative spin orientations of the electrons. This effect can be interpreted in term of an electrostatic interaction between electron clouds which tends to orient the spin angular moments and consequently the magnetic moments over macroscopic distances.

The *exchange energy* can be expressed as:

$$E_{ex} = -2J_{ij}\vec{S}_i \cdot \vec{S}_j \tag{1.1}$$

where J_{ij} is the nearest neighbour exchange integral that describes the coupling between two ions and $\vec{S}_i$ is the total spin angular moment describing the magnetic ions. A positive value of J_{ij} favours a parallel spin alignment. The exchange forces depend mainly on interatomic distances and not on any geometrical regularity of atom positions.

By considering two ions and $\vec{S}_i$ as classical vectors, it is possible to define a phenomenological constant called *exchange stiffness constant*:

$$A \approx kJS^2 / a \tag{1.2}$$

where *a* is the lattice constant and *k* is a numeric factor depending on the lattice symmetry. This constant, of the order of 10^{-11} J/m, depends on the material and gives the strength of the short-range exchange interaction, i.e. it is a measure of the torque stiffness of the spin-spin coupling. The *exchange-length* $l_{ex} = \sqrt{A / \mu_0 M_s^2}$ is then the length below which atomic exchange interactions dominate typical magnetostatic effects.

1.2 Magnetic Anisotropy Energy

The magnetic anisotropy represents the dependence of the macroscopic magnetic properties on the crystal structure. In particular, a crystalline ferromagnet in most cases presents an easy direction for the spontaneous magnetization, i.e. a direction along which the magnetization vector is spontaneously aligned in the absence of other constrains. This makes the magnetization process anisotropic, because the energy required to magnetize the material depends on the applied magnetic field direction with respect to the crystallographic axis. The energy contribution that depends on the direction between the magnetization vector and the symmetry axes is called *anisotropy energy*.

There are several kinds of anisotropy: magnetocrystalline, shape, exchange, surface and interface, induced by stress, plastic deformations, thermal annealing, magnetic field or irradiation. Of these, only the magnetocrystalline anisotropy is an intrinsic property of the material, the others are induced by the growing technique or by the treatments done on the materials.

The microscopic origin of the anisotropy is linked to the spin state and to the atomic configuration. In effect the spin state gives rise to a dipolar interaction responsible of the shape anisotropy, while the atomic configuration is at the origin of the magnetocrystalline and stress anisotropy.

1.2.1 Magnetocrystalline Anisotropy

The microscopic origin of the *magnetocrystalline anisotropy* mainly lies in the spin-orbit interaction and its relation with the electric field creates by the crystallographic lattice. When an external field tries to reorient the spin of an electron, the orbit of that electron also tends to be reoriented. But the orbit is strongly coupled to the lattice and therefore resists the attempt to rotate the spin axis. In a ferromagnetic material, the most important contribution to the moment is due to the electronic spin moments, and only a minor contribution derives from the orbital moments because of the partial quenching of the orbital magnetic moment.

The anisotropy energy required to rotate the spin moments away from the easy direction, the *anisotropy energy*, is just the energy required to overcome both the spin-orbit interaction and the orbit-lattice coupling. In rare-earth elements, the spin-orbit interaction is stronger than the crystal field and the intensity of the anisotropy is quantified by spin-orbit interaction, on the contrary in a 3d transition metal the crystal field dominates the spin-orbit interaction and the anisotropy is mainly due to the crystal-lattice coupling.

A phenomenological representation of the anisotropy energy can be made by a power expansion in the cosine direction of $\vec{M}_s$ with respect to the crystallographic axes. In the case of a crystal with cubic symmetry, the anisotropy energy density can be written as:

$$E_a = K_0 + K_1\left(\alpha_1^2\alpha_2^2 + \alpha_2^2\alpha_3^2 + \alpha_3^2\alpha_1^2\right) + K_2\left(\alpha_1^2\alpha_2^2\alpha_3^2\right) + ... \qquad (1.3)$$

where α_i represent the direction cosines of M_s with respect to the crystallographic axes and the K_i coefficients, expressed in ergs/cm^3, are the *magnetic anisotropy constants*. These are temperature dependent and characteristics of each material.

The analysis of E_a as a function of the K_i, allows to identify the easy and hard magnetization direction of the magnet. In effect if $K_2 = 0$ and $K_1 > 0$ the (100) direction is the easy direction while for $K_1 < 0$ the (111) direction is the easiest one.

In the case of an uniaxial system with hexagonal symmetry the anisotropy energy density becomes:

$$E_a = K_0 + K_1 \sin^2\theta + K_2 \sin^4\theta + ... \qquad (1.4)$$

where θ is the angle that the magnetization vector forms with the *c*-axis. In this case, the anisotropy symmetry is defined not only by the sign of K_1 but also by the sign of K_1 / K_2.

In effect if $K_1 > 0$ and $K_2 > -K_1$, the E_a has a minimum for $\theta = 0°$ and the *c*-axis is the easy magnetization axis. If the minimum occurs for $\theta = 90°$, the basal plane of the crystal is an easy plane of magnetization and the *c*-axis becomes a hard direction. Moreover, the minimum can

occur for an intermediate direction $\theta = \arcsin\sqrt{-K_1/(2K_2)}$ that does not coincide with any particular crystallographic axis and represents a cone with the symmetry axis along the *c*-axis. In this case the magnetization vector may lie anywhere on the surface of a cone with a semivertex angle of θ. In Fig. 1.1(a) a schematic representation of the easy magnetization axis, plane and cone, and in Fig. 1.1(b) the results obtained for a hexagonal crystal summarized in a typical *magnetic phase diagram.*

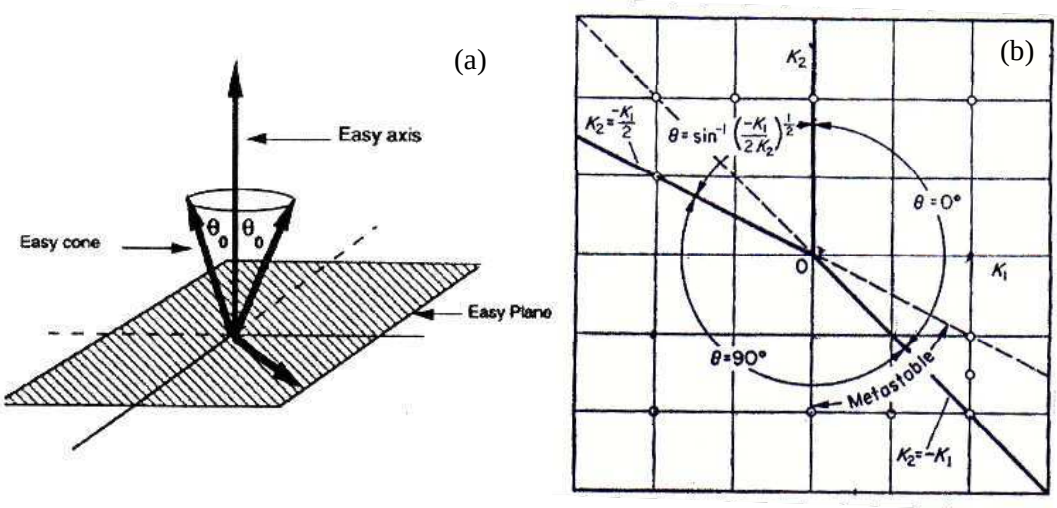

Figure 1.1 - (a) Schematic representation of the easy magnetization axis, plane and cone and (b) magnetic phase diagram obtained for an uniaxial crystal with hexagonal symmetry[1].

1.2.2 Shape Anisotropy and the Magnetostatic Energy

Samples having non spherical shape have easy axes that are determined also by their geometrical characteristics. This phenomenon is due to the presence of the *demagnetizing field* H_d arising from the free poles that form on the magnetized sample surfaces giving rise to long range dipolar interactions. In the expression of the total free energy that characterized the system, a new contribution must be taken into account, the *magnetostatic energy* or *self-energy* of the magnet that can be expressed (per unit volume) as:

$$E_{ms} = -\frac{1}{2}\vec{H}_d \cdot \vec{M} \text{ (ergs/cm}^3\text{)}; \tag{1.5}$$

The negative sign in the right hand of the equation indicates that the demagnetizing field is opposing and reduces the magnetization of the sample. The intensity of this field is proportional to the magnetization and is always lower than $4\pi M_s$ value. It can be expressed as

$$H_d = -\vec{N}_d \cdot \vec{M} \tag{1.6}$$

where $\vec{N}_d$ is the *demagnetizing tensor* mainly depending on the shape of the body.

In the case of ellipsoids, by considering a suitable reference system with axes parallel to the semiaxes of the ellipsoid, this tensor becomes diagonal and the diagonal terms are called *demagnetizing factors*. The values of these factors along different semiaxes are related by the constraint $\sum N_i = 4\pi$ (C.G.S. units). In the case of a thin film that can be well approximate by an infinite flat plate, $N = 4\pi$ if the sample is magnetized normal to its surface and $N = 0$ if it is in-plane magnetized. In this way the magnetization tends preferentially to lie in the film plane.

In analogy with the magnetocrystalline anisotropy energy and by considering the cosine direction of the magnetization relative to the axes of the ellipsoid, the *shape anisotropy energy* can be expressed as:

$$E = K_f \sin^2\theta + ... \tag{1.7}$$

where $K_f = \frac{1}{2} M^2 N$ is the *shape anisotropy constant*.

1.2.3 Stress Anisotropy and the Magnetoelastic Energy

Stress is a magnetomechanical strain induced by the presence of dislocations and defects, different thermal expansion coefficients, by lamination procedures, and by the lattice mismatch among different materials. The stress induces a variation of the lattice symmetry with the consequent appearance of an uniaxial anisotropy along the stress axis.

This effect can be taken into account by considering the *magnetoelastic energy* that for an isotropic material can be defined as:

$$E_{me} = \frac{3}{2} \lambda_s \sigma \sin^2\theta + \text{const.}, \tag{1.8}$$

where σ is the strain, θ is the angle between the stress and the magnetization directions and λ_s is the isotropic saturation magnetostriction constant. By introducing the constant $K_\sigma = (3/2)\lambda_s \sigma$ the above equation assumes the same form of the magnetocrystalline anisotropy energy. The behaviour of a sample subjected to a stress is indeed determined by the sign of the $(\lambda_s \sigma)$ product. The axis of stress is an easy axis if $(\lambda_s \sigma) > 0$, on the contrary if this quantity is negative the stress axis is a hard axis and the energy minimum is reached only for $\theta = 90°$, i.e. in this case an easy magnetization plane exists.

As for the *magnetostriction*, it represents the lattice deformation along the magnetization direction when a crystal is subjected to a magnetic field. This lattice deformation induces a change of the magnetization direction in this way influencing the anisotropy axis.

It is to be noted that the magnetostriction arises only if the anisotropy energy of the system decreases of a quantity greater than the amount that increases the elastic energy of the system.

There are two kinds of magnetostriction: a *spontaneous magnetostriction* that occurs in each domain when a specimen is cooled below the Curie point and a *forced magnetostriction* which occurs when a saturated specimen is exposed to fields large enough to increase the magnetization of the domain above its spontaneous value. Both kinds are due to an increase in the degree of the spin order. For temperature higher than the Curie temperature, the magnetostriction is equal to zero because of the absence of interactions between magnetic moments. Since the spontaneous strain is independent on the magnetization sense, the dimensions of a domain do not change when the direction of its spontaneous magnetization is reversed. In this way the process of the domain wall motion does not produce any magnetostrictive change in dimensions. On the contrary the rotation of moments of a domain always produces a dimensional change, since the spontaneous magnetostriction depends on the direction of the M_s vector with respect to the crystal axes.

1.2.4 Induced Anisotropy

The application of magnetic fields, stresses, annealing processes and plastic deformations during the growth can induce the appearance of an easy magnetization axis, by favouring the establishment of a local directional order due to a more easily diffusion or the formation of preferential interstitial sites. The phenomenological representation of this type of anisotropy is the same as that for the magnetocrystalline or shape anisotropy, considering that the anisotropy constant depends, in this case, from the chemical composition of the material.

1.3 Magnetic Domains

Domains[2,3] are regions of uniform magnetization, in which the spins are all aligned along a preferred direction through the exchange interaction. The crystals, in the demagnetized state, are generally in a multi-domain configuration that arises in order to reduce the stray field [Fig. 1.2(a)].

The subdivision into smaller domains is limited by the presence, between different domains, of a transition layer, the *domain wall*, that adds energy to the system. In this region, the direction of the atomic spins gradually changes from the one domain orientation to the adjacent one. Inside the wall the spins are not parallel to their neighbours and not parallel to the

easy axis. Therefore, their characteristics (width and energy) are determined by the balance of the exchange and anisotropy energies. In effect, while the exchange energy tries to make the wall as wide as possible, in order to make the angle ϕ between adjacent spins as small as possible, the anisotropy energy tries to make the wall thin in order to reduce the number of spins pointing in non-easy directions. This kind of domain wall is called *180° Bloch wall* [Fig. 1.2(b)] and its width describes the spatial response of the magnetization to local perturbation.

For very small ϕ, the exchange energy associated to the formation of a wall, varies as ϕ^2. In effect, considering a pair of atoms with the same spin *S* this energy can be expressed as:

$$E_{ex} = JS^2\phi^2 - 2JS^2 \tag{1.9}$$

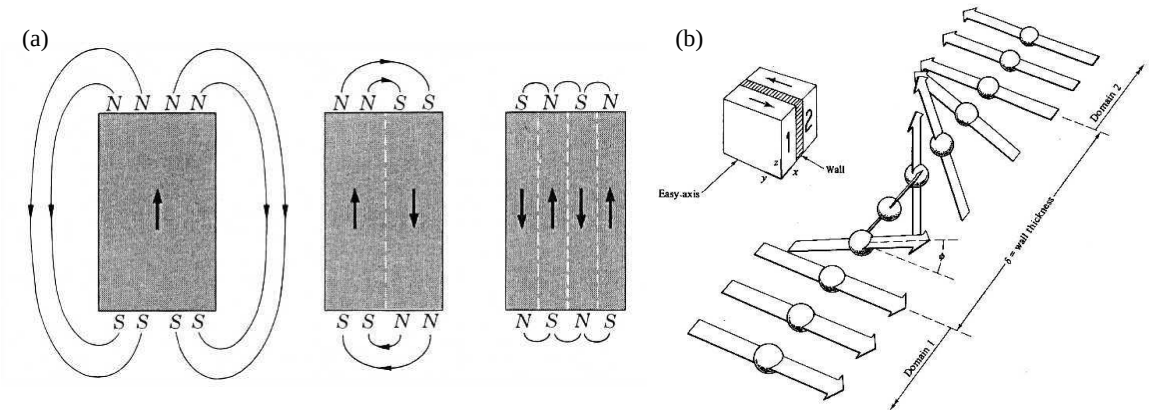

Figure 1.2 – (a) Schematic representation of the domain formation in an uniaxial material. The spatial extension of the stray field and hence the magnetostatic energy strongly decrease as the domains form. (b) Schematic representation of a 180° Bloch domain wall for a cubic crystal. ϕ is the angle between adjacent spins[1].

The first term in equation 1.9 is characteristic of a domain wall and is called *extra exchange energy*. For a wall *N* atom thick ($\phi = \pi / N$), and a system with cubic symmetry and lattice constant *a*, the exchange energy per unit area can be expressed as:

$$\gamma_{ex} = JS^2\phi^2 \frac{N}{a^2}. \tag{1.10}$$

The anisotropy energy per unit area of a wall can be defined as:

$$\gamma_{an} = KNa \tag{1.11}$$

where *K* is the anisotropy constant.

The total wall energy per unit area for a wall of thickness $\delta_w = Na$ is $\gamma_w = \gamma_{ex} + \gamma_{an}$. By imposing $\frac{\mathrm{d}\gamma_w}{\mathrm{d}\delta_w} = 0$, the energy minimum can be found, corresponding to a domain wall width of $\delta_w = \pi\sqrt{A/K} \approx \sqrt{T_c / K}$. It occurs when the values of the exchange energy and the anisotropy energy are equal [Fig. 1.3(a)]: $\gamma_w = 2K\delta = 2\pi\sqrt{AK}$.

The balance between the magnetostatic energy of the system in the single-domain state and the domain wall energy in the multi-domain state allows to evaluate an equilibrium domain size:

$$D_s = \sqrt{\frac{\gamma_w L}{1.7 M_s^2}} \tag{1.12}$$

where L is the thickness of the crystal.

The ratio of the total energy before and after the division into domains is:

$$\frac{E(\text{single-domain})}{E(\text{multi-domain})} \approx \sqrt{\frac{M_s^2 L}{\gamma_w}} \,. \tag{1.13}$$

For very thin thickness of the crystal, the reduction of the energy becomes smaller and the wall energy tends to increase because of the lower width [Fig. 1.3(a)]. In this situation the crystal prefers to remain in the single-domain state. This effect is due to the dependence of the energy gain from the crystal thickness L. In Fig. 1.3(b) the behaviour of the total energy is reported with respect to the crystal size for the single- and multi-domain state.

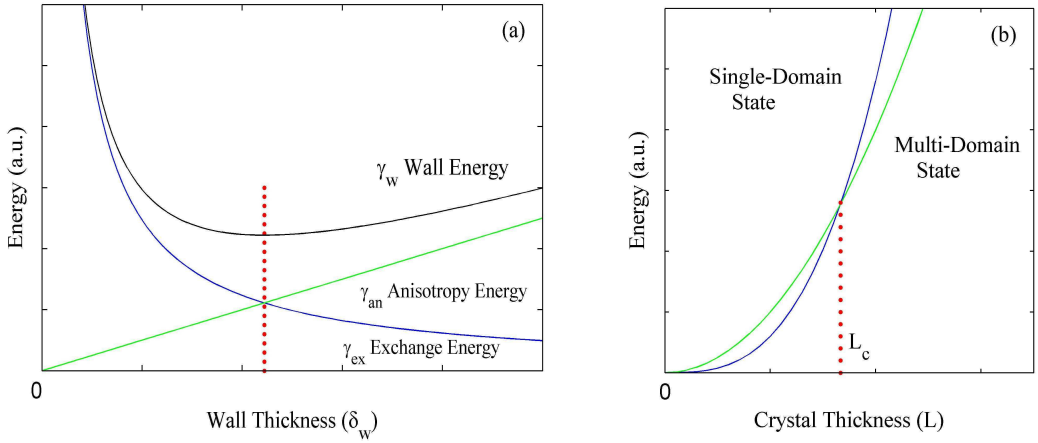

Figure 1.3 – (a) Total wall energy with respect to the domain wall thickness. (b) Relation between the energy of a crystal and its linear dimensions L for the single- and multi-domain states. L_c is the critical size of the crystal, below which the single-domain state is favoured.

The two curves indicate the existence of a critical thickness below which the single-domain state is favoured. Its value depends linearly from the domain wall energy density and is inversely proportional to the square of the saturation magnetization: $L_c = 1.7\gamma_w / \left(\pi^2 M_s^2\right)$.

The single-domain crystals are permanent magnets and the inversion of magnetization can take place only through coherent rotation processes.

1.4 Superparamagnetism

The initial stage of a film growth is characterized by a granular state with ultrathin particles having *superparamagnetic properties*. The anisotropy energy of a particle is: $E = KV$ where V is the volume of the particle and K is the anisotropy constant. By reducing the particle dimensions below a critical size D_P, the thermal energy, proportional to k_BT, becomes comparable to the anisotropy energy. In this case, thermal fluctuations can overcome the anisotropy energy barrier, reversing the magnetization also in the absence of an applied magnetic field.

The name "superparamagnetic particles" derives from the fact that these systems behave like paramagnetic materials. The only difference is the value of the magnetic moment that in a paramagnet is of a few Bohr magnetons μ_B, while in a superparamagnet is of the order of ten thousands of μ_B.

It is to be noted that the superparamagnetism is a time-dependent phenomenon and thus the critical size for superparamagnetic behaviour depends on the characteristic time of the experiment. In effect small ferromagnetic particles present several magnetization equilibrium states separated by energy barriers. Their magnetic properties are the result of the evolution of the magnetization in a metastable state, in which the system remains trapped over a time period much longer than the *observation time* t_{obs}. However at a given temperature, thermal activation over the energy barrier leads the system toward the thermodynamic equilibrium. This process is known as *thermal relaxation* and has a characteristic time called *relaxation time* t_{rel} defined as:

$$t_{rel} = t_0 \exp\left(\frac{KV}{k_B T}\right) \tag{1.14}$$

where t_0 is a constant of the order of $10^{-12} \div 10^{-9}$ s.

Indeed ferromagnetic properties are found when $t_{obs} << t_{rel}$, whereas for $t_{obs} > t_{rel}$ the systems show superparamagnetic behaviour. In the intermediate situation $t_{obs} \sim t_{rel}$ nonequilibrium phenomena and magnetic relaxation occur.

Therefore, particles that show superparamagnetic properties in standard magnetic measurements (t_{obs} of the order of some seconds) can behave as ferromagnets in Mössbauer experiments where t_{obs} is $\sim 10^{-9}$ s.

Magnetically, a superparamagnetic system is characterized by magnetization curves without coercivity or remanence, that coincide if plotted as a function of (H/T) ratio, where T is the measurement temperature. The hysteresis in the loop appears both by increasing the particle diameter above the critical size D_P, or by reducing the measurement temperature below

a value T_B, called *blocking temperature*. The thermal energy associated to this temperature is lower than the anisotropy energy and the magnetization becomes stable.

In a Mössbauer spectrum, time-dependent effects are often observed via the magnetic field. There are two important timescales involved here: the lifetime of the nuclear excited state and the Larmor precession time. If the nucleus shows a well resolved magnetic splitting, at least one complete Larmor precession occurs before the nuclear state decades. On the contrary if the spectrum shows a relaxation broadening, the electronic configuration changes at a rate faster than that corresponding to the nuclear Larmor precession rate. Hence the nucleus senses a time-averaged hyperfine environment, which manifests with a collapse of the magnetic field. The reduced hyperfine field B_{hf} can be described by the equation:

$$B_{hf} = B_{hf,0}\left(1-\frac{k_B T}{2KV}\right) \tag{1.15}$$

where $B_{hf,0}$ represent the bulk value of the hyperfine magnetic field.

1.5 Coercivity and Particle Sizes

Contrary to the saturation magnetization that is an intrinsic property of the specimen, the coercivity is a size dependent characteristic (Fig. 1.4). By decreasing the grain sizes the coercivity increases and has a maximum for a critical particle size D_s. Below this value coercivity decreases until to approach the zero value for diameter lower than D_p. This behaviour is due to the different mechanisms that are responsible for the magnetization reversal.

For diameter greater than D_s, the particles are multi-domains and the reversal of magnetization mainly occurs through domain wall motion.

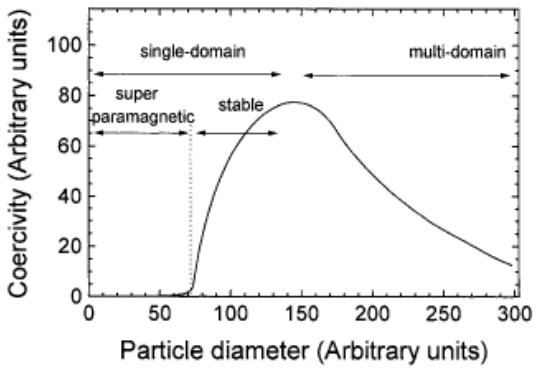

Figure 1.4 – Coercivity H_c behaviour as a function of the particle sizes D, for a fixed temperature[1].

In this regime, the size dependence of the coercivity is experimentally found to be given by:

$$H_c = a + \frac{b}{D} \tag{1.16}$$

where *a* and *b* are constants.

For particle sizes in the range between D_s and D_p, the particles tend to become single-domain and the main mechanism controlling the reversal is the moment rotation.

For sizes lower than D_s, thermal effects become significant and the coercivity gradually decreases following the relation:

$$H_c = g - \frac{h}{D^{3/2}} \tag{1.17}$$

where *g* and *h* are constants. Below the critical diameter D_p, the coercivity is zero since the thermal effects are strong enough to demagnetize the ensemble and the particles become superparamagnetic.

1.6 Magnetization Processes

Two are the main mechanisms that govern the magnetization processes: the *domain wall motion* and the *moment rotation*. In the demagnetized state, all the domains are spontaneously magnetized to their saturation value with the magnetization pointing along their easy axes. The application of an external field along an easy direction gives rise to an expansion of the domains with the magnetization pointing along the field direction with the consequent increase of the total magnetization. The domain walls move until the internal field of the material is zero, i.e. when the applied field is equal to the demagnetizing field. If the field is applied along an easy direction axis, the saturation is reached only through the domain wall motion, in all other cases the magnetization is subjected to a torque moment and the saturation is asymptotically reached through the moment rotation (Fig. 1.5).

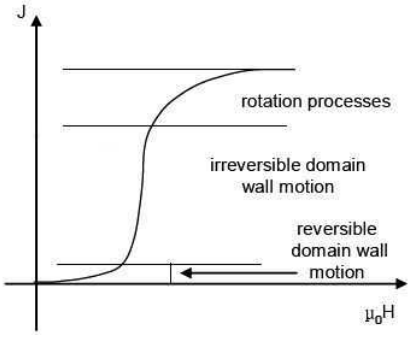

Figure 1.5 – Magnetization processes in a multi-domain particle.

1.6.1 Magnetization Rotation

The application of a magnetic field along a hard direction induces the moment rotation. The theoretical model of Stoner and Wohlfarth[4] for uniaxial single-domain particles having a shape of an ellipsoid of revolution considers only processes of coherent rotation, i.e. during the reversing the spins of all the atoms remain parallel each other. In this approximation among the spins a strong exchange coupling is present giving rise to a uniform magnetization.

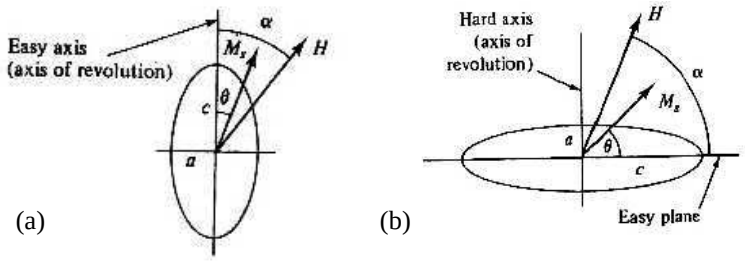

Figure 1.6 – Schematic representation of (a) a prolate and (b) an oblate spheroid, and of the directions of the magnetization and the applied magnetic field with respect to the easy direction.

For crystals with the symmetry of prolate spheroids, the shape anisotropy induces an easy magnetization axis along the major axis of the spheroid. By minimizing the total energy of the system, it is possible to obtain the equilibrium position θ of the magnetization as a function of the magnetic field H, applied to an arbitrary angle α from the easy axis [Fig. 1.6(a)].
The total energy density of the system is given by the anisotropy and the Zeeman energy:

$$E_T = K_u \sin^2\theta - HM_s \cos(a-\theta) \tag{1.18}$$

where $M_s \cos(\alpha-\theta)$ represents the component of the magnetization along the direction of the applied field and $K_u = \frac{1}{2}(N_a - N_c)M_s^2$ is the shape anisotropy constant.

The equilibrium position of the saturation magnetization coincides with the minima of the energy that are given by:

$$\frac{\mathrm{d}E}{\mathrm{d}\theta} = \sin\theta\cos\theta - h\sin(\alpha-\theta) = 0 \tag{1.19}$$

where $h = H / H_k$ is the reduced field and $H_k = (2K_u)/M_s$ is the anisotropy field. The above condition states that the torque applied by the field on the magnetization $\vec{H}\times\vec{M}$ must be zero.
If $\alpha = 90°$, the magnetization is a linear function of the applied field $m = h$, where $m = M / M_s$ is the reduced magnetization defined as: $m = HM_s/(2K_u)$. This relation implies that the field, required for the complete saturation of the system, is equal to the anisotropy one:

$$H = \frac{2K_u}{M_s} = H_k \,. \tag{1.20}$$

If $\alpha = 0°$, the field is along the easy axis and parallel to M_s. By reducing the field to zero and then increasing it in the opposite direction $\alpha = 180°$, the magnetization remains stable until the applied field reaches the value of H_k, at which the moment rotates along the direction of the applied field.

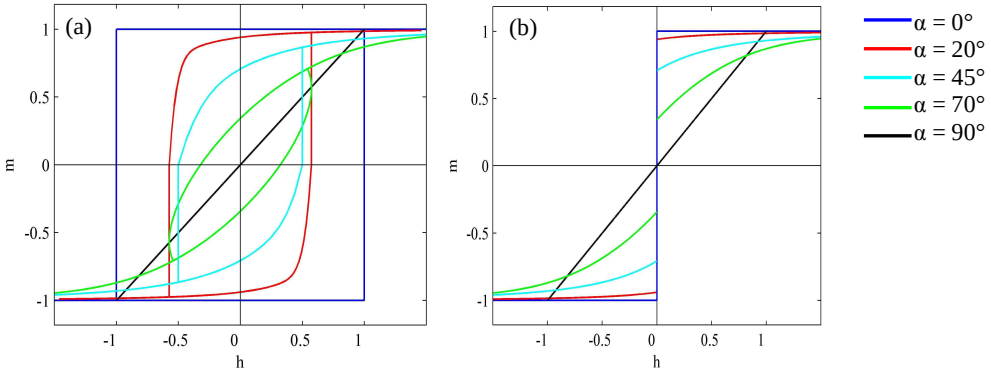

Figure 1.7 – Magnetization curves of an uniaxial single-domain assembly of particles with (a) prolate and (b) oblate spheroid shapes. α is the angle between the field vector and the easy magnetization axis.

The anisotropy field in effect represents the intensity of the field that must be applied for the complete rotation of the magnetization along the direction of the field itself. The hysteresis loop is rectangular.

In the case of an arbitrary α angle, the critical field h_c corresponding to the critical angle θ_c at which the complete reversal of the moments occurs, is a stable equilibrium point of the energy for which the following constraints are realized $\frac{\mathrm{d}E}{\mathrm{d}\theta} = \frac{\mathrm{d}^2 E}{\mathrm{d}\theta^2} = 0$:

$$\tan^3 \theta_c = -\tan\alpha \tag{1.21}$$

$$h_c = -\frac{\left(1 - \tan^2\theta + \tan^4\theta\right)^{1/2}}{1 + \tan^2\theta} \,. \tag{1.22}$$

In this case the hysteresis loop consists of reversible and irreversible portions, the latter constituting *Barkhausen jumps*.

The magnetization rotates irreversible for $\alpha = 0°$ while it continuously rotates without abrupt change for $\alpha = 90°$. The critical field value, i.e. the value at which the M_s vector flips from one orientation to another, decreases from 1 at $\alpha = 0°$, to a minimum of 0.5 for $\alpha = 45°$ [Fig. 1.7(a)] and then increases to 1 again as α approaches 90°. These critical values are equal for any two values of α symmetrically located around $\alpha = 45°$. On the contrary the coercive field that is the field that reduces the magnetization component along the field direction to zero,

is the highest when the field is applied along the easy magnetization axis, while it is the lowest for an applied field parallel to the hard axis ($\alpha = 90°$).

In the case of oblate spheroid shape [Fig. 1.6(b)], the minor revolution axis is a hard magnetization axis end an easy plane of magnetization exists. By minimizing the total energy with respect to the θ angle, for $\alpha = 90°$ the situation is the same as in the case of the prolate spheroid [Fig. 1.7(b)]. On the contrary, for $\alpha = 0°$ the magnetization loop does not show the hysteresis phenomenon, because of the existence of an easy plane of magnetization that allows the complete rotation of the magnetization also for applied field approaching the zero value.

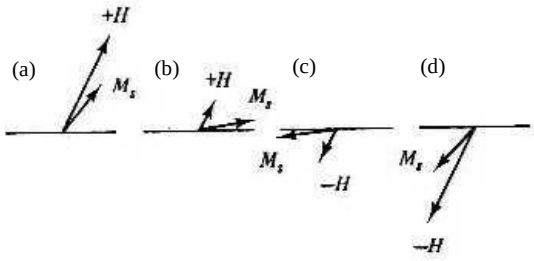

Figure 1.8 – Schematic representation[1] of the magnetization rotation in a crystal with oblate spheroid shape. By reducing the field from large positive value (a) to a small positive value (b), M_s rotates reversibly towards the easy plane, as H changes to a small negative value (c), M_s rotates by 180° in the easy plane. By increasing the field in the negative direction, the magnetization rotates away from the easy plane (d).

For intermediate value of α, by reducing the field from large positive value Fig. 1.8(a) to a small positive value Fig. 1.8(b), M_s rotates reversibly towards the easy plane, then when the external field becomes negative the magnetization rotates of about 180° into the easy plane and the reduced magnetization abruptly changes from a positive to a negative value at h = 0 [Fig.1.7(b)]. Finally, by increasing the applied field in the negative direction the magnetization rotates away from the easy plane [Figs. 1.8(c) and (d)].

1.6.2 Magnetization Curves of Polycrystalline Samples

The magnetization curves of an assembly of uniaxial non-interacting particles with their easy axis randomly oriented in space, have shapes that are intermediate between the squared and the linear ones obtained for field applied respectively parallel and perpendicular to the easy axis in monocrystalline uniaxial single-domain particles. In Fig. 1.9 a few magnetization states for this type of systems are reported.

The demagnetized state in the figure is represented by point O, in this state the domains can be represented by a set of vectors randomly oriented. By increasing the external field, the magnetization starts to rotate with the disappearance of a few domains having M_s oriented along directions different from that of the applied field, point B. In point C, the system reaches the

saturated state and the moments are all parallel to the field vector. The following decrease of the external field induces the appearance of new domains having the direction of their easy magnetization axis near to that of the magnetic field, point D.

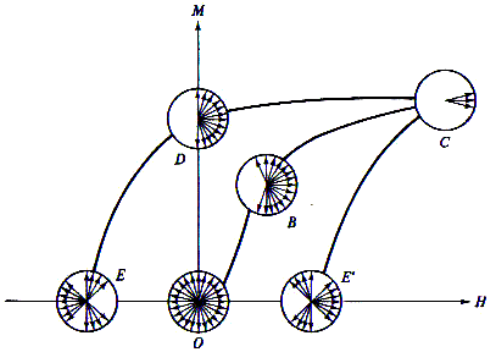

Figure 1.9 – Domain representation for different magnetization states of a polycrystalline sample, constituted by uniaxial grains each oriented randomly.

The remanence (i.e. the value of the magnetization reached for zero applied field) to saturation ratio M_r / M_s calculated by Stoner and Wohlfarth, for this type of system, is equal to 0.5 while the reduced coercivity is about 0.48. It is to be noted that the model gives only an estimated value of the squareness of the hysteresis loop, since the effects due to demagnetizing field arising from the surface free charges are not considered.

1.6.3 Incoherent Magnetization Reversal

In the above theoretical model of Stoner and Wohlfarth the starting assumption is the coherent rotation of the spins. This implies that among the particles no magnetic interactions are present. In real materials, it is very difficult to realize this situation and the particles tend to interact giving rise to an incoherent reversal i.e. the spins during the rotation do not remain parallel. The most important modes are the magnetization *fanning* and *curling*.

Fanning implies that the magnetization vectors of successive particles fan out in a plane by rotating in alternate directions in alternate particles. In this case the coercivity is three times lower than the value found assuming a coherent rotation.

Curling mode is characterized by the fact that the spins are not parallel during the rotation but form closed circles of flux. In this case no free poles are formed on the specimen surface and no magnetostatic energy is involved. Contrary to the coherent rotation and fanning processes, this mode is strongly size dependent and the coercivity tends to decrease as the particle sizes increase.

Figure 1.10 shows, for an infinite cylinder, the particle size dependence of the coercivity for different modes of reversal. For small particles, the coherent rotation is favoured, on the contrary large particles prefer to reverse by curling mode.

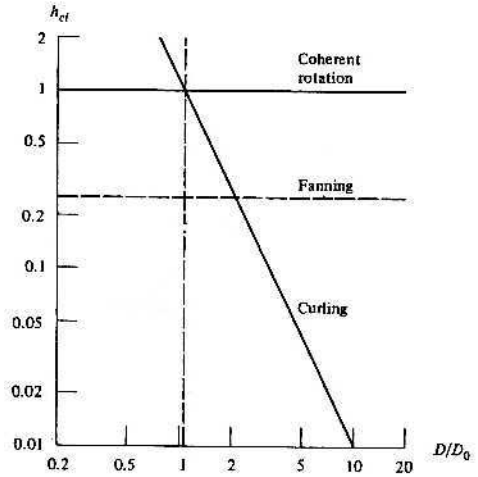

Figure 1.10 – Reduced coercivity calculated for different reversal mode as a function of the reduced diameter of the particles D / D_0 where $D_0 = 2A^{1/2} / M_s$ [1].

It is to be noted that neither the Stoner-Wohlfarth rotation nor the curling mode account for the coercivity of real materials. In effect in real specimens the coercive value is much lower (20-40 %) than the anisotropy field, this effect is known as *Brown's paradox*.
The reason lies in the real structure of the specimens. Defects and imperfections can act both as pinning sites for domain wall motion or as nucleation points where a reversed domain can be easily created (Fig. 1.11)[5]. The different behaviour of the defects gives rise also to a different behaviour of the first magnetization curves, remanence curves and minor loops (Fig. 1.12).

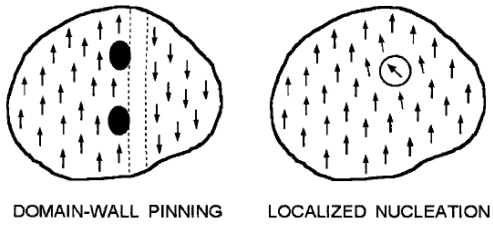

Figure 1.11 – Pinning mechanism: the coercivity is controlled by the trapping of the domain wall at pronounced inhomogenities. Nucleation mechanism: the defects favour the formation of reversed domains and the coercivity is determined by the reversal field at which the original magnetization becomes unstable.

In the case of *domain wall pinning*, the initial magnetization curves are characterized by a low susceptibility up to values of the applied field of the order of the coercivity at which the curves abruptly increase up to the saturation. The minor loops show that by decreasing the maximum applied field, the coercive field remains practically unchanged, while the saturation magnetization gradually decreases. In effect, in this case, defects and inclusions can be treated

as demagnetized regions since their spontaneous magnetization differs from that of the surrounding material. The wall spontaneously tends to adhere to these inclusions, favouring a reduction of the domain wall area and energy. The efficiency of the pinning has a maximum for inclusion sizes comparable to those of the wall.

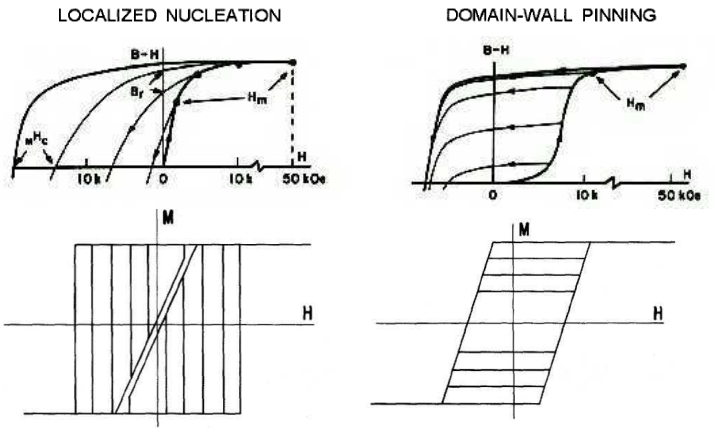

Figure 1.12 – Schematic representation of the first magnetization curves, IRM (isothermal remanence curves) and minor loops for a specimen with the coercivity controlled by nucleation and domain wall pinning mechanism.

Around these inclusions generally spike or closure domains form having the function to decrease the surface concentration of free charges that are sources of magnetostatic energy. The closure domains took their name because they are path by which the magnetic flux can close on itself, reducing to zero the magnetostatic energy. Their formation is not always favoured since it implies an increase of the anisotropy energy. In response to an applied field, the domain wall tends to move away from the inclusion. During the motion, the domains around this inclusion are deformed and new closure domains form. Further motion of the wall lengthens these domains. Until this point the change in magnetization is reversible and the initial domain configuration can be regained if the field is reduced. But if the field is continually increased, the domains do not continue to increase since the increased area adds too much wall energy to the system. At this point the magnetization process becomes irreversible: the wall instantaneously breaks its interaction with the domains and jumps a distance living the inclusion and its domains (*Barkhausen jumps*).

The coercivity due to pinning-type mechanism that involves obstacles with dimensions small compared to the magnetic domain wall width can be expressed as[6]:

$$H_c = \alpha\left(2K_1 / M_s\right) - N_{eff} M_s \tag{1.23}$$

where α is a parameter related to the pinning strength of the small obstacles and $N_{eff} M_s$ is the demagnetizing field.

In the case of *nucleation controlled coercivity* a nucleus is formed in which the magnetization is not fully aligned, the initial susceptibility is very high and the magnet easily

reaches the complete saturation (Fig. 1.12). As for the minor loops, by decreasing the maximum applied field the saturation magnetization remains constant and only the coercivity gradually decreases. In this case the imperfections can be treated as a modification of the local anisotropy that leads to a reduction of the nucleation field and coercivity.

The coercivity in this case is inversely proportional to the grain size and can be expressed as follows:

$$H_c = \beta(\gamma M_s)(1/D) \tag{1.24}$$

where β is a geometrical factor related to the details of the nucleus geometry for the reversed magnetization domain, γ is the magnetic domain wall energy and D is the grain diameter[6].

The occurrence of nucleation or pinning-depinning mechanism may be also characterized by the fact that the angular dependence of the coercive field is very different from the one corresponding to the coherent rotation (Fig. 1.13):

$$H_c(\theta) = \frac{H_k}{\left(\sin^{2/3}\theta + \cos^{2/3}\theta\right)} \text{ for coherent rotation} \tag{1.25}$$

$$H_c(\theta) \approx \frac{H_c(0)}{\cos\theta} \text{ for nucleation/pinning mechanism} \tag{1.26}$$

where θ is the angle between the direction of the applied field and the easy axis and $H_c(0)$ is the coercive field for $\theta = 0°$.

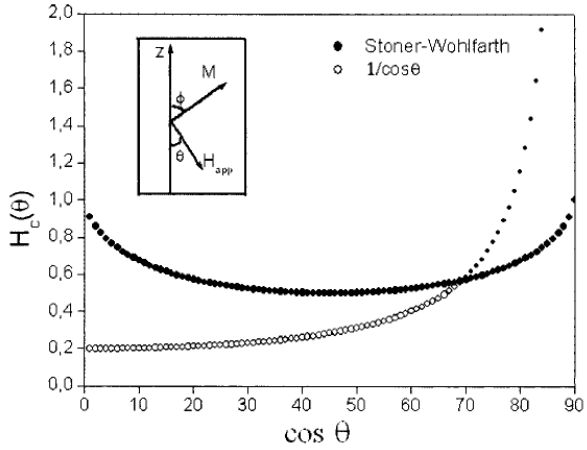

Figure 1.13 – Angular variation of the normalized coercive field $H_c(\theta) / H_k$ as evaluated in the Stoner-Wohlfarth model and the 1/cosθ dependence.

Equation 1.26 reflects the fact that only the projection of the applied field along the moment direction is active in the reversal process. The coherent rotation becomes the predominant mechanism only for very large θ values.

1.7 Thin Films and Multilayers

In the case of very low thickness, generally lower than 1 μm, thin films and multilayers can be treated as bi-dimensional systems. Among them, of particular interest are the structures constituted by different ferromagnetic phases or intercalated ferro-/antiferromagnetic layers and the superlattice structures formed by magnetic/non-magnetic layers.

In these systems, the macroscopic properties are strongly influenced by the periodical modulation along the growth direction, by surface/interface phenomena and by the type and strength of the interaction that develops between different layers. Their characteristics and properties are used in the microelectromechanical and optical fields, in the production of magnetic sensors and protective coatings against corrosion.

1.7.1 Magnetic Properties

The magnetic properties of thin films and multilayers[7-8] are strongly influenced by the presence of interfaces and surfaces, since the surface/volume ratio strongly increases. Surfaces and interfaces are regions of low symmetry where the periodicity of the crystallographic lattice is strongly modified. The corresponding energies are the main causes of the appearance of a perpendicular anisotropy that induces a spontaneous tilting of the easy axis out of the film plane. The origin of the interface anisotropy lies in the change of the magnetocrystalline anisotropy, indeed, effects such as roughness, defects, interface intermixing and the crystallographic orientation strongly influence the degree of tilting of the easy axis.

In low dimensional systems, the anisotropy energy can be expressed trough an effective anisotropy constant that can be written as a weighted average over the whole thickness t of two contributions, one due to volume/bulk effects (K_v) and the second due to interfaces and surfaces (K_s / t):

$$K_{eff} = K_v + 2\frac{K_s}{t} \tag{1.27}$$

The 2 factor derived from the hypothesis of two identical interfaces.

Contrary to the surface/interface effects, the shape anisotropy is opposing to the perpendicular tilting of the easy axis favouring an in-plane orientation. However under specific conditions, e.g. the presence of suitable magnetic spacer and below a critical thickness value, films and multilayers can display a predominant perpendicular anisotropy. This can be also achieved by exploiting the volume contribution in order to overcome the magnetostatic term.

The effect of the shape anisotropy can be considered by adding the magnetostatic term to equation 1.27:

$$K_{eff} = K_v + 2\frac{K_s}{t} - 2\pi M_s^2 \tag{1.28}$$

The sign of K_{eff} determines the direction of the easy axis, in particular for $K_{eff} > 0$, the easy axis points along the normal to the film plane. For $K_{eff} = 0$, a critical thickness can be defined:

$$t_c = -2\frac{K_s}{K_v - 2\pi M_s^2} \tag{1.29}$$

below which the interface and surface contributions overcome the volume and magnetostatic ones and the system shows a perpendicular component to the anisotropy (Fig. 1.14).

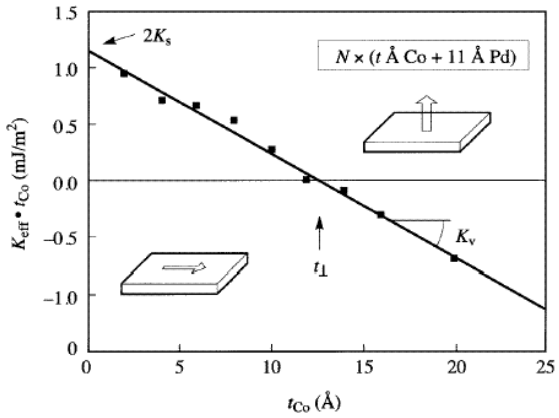

Figure 1.14 - $K_{eff} \cdot t_{Co}$ as a function of t_{Co} for a Co/Pd multilayer

1.7.2 Domain Walls in Thin Films

In a Bloch domain wall, the moments rotate around an axis normal to the domain wall surface (Fig. 1.15). When the wall width is greater or comparable to the film thickness, the magnetostatic energy overcomes the exchange and the anisotropy energies and the wall energy density strongly increases [Fig. 1.16(a)]. In this case, a new type of domain wall forms, called *Néel wall*[6], in which the rotation occurs around an axis that lies in the wall plane and is normal to the film plane (Fig. 1.15).

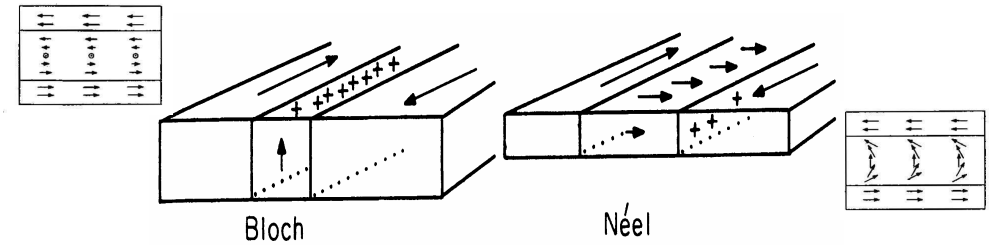

Figure 1.15 – Schematic representation of the moment rotation in a Bloch and Néel domain wall.

This particular type of rotation induces the formation of free magnetic charges only on the wall surface (Fig. 1.15), favouring the spins to remain parallel to the film plane during the reversal. This gives rise to a strong decrease of the magnetostatic energy.

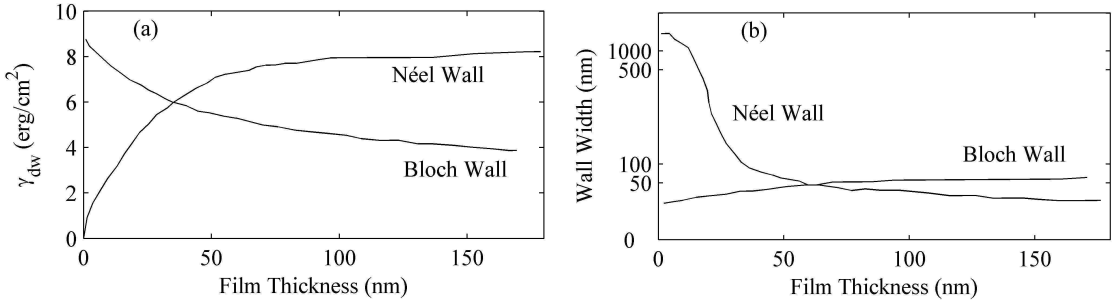

Figure 1.16 – (a) Domain wall energy per unit area and (b) width of a Bloch and Néel wall as function of the film thickness[1].

The magnetostatic energy gain between a Bloch and Néel wall, depends on the ratio between the wall width δ and the film thickness t:

$$\frac{\gamma_B}{\gamma_N} = \frac{\delta}{t} \tag{1.30}$$

This equation shows that the Néel walls are favoured for film thickness lower than the domain wall width [Fig. 1.16(b)].

1.7.3 Stripe Domains

A peculiar domain configuration characterizes thin films with perpendicular anisotropy. In the case of *weak perpendicular anisotropy* the magnetization lies in the film plane since the demagnetization effects dominate. By increasing the film thickness the magnetostatic term becomes less important if compared to the anisotropy and beyond a critical thickness the magnetization starts to oscillate periodically out of the film plane. The domain pattern is constituted by *stripe domains* pointing up and down respect to the film surface [Fig. 1.17(a) and 1.17(b)]. The sizes of these domains are comparable to the film thickness.

It is to be noted that while the shapes of the hysteresis loops and the domain sizes are strongly dependent from the film thickness, the wall energy is only dependent from the deflection angle of the magnetization respect to the film plane.

In the case of *strong perpendicular anisotropy* this domain pattern is stable also in the demagnetized state and for very low thickness. In this case the hysteresis loops are modified, and they assume a particular shape called "*transcritical shape*" characterized by very low remanences.

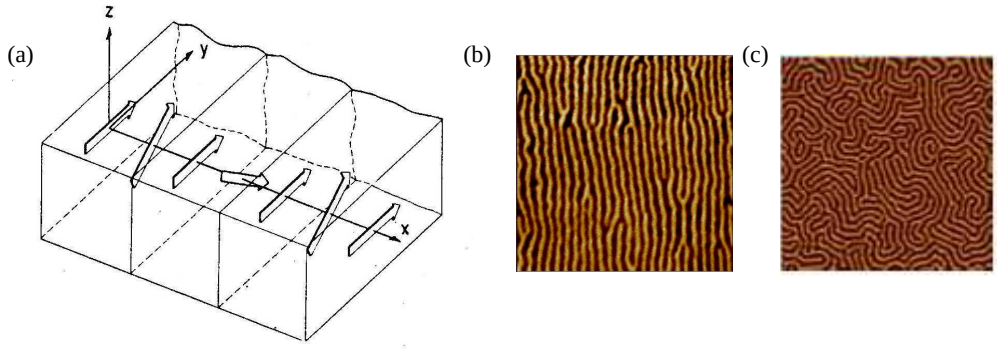

Figure 1.17 – (a) Schematic representation of the magnetization vectors in a stripe domain[1]. MFM images of (b) stripe domains and (c) labyrinth-type stripe domains in low coercive films.

The morphology of the domain depends also on the field history. Demagnetizing the films with a perpendicular applied field results in labyrinth-stripe domains with random in-plane orientation [Fig. 1.17(c)]. However, demagnetizing the film with an in-plane magnetic field, it couples to the in-plane magnetization component of the domain wall and aligns the stripe domains parallel to the external field direction [Fig. 1.17(b)]. Furthermore, in high coercive films the stripe configuration becomes less regular and periodic respect to those of Figs. 1.17(b) and 1.17(c), assuming a more maze-like pattern.

1.7.4 Magnetization Processes in Thin Films

A thin film can be represented by an oblate spheroid, with the demagnetizing factor along the revolution axis (normal to the film plane) equal to 4π and that in the film plane practically equal to zero. This is due to the fact that the in-plane demagnetizing factor is proportional to the film thickness D and inversely proportional to the film surface size L: $N_{\parallel} = 4\pi D / (D + L) \to 0$.

In these systems, the easy axis can be perpendicular to the film plane only when the anisotropy field overcomes the demagnetizing field. Indeed by measuring the hysteresis loop with the field applied perpendicular to the film plane, the saturation should be reached for field of the order of $4\pi M_s$. Experimentally it was found that the saturation can occur for lower fields, whose values depend on the film thickness, the saturation magnetization and the specific wall energy.

Kooy and Enz[9] develop a theoretical model that derives the shape of the hysteresis loop for film showing a strong perpendicular anisotropy. This requirement implies that the anisotropy field must be much greater than the demagnetizing field, favouring in this way the absence of closure domains. Moreover, the studied system is constituted by stripe domains, in a magnetic state near to the saturation in which a unique reversed domain of width *d* is present.

By increasing the applied field, the domains with magnetization oriented parallel to the field direction increase their sizes while those opposing to the field decrease. In effect, the domain with magnetization parallel to the applied field grows of an amount greater than the amount that the reversed domain decreases. Therefore, in this system, a stable state can be found for fields lower than $4\pi M_s$ and for finite values of the reversed domain width *d*.

By decreasing the film thickness *D*, the value of the saturating field decreases [Fig. 1.18(a)] from the $4\pi M_s$ value, value that can be reached only if the width *d* of the reversed domain is comparable or greater than the film thickness.

The existence of a stable state for a finite value of *d* suggests that an energy barrier is present that does not allow the disappearance of the reversed domain in the saturated state. In effect, the reversed domains change their shapes giving rise to a *bubble domains pattern*.

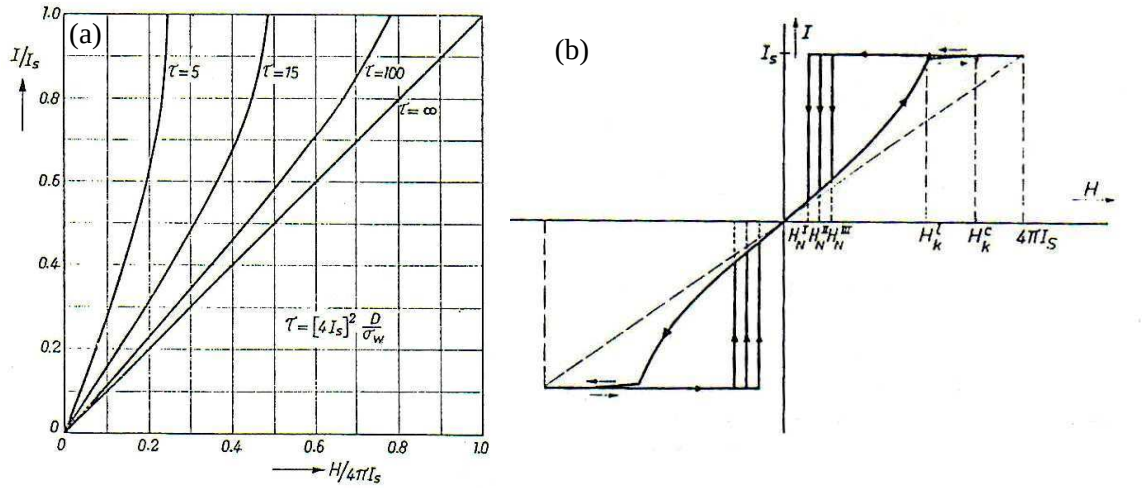

Figure 1.18 – (a) Theoretical magnetization curves of an infinite plate with easy axis normal to the film plane evaluated for different values of the reduced film thickness τ, whose expression is reported inside the figure[9]. (b) Theoretical demagnetization curve of an infinite plate with perpendicular anisotropy[9].

Therefore, two critical fields can be defined, the first H_k^L at which the reversed stripe domains change their shape into a bubble one and the second H_k^C at which the reversed bubble domains become unstable and then disappear [Fig. 1.18(b)]. For fields greater than H_k^C the magnetization process becomes irreversible and the specimen remains in the saturated state until the field intensity decreases to a value H_N^i at which a nucleation centre is activated. At this point a domain wall is enucleated or unpinned, and the reversal of the magnetization starts.

Becker suggested that each particle has a determined number of pinning sites for the wall motion each of which characterized by the own nucleation field H_N^i. The activated nucleation point depends on the maximum value of the applied field that determines the intensity of

adhesion of the wall to the inclusions or defects. The presence of these pinning sites lowers the field necessary for the complete reversal of the magnetization.

1.8 Exchange-Spring Magnets

The *exchange-spring magnets* are characterized by both high coercive field and saturation magnetization values thanks to the exchange-coupling that develops between two different and finely dispersed ferromagnetic phases. One of these phases is soft with high value of the saturation magnetization and the other is hard favouring high coercive values. In order to profit from the combination of the beneficial properties of the constituent phases the demagnetization behaviour of the composite material must be magnetically single-phase, i.e. the two phases must be exchange-coupled. The most important parameters to obtain a good exchange coupling between different phases are the dimensions, the relative amounts and the distribution of soft and hard ferromagnetic phases. In the last few years the attention has been addressed to the development of these magnets in the form of multilayers since they are simple systems that allow a good reproducibility and control during the growth process.

The exchange-spring systems show reversible magnetization curves and high values of the remanence to saturation ratio (M_r / M_s). These properties allow to obtain a strong increase of the maximum energy product $(BH)_{max}$ that represents the energy that can be stored by the magnet. This product can be deduced from the second quadrant of the hysteresis loop and is represented by the rectangular area shaded in Fig. 1.19. The maximum value of $(BH)_{max}$ can be achieved when $M_r / M_s = 1$ and the nucleation field at which the moment reversal occurs satisfies the following condition: $H_n \geq M_s / 2$. The materials that easily satisfy these requirements have strong uniaxial magnetocrystalline anisotropy able to overcome the demagnetizing effects: $K >> \left(\mu_0 M_s^2\right) / 4$.

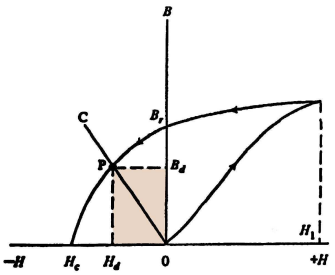

Figure 1.19 – Demagnetization curve, working point P and energy product $(BH)_{max}$ of a magnet.

The first theoretical model on systems having in-plane anisotropy is due to Kneller and Hawing[10]. Their work underlines the role played by the microstructure and the relative phase sizes in the developments of good exchange coupling between phases. This one-dimensional model considers a soft layer sandwiched between two hard layers with thickness d_s and d_h respectively (Fig. 1.20) exchange coupled at the interface.

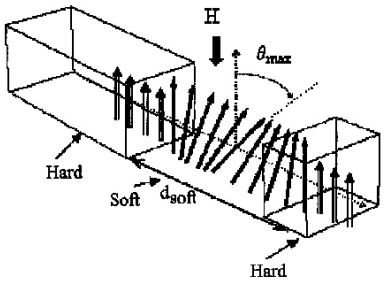

Figure 1.20 – Schematic representation of the system studied by Kneller and Hawing.

The domain wall energy is given by the anisotropy and the exchange energies that are defined respectively as

$$E_k = K \sin^2 \theta \tag{1.31}$$

$$E_{ex} = A\left(\frac{\mathrm{d}\psi}{\mathrm{d}x}\right)^2 \tag{1.32}$$

where the *x* direction is perpendicular to the *z*-field axis, θ is the angle between the direction of the magnetization vector and the easy axis and ψ is the angle between the magnetization and the *z* axis.

The domain wall energy per unit area, in a homogeneous material, is defined as:

$$\gamma = \delta K + \delta A\left(\frac{\pi}{\delta}\right)^2 \tag{1.33}$$

where δ is the wall width. At the equilibrium, the wall thickness is $\delta_0 = \pi\left(A/K\right)^{1/2}$ and the corresponding energy is $\gamma_0 = 2\pi\left(AK\right)^{1/2}$. Indeed the relative thickness of the hard and soft phases at the equilibrium are respectively $\delta_{0h} = \pi\left(A_h / K_h\right)^{1/2}$ and $\delta_{0s} = \pi\left(A_s / K_s\right)^{1/2}$.

If the soft layer thickness d_s is such that $d_s \approx \delta_{0s} >> \delta_{0h}$ the application of a field induces a reversible continuous rotation of the moments in the soft layer with the angle of rotation increasing with increasing distance from the hard layer. In effect the moments are free to rotate in the inner part of the soft layer, while they are completely pinned at the interface with the hard layer due to its strong anisotropy (Fig. 1.21)[12]. This feature can be reproduced within the simple picture of a domain wall.

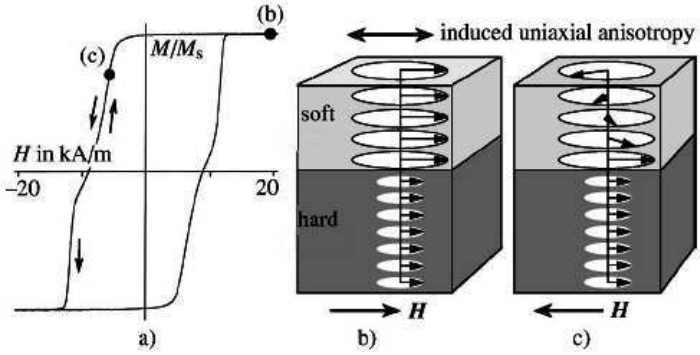

Figure 1.21 – (a) Easy axis magnetization curve, (b) and (c) schematic representations of the twisting of magnetization in the soft layer along the reversible branch of the hysteresis curve[11].

The field at which a first departure from saturation takes place is called *exchange-bias field* and can be expressed as follow:

$$H_{ex} = \frac{\pi^2 A_s}{2M_s d_s^2} \tag{1.34}$$

This field is independent on the thickness of the hard layer as long as $d_h >\approx 3\delta_h$ [13].

The moment orientation in the hard phase remains unchanged until the wall energy density in the soft phase overcomes the equilibrium wall energy density in the hard phase. At this point, the wall formed in the soft layer becomes progressively compressed at the soft/hard interface until it penetrates into the hard layer giving rise to a full irreversible moment rotation. The field at which this rotation occurs is called *nucleation* or *propagation field* and its intensity is strongly dependent on the soft layer thickness.

Figure 1.22 reports the behaviour of the reduced nucleation field as a function of the soft layer thickness as evaluated by Leineweber and Kronmüller[14] through a micromagnetic approach.

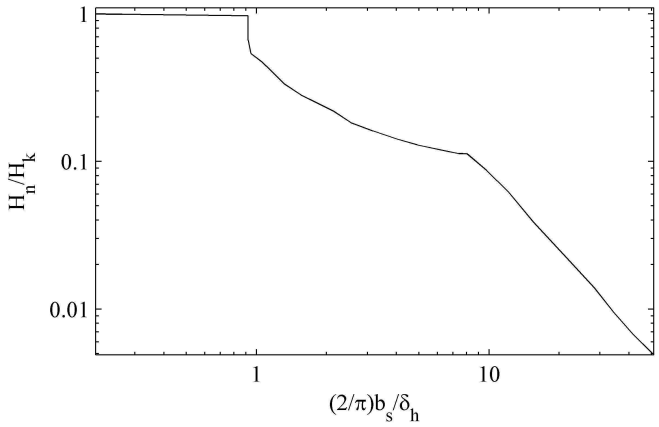

Figure 1.22 – Behaviour of the nucleation field normalized to the anisotropy field as a function of the soft layer thickness normalized to the domain wall width of the hard phase for a $Fe/Nd_2Fe_{14}B$ exchange spring magnet[14].

From Fig. 1.22, three regimes can be identified:

1. for $d_s << \delta_h$, the nucleation field is independent from the soft layer thickness and coincides with the value of the anisotropy field. The hysteresis loop is completely irreversible with the presence of only one critical field as in the case of a single-layer hard magnet. This is the "*hard phase regime*" characterized by a saturation magnetization and a nucleation field that can be evaluated through the weighted average of the saturation magnetization and coercivity respectively of the single layers[15]:

$$M = \frac{d_h M_s^h + d_s M_s^s}{d_h + d_s} \tag{1.35}$$

$$H_n = \frac{2\left(d_h K_h + d_s K_s\right)}{d_h M_s^h + d_s M_s^s} \tag{1.36}$$

2. for d_s a few times the δ_h, the nucleation field rapidly decreases by increasing the soft layer thickness. The hysteresis loops show two critical fields, the nucleation and the exchange one, and are characterized by both a reversible and an irreversible component. This regime is called "*exchange-coupled regime*". The hysteresis loop and a schematic image of the magnetic structure are reported in Fig. 1.23[16].

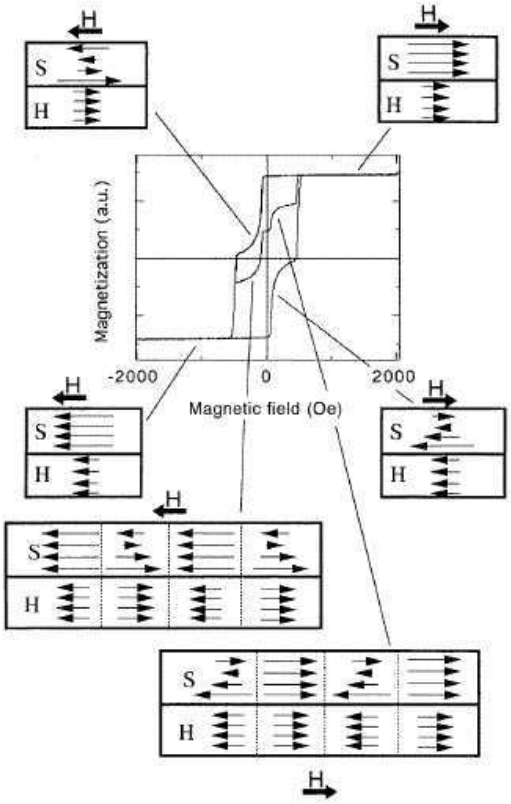

Figure 1.23 – Magnetization curve and schematic images of the corresponding magnetic structures[16].

3. for $d_s >> \delta_h$ the two phases are completely decoupled, and the nucleation field decreases with an inverse power of the soft layer thickness/diameter[17]:

$$H_n / H_k \sim d_s^{-c} \text{ with } c = \begin{cases} 1.750 \text{ for multilayers} \\ 0.762 \text{ for cubic soft inclusions} \\ 0.701 \text{ for spherical soft inclusions} \end{cases} \quad (1.37)$$

The decrease of the coercive field strength and the increase of the remanence ratio are due to the exchange interactions between nanoparticles. In effect, the interparticle exchange interactions, which favour a common parallel alignment of the moments, compete with the anisotropy which on the contrary favours their individual alignment along the easy magnetization direction of each crystallite.

Chapter 2

Experimental Techniques

In the present chapter an overview is given of the main experimental techniques employed in this thesis for the growth and characterization of magnetic thin films and exchange-spring magnets.

The growth of the films has been carried out with an UHV e-beam evaporation technique available at the Surface Laboratory of the University of Parma. Since the microstructural and magnetic properties of thin films are strongly dependent on the growing techniques and the energies involved during the deposition process, thin films have also been grown with a rf sputtering system available at the IMEM-CNR of Parma.

The microstructural and phase analysis have been realized through conversion electron Mössbauer spectroscopy (CEMS) in high vacuum using a 55 mCi ^{57}Co(Rh) source. The γ-rays incident angle was 20°. The spectra were fitted using a least squares minimization routine with a combination of linear and nonlinear regressions. The isomer shifts, *IS*, are referred to α-Fe. Morphology and magnetic domain configuration studies have been performed using an UHV atomic and magnetic force microscopy (AFM-MFM). The magnetic properties of the samples were measured using a Magneto-Optical Kerr Effect (MOKE) magnetometer with He-Ne laser light (Chapter 3). All these techniques are available at the Surface Laboratory.

The X-ray diffraction (XRD) patterns were recorded at the Department of Metals Science, Electrochemistry and Chemical Techniques of University of Bologna using a computer-controlled goniometer and Cu(K_α) radiation.

2.1 UHV e-beam Evaporation

The evaporation technique allows a controllable transfer of atoms from a heated source to a substrate located a distance away, where the film forms and grows[18]. The thermal energy is imparted to atoms in a solid source such that their temperature is raised to the point where they either evaporate or sublime. The main reason for the ascendancy of evaporation methods are the better vacuum and cleaner environments for film formation and growth and the general applicability to all classes of materials.

The evaporation rates are proportional to the difference between the equilibrium pressure P_e, of the material at a given temperature and the hydrostatic pressure P_h, acting on the evaporant. The maximum evaporation rate is achieved when the number of vapour molecules emitted corresponds to that required to exert the equilibrium vapour pressure while none return:

$$\Phi_e = \frac{\alpha_e N_a \left(P_e - P_h\right)}{\left(2\pi MRT\right)^{1/2}} \tag{2.1}$$

where Φ_e is the evaporation flux in number of atoms per unit area and per unit time, and α_e is the coefficient of evaporation, which is in between the values of 0 and 1. When $\alpha_e = 1$ and $P_h = 0$ the maximum evaporation rate is realized. The key variable influencing the evaporation rates is the temperature since it affects the equilibrium vapour pressures. In particular, the element sublimation is achieved only when a sufficiently high vapour pressure (greater than 10^{-3} torr) is reached by the material below the melting point.

The deposition of thin films involves consideration of both the source and the substrates upon which the evaporated atoms impinge; in effect the source-substrate geometry strongly influences film uniformity. The mass deposited per unit area is given by:

$$\frac{\mathrm{d}M_s}{\mathrm{d}A_s} = \frac{M_e \cos\phi \cos\theta}{\pi r^2} \tag{2.2}$$

where $\mathrm{d}M_s$ is the mass that falls on the substrate of area $\mathrm{d}A_s$, M_e is total evaporated mass, r the source-substrate distance and the ϕ and θ angles are the evaporated emission and the deposition/receiving angles respectively [Fig. 2.1(a)].

In real systems it has been found that a $\cos^n\phi$ evaporation law is more realistic, where n is a number that determines the geometry of the vapour cloud and the angular distribution of evaporant flux from extended sources [Fig. 2.1(b)]. Physically this number is related to the evaporation crucible geometry and scales directly with the ratio of the melt depth to the melt

surface area. Deep and narrow crucibles are characterized by large *n* and promote a strong confinement of the evaporated materials in a narrow angular spread.

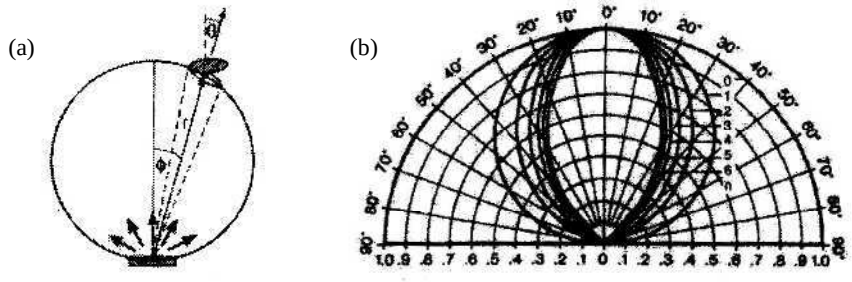

Figure 2.1 – (a) Schematic representation of evaporation from surface source. (b) Calculated vapour clouds with various cosine exponents.

The film thickness *d* is then given by:

$$\frac{d}{d_0} = \frac{1}{\left[1+\left(l/h\right)^2\right]^2} \tag{2.3}$$

where the variables are defined in the inset in Fig. 2.2(a). The maximum thickness d_0 is achieved for $l = 0$. The geometrical dependence of the film thickness uniformity must be taken into account when designing source-substrate geometry. The uniformity can be also promoted by rotating the substrate.

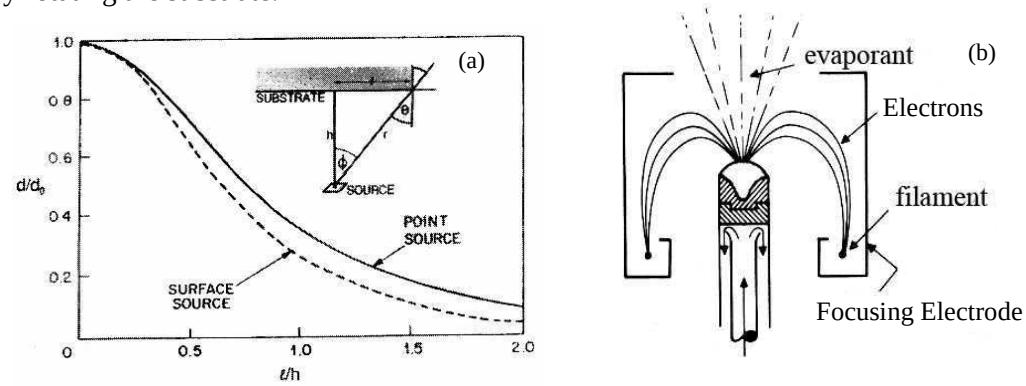

Figure 2.2 – (a) Film thickness uniformity. (b) Schematic representation of an e-beam gun.

Compared to the resistively heated evaporation sources, the *e-beam heating* eliminates the disadvantages of contamination by crucibles, heaters and support materials. The purity of the evaporant is assured because only a small amount of material melts or sublimes.

Electrons are thermionically emitted from heated filaments that are shielded from direct line of sight of the evaporant charge [Fig. 2.2(b)]. The cathode potential (3 – 20 kV) is biased negatively with respect to a grounded anode and serves to accelerate the electrons. Both magnetic and electric fields can be used to focus the e-beam on the material to be evaporated.

2.1.1 Nucleation and Growth of Thin Films

Three different mechanisms of film formation can be distinguished depending on the strength of interaction between the atoms of the film and the substrate: the *Van der Merwe mechanism* characterized by a layer by layer growth, the *Volmer-Weber mechanism* that is a three dimensional nucleation, forming, growth and coalescence of islands and *Stranski-Krastanov mechanism* characterized by the adsorption of a monolayer and the subsequent nucleation on top of this layer.

The Volmer-Weber mechanism is the most commonly type of growth and it can be divided into stages: (i) the nucleation during which small nuclei are formed statistically distributed over the substrate surface, then, (ii) after a certain concentration of nuclei is reached, additional particles do not form further nuclei but adhere to the existing ones causing their growth with the formation of larger islands and finally (iii) the coalescence of the islands with the formation of a more or less connected network containing empty channels. The different stages of thin film nucleation and growth from the vapour phase are shown schematically in Fig. 2.3.

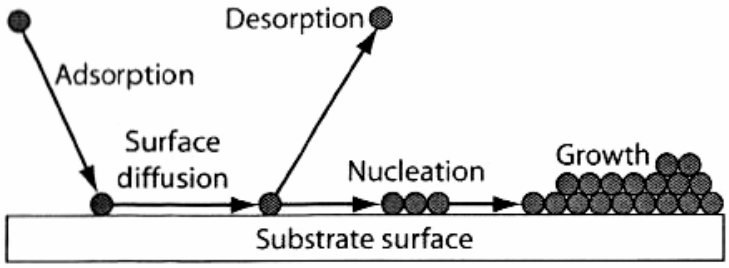

Figure 2.3 – Events in vapour-phase thin film growth process

The evaporant atom is attracted to the surface by the instantaneous dipole and quadrupole moments of the surface atoms, being physically adsorbed (*adatoms*). This atom can move over the surface (*surface diffusion*) by jumping from one potential well to another because of the thermal activation and/or its kinetic energy. Furthermore, this atom can be chemically adsorbed or can meet another particle forming a pair with a lower re-evaporation probability than a single particle. It is to be noted that the adsorbed particle tends always to occupy the state of minimum energy and thus to be localized in some adsorption points. To jump to another surface potential well it must overcome a certain potential barrier (the *activation energy*) strongly influencing the surface diffusion. If two adjoining nuclei, formed by several particles, are at a distance equal or lower than the mean distance that a particle can move on the surface from the point of incidence, the formation of additional nuclei is stopped and all other particles will join existing islands.

To ensure the formation of condensation nuclei, the evaporation rate must be sufficiently high, otherwise the migrating particle on the surface might re-evaporate before meeting another particle. The ratio of the impinging flow to the re-evaporation flow is called *supersaturation*. The condensation depends mainly on the ratio of two quantities: the *desorption energy* characterizing the binding of impinging atoms on the substrate and the *sublimation heat* determining mutual binding of the condensing atoms. If the desorption energy is much lower than the sublimation heat, the condensation occurs without supersaturation and the coverage is high, if the two quantities are comparable the condensation occurs at a moderate level of supersaturation. Finally if the desorption energy is much higher than the sublimation heat only a very small coverage is achieved.

The growth rate of an island is limited by the slower of the two processes cooperating in the growth: the surface diffusion and the interface transfer. The final coalescence can proceed in three ways:

- The Ostwald ripening: when particles with different radii are in contact, a larger nucleus forms at the expense of a smaller one. This process is more important for annealing after deposition than during deposition
- The coalescence due to mobility of islands
- The coalescence by growth: if two growing particles touch each other, they can either retain their shape (sintering or agglomeration) or they can coalescence into a single one.

2.1.2 Crystallographic Structure of Thin Films

There are essentially three different groups of films: amorphous, polycrystalline and monocrystalline. *Amorphous films* are characterized by a low surface mobility of adsorbed atoms so that the disordered state is frozen before the particles are able to reach the most preferable energetic sites. The amorphous state is a metastable state and the films easily recrystallize.

Polycrystalline films are systems characterized by a highly disordered state, where the directions of the crystallographic axes of the particles are randomly oriented. In these systems, despite the high degree of disorder, there may exist a few preferred orientations of the crystallographic axes, these directions are called *axes of texture*. If a unique texture is present, the film is *monocrystalline*.

The formation of monocrystalline films usually on monocrystalline substrates is called *epitaxy*. The resulting orientation of the film depends in each case on the crystal structure and on the orientation of the substrate. A fundamental parameter of epitaxial growth is the substrate

temperature. For every pair of materials a certain critical epitaxial temperature exists, in addition this temperature depends on the evaporation rate, which influences the time for an adatom to jump into a position of equilibrium before to collide with another particle.

2.2 Conversion Electron Mössbauer Spectroscopy (CEMS)

The Mössbauer effect represents the recoil-free nuclear resonance emission and absorption of gamma rays of atoms bound in solids. The probability of this effect is a function of the temperature, i.e. of the mean squared vibrational amplitude of the emitting nucleus in the direction of the γ-rays and the energy of the γ-rays, i.e. of the recoil energy of free atoms[19]. When γ-rays are emitted (or scattered) by an atom bound in solids, if the recoil energy (E_R) is larger than the binding energy (~25 eV), the atom will be displaced from its lattice site. If E_R is lower than the displacement energy but larger than the phonon energy (~10^{-2} eV), it is mostly converted into lattice vibrational energy. However, if the recoil energy is lower than the phonon energy, a new phenomenon takes place since the lattice is a quantized system which cannot be arbitrary excited. The emission of γ-rays can only be accompanied by transfer to the solid of integral multiples of the phonon energy. Therefore there is a probability *f*, called *recoil-free fraction* or *Lamb-Mossbauer factor* or *Debye-Waller factor*, that no transfer of energy occurs during the emission or absorption of γ-rays (*zero-phonon energy*). This probability can be expressed as:

$$f = \exp\left[-\frac{E_R}{k_B\Theta_D}\left(\frac{3}{2}+\frac{\pi^2T^2}{\Theta_D^2}\right)\right] \tag{2.4}$$

for $T << \Theta_D$ (the Debye temperature), and as

$$f = \exp\left(-\frac{6E_RT}{k_B\Theta_D^2}\right) \tag{2.5}$$

for $T > \Theta_D$, k_B is the Boltzmann factor. From the above expressions it is possible to conclude that the lower is the recoil energy i.e. the transition energy between two nuclear states, the higher is the recoil-free fraction. This also increases with decreasing the temperature while decreases with decreasing Θ_D.

In the γ-emission process when the lattice is not excited, the linewidths are only determined by the widths of nuclear levels involved in the transitions (~10^{-9} eV for τ ~10^{-7} s). This means

that, for energy of 10 keV the ratio of the width to the total energy of the γ-rays is ~10^{-12}. Therefore the zero-phonon-radiation is the most accurately defined electromagnetic radiation available. Moreover the linewidths associated with this effect are smaller than the characteristic energies of interaction of nuclei with the surrounding charges (*hyperfine interactions*), i.e. those arising from the coupling of the nuclear magnetic dipole moment with the magnetic electrons or those due to the coupling of nuclear electric quadrupole moments with the crystalline electric field gradient.

2.2.1 Hyperfine Interactions

Isomer Shift: Electric Monopole Interaction

The nucleus in an atom is surrounded and penetrated by electronic charges with which it interacts electrostatically. The electrostatic Coulomb interaction between the nuclear charge and electrons inside the nuclear region is usually called *electric monopole interaction*. A change in the electron density and in particular in *s*-electron density will result in an altered Coulomb interaction which manifests as a shift of the nuclear levels. The difference between the energy shift in the source and that in the absorber can be measured through the isomer shift *IS*. If the absorber is chemically or physically different from the source the electron densities at the Mössbauer nucleus in source and absorber will have different values.

Therefore the isomer shift can be expressed as:

$$IS = \frac{2\pi}{5} Ze^2 \left[\left|\psi_s(0)\right|^2 - \left|\psi_a(0)\right|^2 \right] \left(R_e^2 - R_g^2 \right) \tag{2.6}$$

where *e* and *g* indicate excited and ground states, *s* and *a* mean source and absorber respectively, *R* is the nuclear radius and $-e\left|\psi(0)\right|^2$ is the electronic charge density.

Quadrupole Splitting: Electric Quadrupole Interaction

The quadrupole splitting is the result of the interaction (called *electric quadrupole interaction*) between the nuclear quadrupole moment *Q* and an inhomogeneous electric field described by the electric field gradient at the nucleus. The nuclear quadrupole moment *Q* is a measurement of the deviations from spherical symmetry of the nuclear charge distribution of states. Flattened nuclei have negative quadrupole moments while elongated nuclei have positive moments.

The eigenvalues of the corresponding Hamiltonian contains only the second power of the nuclear magnetic spin quantum number m_I and therefore states whose m_I differ only in sign

remain degenerate. In a 3/2 → 1/2 transition, the electric quadrupole interaction gives rise to a doublet in the Mössbauer spectrum (Fig. 2.4), with the separation between the lines given by:

$$\Delta E_Q = \frac{e^2 qQ}{2}\left(1+\frac{\eta^2}{3}\right)^{\frac{1}{2}} \tag{2.7}$$

where η is an asymmetry parameter representing the electric field gradient.

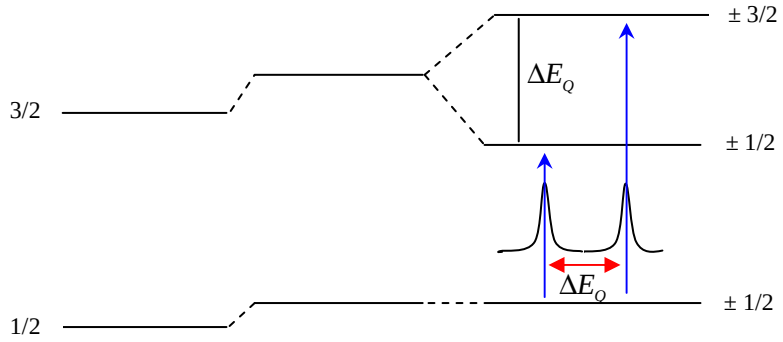

Figure 2.4 – The effect of the electric quadrupole interaction on the nuclear energy levels for a 3/2 → 1/2 transition.

The principal sources of the electric field gradient are the charges in incompletely filled shells and the charges surrounding the Mössbauer atom with non-cubic symmetry.

Magnetic Splitting: Magnetic Hyperfine Interaction

A nucleus with spin quantum number $I > 0$ has a non-zero magnetic dipole moment which may interact with a magnetic field *H* at the nucleus. This nuclear Zeeman effect is responsible of the nuclear state splitting with spin quantum number *I* into 2*I*+1 non-degenerate and equally spaced substates (Fig. 2.5). The allowed transitions between the levels of the excited state and those of the ground state are those obeying the selection rules.

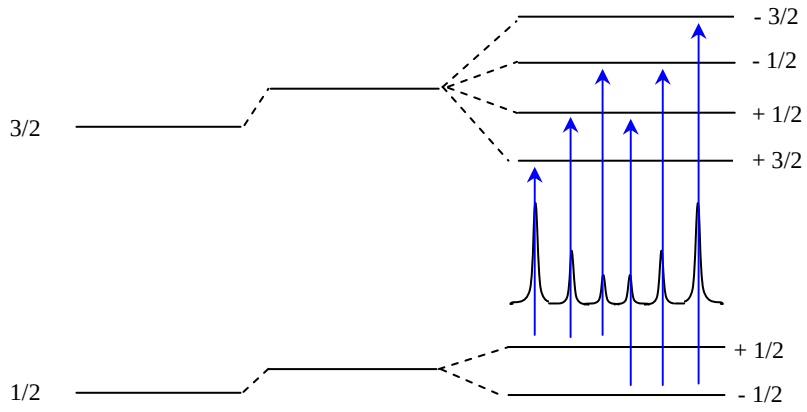

Figure 2.5 – The effect of magnetic splitting on the nuclear energy levels for a 3/2 → 1/2 transition in the absence of quadrupole splitting. The magnitude of the splitting is proportional to the total magnetic field at the nucleus.

For a 3/2 → 1/2 transition, the relative intensities of the six transition lines are given by the Clebsch-Gordan coefficients and depend on the angle θ between the incident γ-ray direction and the nuclear magnetic moment. From lowest to highest energies the relative lines intensities are in the ratio $3:x:1:1:x:3$ where $x=\frac{4\sin^2\theta}{1+\cos^2\theta}$. For random orientation of the magnetic moments $x=2$, for planar easy axis $x=4$ and for a perpendicular anisotropy $x=0$.

The observation of magnetic hyperfine splitting yields useful information about the magnetic order, the direction of easy magnetization, the magnetically non-equivalent lattice sites, the size of magnetic interactions, etc.

In general both magnetic dipole and electric quadrupole effects are present and this results in an asymmetric sextet (Fig. 2.6).

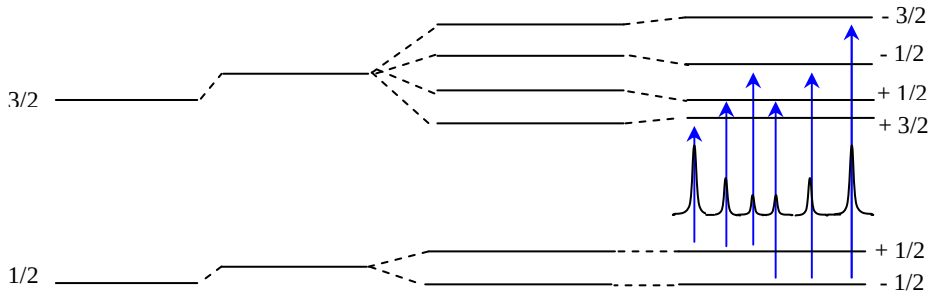

Figure 2.6 – Nuclear energy level splitting in the presence of both magnetic and electric quadrupole interactions.

2.2.2 Scattering Technique

A Mössbauer experiment consists in detecting the resonant excitation of nuclear states by means of γ-rays of appropriate energy, emitted by a radioactive source in a recoil-free fashion. The majority of experiments are performed in transmission geometry; this has the disadvantage to necessitate the use of thin foils or powders.

The scattering technique is a non–destructive tool which allows investigation of materials of nearly any shape. In these experiments it is possible to measure the γ-rays re-emitted by the resonant absorber, the X-rays or the electrons emitted via the *internal conversion process* (Fig. 2.7).

Depending on the kind and energy of the detected radiation, i.e. depending on the penetration power, spectra of surface layers of different thickness can be obtained. Moreover, in the case of the conversion electrons emerging at the surface, by selecting particular energies, it is possible to analyse at different depths, layers with thicknesses lower than their maximum penetration power. For the electron ranges, the upper limit is the estimated maximum thickness for stopping all electrons and the lower limit is the electron mean free path.

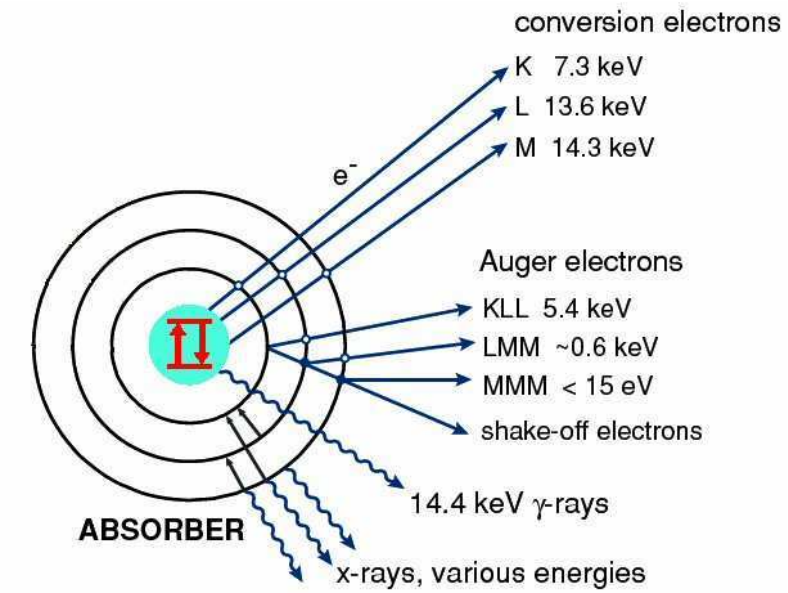

Figure 2.7 – Decay scheme of a ^{57}Fe nucleus after a resonant absorption of an incident gamma photon.

The analysis for different depths is performed by both selecting electron energies and selecting the direction of detection. In effect, the electrons are emitted isotropically but electrons of a given energy detected along the normal to the surface come from deeper regions than those detected at grazing angles.

2.3 UHV Atomic and Magnetic Force Microscopy (AFM-MFM)

Atomic and magnetic force microscopy allows the evaluation of local properties through the measurement of the deflection of a probe tip due to the interaction with the sample surface. The result is an image that represents respectively the topography and the magnetic pattern of the sample. The resolution is mainly given by the tip-sample distance.

The more commonly used measurement method is the *tapping mode*, where the cantilever is mechanically forced to oscillate at its resonance frequency above the sample surface. The interaction with the sample surface induces a phase or an amplitude shift of the cantilever oscillation.

The cantilever deflection is detected through an optical system constituted by a laser focused onto the tip and a position sensitive detector formed by four photodiodes (Fig. 2.8).

In the AFM, the tip is integrated into a cantilever (usually in Si-oxide or Si-nitride), which is deflected by the sample-tip interaction due to electric and Wan der Waals short-range forces. On the contrary in the MFM, the tip is covered by a thin magnetic layer and the image arises from the interaction of the tip with the magnetic stray field of the sample. This is possible when the tip experiences a gradient of the field perpendicular to the sample surface, i.e. when it passes between two opposite domains with perpendicular magnetization. Since these forces are of long-range interaction type, the magnetic image is performed at a greater distance from the sample surface with respect to that normally used in AFM. The possibility to perform measurements at different heights from the sample surface allows to record MFM images unaffected by the sample morphology.

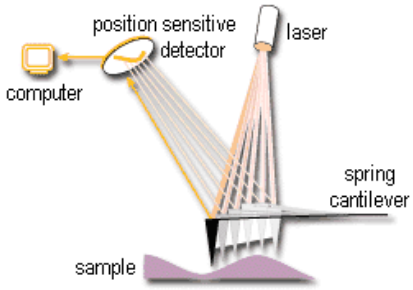

Figure 2.8 – Schematic representation of the optical system for the detection of the cantilever deflection.

Unfortunately the MFM signal is proportional to the product of the probe moment and the sample field gradients so that it is impossible to simultaneously maximize the resolution and field sensitivity. High resolution demands a small magnetically active volume of the probe, which leads to low moments and consequently to less interaction.

Performing MFM in vacuum conditions enhances the minimum detectable frequency shift of the cantilever[20], i.e.:

$$\delta f_{\min} = \sqrt{\frac{k_B T B f_0}{A^2 c Q}} \tag{2.8}$$

where k_B is the Boltzmann's constant, T the temperature, B the bandwidth of the measurement, f_0 the resonance frequency of the cantilever, A the amplitude and c the spring constant.

The minimum detectable force gradient is given by:

$$\left.\frac{\partial F}{\partial z}\right|_{\min} \approx 2c\frac{\delta f}{f_0} \tag{2.9}$$

Since the shift in frequency δf depends on the quality factor Q of the resonance curve, the sensitivity increases under ultra-high vacuum conditions since air damping is greatly reduced. Moreover it becomes possible to perform measurements of surfaces without protection layers and to reduce the effective tip to sample distance increasing the measurement resolution and sensitivity.

Chapter 3

Magneto-Optical Kerr Effect (MOKE)

The magneto-optical Kerr effect arises because of an optical anisotropy of magnetic materials induced by the magnetization *M*. This anisotropy alters the state of polarization of a linearly polarized light incident on a magnetic surface and induces, upon reflection, an elliptical polarization with a rotation of the major axis. In first approximation the Kerr rotation and ellipticity are linearly dependent on the magnetization, thus by measuring the change of the light polarization as a function of an applied magnetic field, a magnetic hysteresis loop can be obtained.

MOKE has emerged as an important technique in the study of surface magnetism since it is highly sensitive to the magnetization within the first ten nanometers. Other advantages of the MOKE include high accuracy, high temporal and spatial resolution and simplicity.

The main applications are the determination of electronic structure, observation of domains, investigation of oscillations in the coupling between ferromagnetic layers via intercalated non-magnetic metallic layers, and studies of two-dimensional Ising model behaviour of ultrathin layers. Furthermore MOKE has the advantage of a small sampling area, whose dimension is determined by the size of the laser beam. By using highly collimated laser spot, the uniformity in the magnetic properties of the film surface and the magnetic properties of single elemental dot arrays in patterned systems are allowed to be measured.

Since the Kerr rotation angle θ_K and ellipticity ε_K are typically small, i.e. $\sim 10^{-3}$ rad, optimization of the signal-to-noise ratio (S/N) is very crucial. Part of the Ph.D. work has been devoted to the increase of the (S/N) ratio, to the calibration of the Kerr angle and to the development of software for data acquisition allowing different types of magnetic measurements to be performed.

3.1 MOKE Principles

Light is a transverse electromagnetic wave which can be optically manipulated into plane, circularly or elliptically polarized light. Generally the plane of polarization is the plane containing the electric field $\vec{E}$ and the direction of propagation. If the electric field is polarized in the plane of incidence, it is referred as *p*-polarized light; conversely if the electric field is perpendicular to the plane of incidence it is referred as *s*-polarized light. The plane of incidence contains both the incident and the reflected light beam.

The microscopic origin of this effect lies in the spin-orbit coupling due to the interaction of the electric field of the light with the electron spin wavefunctions of the magnetic medium[21-24]. Formal approaches for calculating magneto-optical effects are based on a dielectric tensor theory[22,23]. Linearly polarized light can be decomposed into a right and a left circular polarized mode, RCP and LCP respectively. If the light is reflected from an isotropic and homogeneous material, the indices of refraction for the two circular modes are the same and therefore no rotation or ellipticity result. This occurs since the reflecting surface is a plane of symmetry for the system.

An anisotropic medium characterized by different indices of refraction for the RCP and LCP modes, induces linearly polarized light to become elliptically polarized with a rotation of the major axis. This rotation is caused by the different phase shift of the two modes and is linked to the real part of the refraction index. On the contrary, the imaginary part of the refraction index causes ellipticity because of the difference in the absorption rates of the two modes. In other words if a *p*-polarized light is reflected from a magnetic surface, the reflected light has a *p*-component as in the ordinary reflection but, in addition, a small *s*-component appears being out of phase with the reflected *p*-component (Fig. 3.1). Thus the magneto-optic response of a medium measured with MOKE consists of two parts: a change in the polarization of the in-phase component of the reflected light which gives rise to the rotation and a change in the polarization of the out-phase component that causes ellipticity.

In a magnetic medium the time-reversal symmetry is broken and separated wave vectors are required to describe the propagation of polarized light with left or right helicity. This introduces off-diagonal elements in the dielectric tensor. Assuming that the direction of the magnetization and the incoming light are both normal to the sample surface, $m_x = m_y = 0$, the dielectric tensor can be written as:

$$\tilde{\varepsilon}(\mathbf{M} \| z) = \begin{pmatrix} \tilde{\varepsilon}_{xx} & \tilde{\varepsilon}_{xy} & 0 \\ -\tilde{\varepsilon}_{xy} & \tilde{\varepsilon}_{xx} & 0 \\ 0 & 0 & \tilde{\varepsilon}_{xx} \end{pmatrix} \tag{3.1}$$

In this form, the tensor cannot be diagonalized and thus it affects the propagation of the two RCP and LCP modes.

Macroscopic descriptions of the optical and magneto-optical response relate measurable parameters such as reflectance and polarization changes to generate parameters that describe the media response (the dielectric tensor or the index of refraction). The formulas are based on Snell's law and utilize Fresnel transmission and reflection coefficients. Zak and co-workers[25-27] have derived such expressions for the ultra-thin film regime and more generally to multilayer configurations. They solved the boundary problem between different magnetic layers through a 4 × 4 *medium boundary matrix* whose elements are constructed from the geometric angles of the problem, from the index of refraction *n* and from a magneto-optic constant *Q* that accounts for all the quantum-mechanical effects responsible for MOKE i.e. the spin-orbit interaction. Furthermore, if there is more than one boundary, the wave propagation inside of the medium at depth *z* from the interface is described using a *medium propagation matrix*. The final goal is to obtain the Fresnel transmission *t* and reflection *r* coefficients.

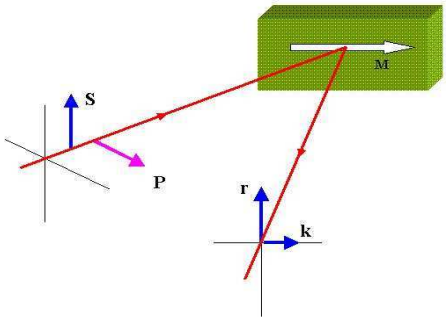

Figure 3.1 – Schematic representation of (*p*-) *s*-polarization of the incident light and the normal and Kerr components of the reflected light.

The Kerr effect given by the Kerr rotation and ellipticity for *p*- and *s*-polarized light are then expressed as:

$$\phi_p = \theta_K^p + i\varepsilon_K^p = \frac{r_{sp}}{r_{pp}} \tag{3.2}$$

$$\phi_s = \theta_K^s + i\varepsilon_K^s = \frac{r_{ps}}{r_{ss}} \tag{3.3}$$

where r_{ij} are the reflection coefficients that depend both on the index of refraction of the media, and on the angles of the light wave vector, measured from the normal to the sample surface. Notice that the r_{pp} and r_{ss} elements are the coefficients signifying how much of the original

polarized state is only reflected, while the off-diagonal elements, r_{sp} and r_{ps} give rise to the net rotation and elliptical polarization induced by the magneto-optical Kerr effect.

3.2 Geometric Configurations

There are principally three Kerr effects which are classified depending upon the geometry employed during the measurement (Fig. 3.2). The classification depends on the orientation of the magnetization with respect to the incident and the sample plane.

In the longitudinal Kerr geometry, the magnetization is in the plane of the sample and parallel to the incident plane. In this geometry, the Kerr effect is linearly dependent on the incident angle of the light respect to the sample surface, indeed it is possible to enhance the longitudinal MOKE signal by increasing this angle. In the limit of ultra-thin films ($2\pi|n_{med}|d/\lambda << 1$ where n_{med} is the refractive index of the magnetic layer with thickness d and λ is the wavelength of the polarized light)[27]:

$$\phi_{longitudinal} = \left(\frac{4\pi}{\lambda} \frac{n_{sub}}{1-n_{sub}^2} \right) Qd\theta \tag{3.4}$$

where n_{sub} is the refraction index of the substrate, Q is the magneto-optic constant of the magnetic layer and θ is the angle of incidence measured from the surface normal.

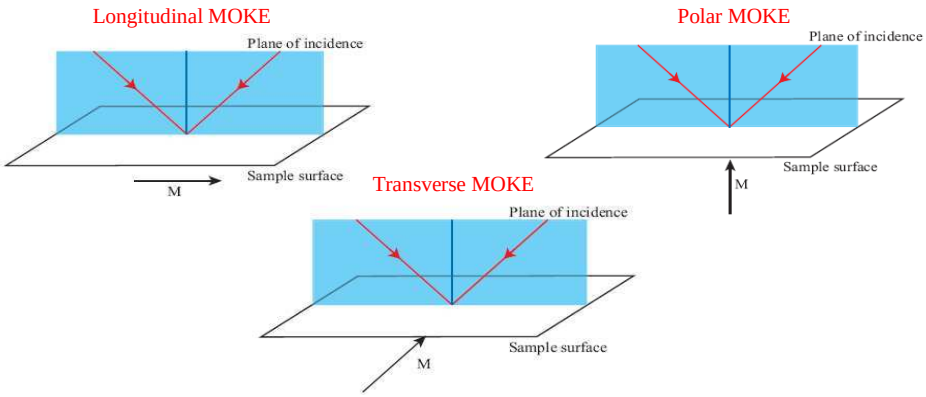

Figure 3.2 – Longitudinal, polar and transverse Kerr geometry.

In the polar geometry, the magnetization is perpendicular to the sample plane and parallel to the plane of incidence. In this configuration the Kerr effect is practically unaffected by the incident angle (for small angles) of the light[27].

$$\phi_{polar} = \left(-\frac{4\pi}{\lambda} \frac{n_{med}^2}{1 - n_{sub}^2} \right) Qd \tag{3.5}$$

Finally in the transverse geometry, the magnetization is in the sample plane but perpendicular to the incident plane. In this last configuration, no change of the light polarization occurs upon reflection. This can be understood by a simple picture where the electric field of the light can be thought of as exciting the electrons so that they oscillate parallel to the incident polarization. This gives rise in the reflected light to the normal component, which has the same polarization of the incoming light.

The Kerr component arises because of the Lorentz force that induces a small electric field component perpendicular to both the normal component and the direction of the magnetization. In the longitudinal and polar Kerr effects the *p*- or *s*-polarized light becomes elliptically polarized with its major axis rotated. The Kerr effect decreases as the angle of incident approaches the normal to the film plane in the longitudinal geometry because either the Lorentz force vanishes (*p*-polarization) or points along the direction of light (*s*-polarization). On the contrary, polar Kerr effect is a maximum for normal incidence because in this case the magnetization is out of the film plane and a Lorentz force always exists at normal incidence: the polar effect becomes independent on the incident polarization. The transverse effect involves no change in the polarization state since there is no Lorentz force present (*s*-polarized incident light) or the induced component (*p*-polarized) has the same polarization of the incident polarization. This last case involves only a change in the intensity of the light that depends upon the component of magnetization perpendicular to the plane of incidence.

The longitudinal and transverse geometries are used to study the in-plane magnetic anisotropy, whereas the polar effect is helpful in the study of systems with perpendicular anisotropy.

3.3 MOKE Magnetometer

The schematic representation of the MOKE set-up is reported in Fig. 3.3. The light is provided by an intensity stabilized, linearly polarized He-Ne laser (20 mW, 632.8 nm), whose polarization (either *p* or *s*) is controlled by a Glan-Thompson polarizer mounted on a computer controlled micro-stepper rotator. The Glan-Thompson polarizers are made of optical grade calcite in the form of a cube sliced diagonally such that the transmitted light is polarized along the optical axis and the rejected beam is polarized perpendicular to the transmitted one. This last

beam is not used during MOKE measurements and thus is blocked by ground black glass cemented onto the calcite. *S*-polarized light was preferentially used to minimize signals caused by the transverse Kerr effect. These can be caused by some small remnants of *p*-polarization. The light is then focused onto the sample. The reflected light passes through a photo-elastic modulator (PEM) that modulates the polarization of light at 50 kHz, and then through a second polarizer indicated as analyzer whose optical axes is fixed at 45°. The signal is measured through a Si-photoconductive diode.

The signal is then amplified and sent to a lock-in phase detector triggered at the PEM modulation frequency or at twice this frequency. A number of experiments were performed by examining the hysteresis loops at different amplifier and time constant settings to ensure that they had no other unwanted influences on the magnetic signal being measured.

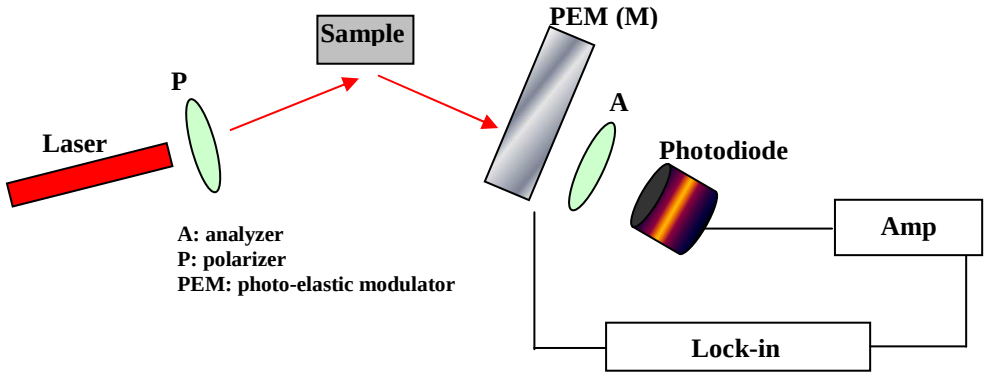

Figure 3.3 – Schematic representation of the MOKE magnetometer.

The magnetic field is provided by a computer controlled electromagnet (Walker Scientific Inc.) whose air-gap is regulated to give a uniform maximum field of 15 kOe calibrated through a Hall probe.

The MOKE software allows the control of the magnet through serial port communication and the data acquisition through a NIDAQ acquisition card. Assuming that both Kerr rotation and ellipticity are linearly dependent from the magnetization the plot of the lock-in output with respect to the applied field represents the magnetization behaviour as a function of the applied field.

The sample is mounted either on a micro-rotator and a micro-positioning allowing a precise positioning of the sample either parallel or perpendicular to the magnetic field.

3.3.1 Modulation Technique

The photoelastic modulator (PEM) is constituted by an optical and an electronic head. The optical head consists of a block of optically isotropic crystal and two piezoelectric transducers that create stress alternation at the resonance frequency f = 50 kHz. This optical head is driven at the resonance frequency through a voltage that is given by the electronic head. This stress alternation induces a different index of refraction along the stress-axis direction allowing the PEM to periodically retard the phase of one linear polarization component with respect to the orthogonal linear component. In effect, along the strained direction a time-dependent phase shift $\varphi = \varphi_0 \sin 2\pi ft$ at frequency f = 50 kHz between the incoming light polarization components is induced. The optical response, treated in the Jones formalism for each optical element is reported in the follow.

If the polarizer transmits only *s*-polarized light ($\mathbf{J}_{\text{in}}$), the polarization state $\mathbf{J}_{\text{out}}$ at the detector is:

$$\mathbf{J}_{\text{det}} = \mathbf{A}(45°)\mathbf{M}\mathbf{S}\mathbf{J}_{\text{in}} = \frac{1}{2}\begin{bmatrix} 1 & 1 \\ 1 & 1 \end{bmatrix}\begin{bmatrix} e^{i\varphi/2} & 0 \\ 0 & e^{-i\varphi/2} \end{bmatrix}\begin{bmatrix} r_{ss} & r_{sp} \\ r_{ps} & r_{pp} \end{bmatrix}\begin{bmatrix} 1 \\ 0 \end{bmatrix} \tag{3.6}$$

where **A** is the matrix representing the analyzer with its optical axis set at 45°, **M** is the PEM matrix and **S** is the sample matrix. The light intensity measured by the detector is:

$$I_{out} \approx \left|r_{ss}\right|^2 + 2\left|r_{ss}\right|^2\left(-\theta_K^s \cos\varphi - \varepsilon_K^s \sin\varphi\right) \tag{3.7}$$

where the small quadratic $\left|r_{sp}\right|^2$ and $\left|r_{ps}\right|^2$ terms have been neglected. Using the Bessel functions J_i, $\sin\varphi$ and $\cos\varphi$ can be expanded up to the second harmonic modulation frequency. The $\left|r_{ss}\right|^2$ term represents only a DC component I_0 of the signal, by normalizing the light intensity the measured fundamental (f) and second harmonic $(2f)$ quantities are:

$$\frac{I_{out}(f)}{I_0} = \frac{-4J_1(\varphi_0)\varepsilon_K^s}{1-2J_0(\varphi_0)\theta_K^s};\ \frac{I_{out}(2f)}{I_0} = \frac{-4J_2(\varphi_0)\theta_K^s}{1-2J_0(\varphi_0)\theta_K^s} \tag{3.8}$$

For $\varphi_0 = 140°$, $J_0 = 0$ and the denominator becomes equal to 1, and the f and 2f Kerr signals are rigorously proportional to the Kerr ellipticity ε_K^s and rotation θ_K^s. Other important values for φ_0 are 108° and 175° which maximize the J_1 and J_2 Bessel functions respectively.

Figure 3.4 shows a schematic explanation of the reason why the f and 2f components of the detected signal represent Kerr ellipticity and rotation respectively[28]. Curve (a) shows the time dependence of the retardation produced by the PEM. If $\varphi_0 = \pi/2$, the maximum and minimum of φ correspond to circularly polarized light. Without magneto-optic effects, the vector loci of

the electric field are illustrated in (b). The projection of this field along the *x*-axis (corresponding to the optical axis of the PEM) is constant against time (c). When a difference between phase shifts of the right and left circularly polarized light exists, the plane of the linearly polarized light rotates (Kerr rotation) producing a change of only the *x*-projection of the electric field with the appearance of a 2*f* component (e). No changes of the electric field vector loci occur (d). On the contrary, if ellipticity is present, the vector length of RCP and LCP become different (f) resulting in the appearance of a *f* component in the *x*-projection (g).

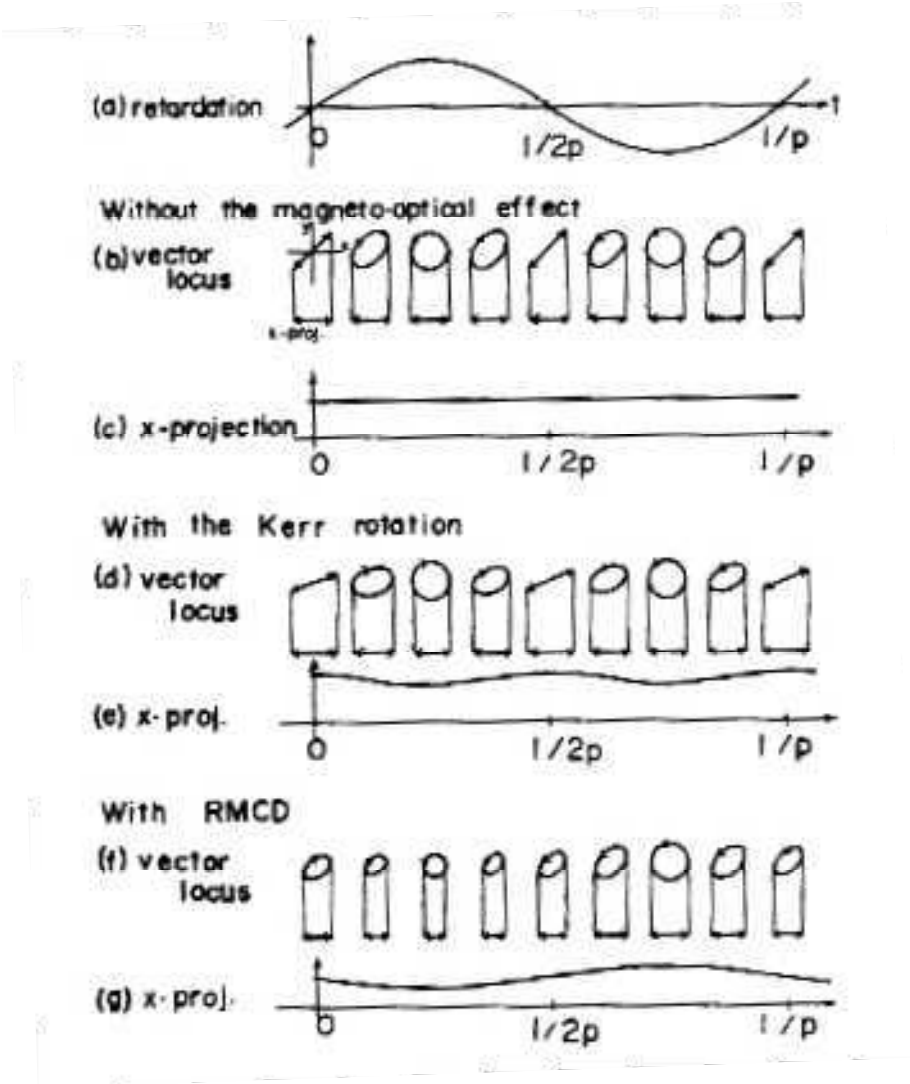

Figure 3.4 – Schematic illustration of the effect of the modulator on the detected MOKE signal.

3.3.2 MOKE Acquisition Software

The software has been written to automate the system in MATLAB language and then converted into a C-language executable, it is user-friendly and straight forward to use. The software (Fig. 3.5) is constituted by a series of control panels.

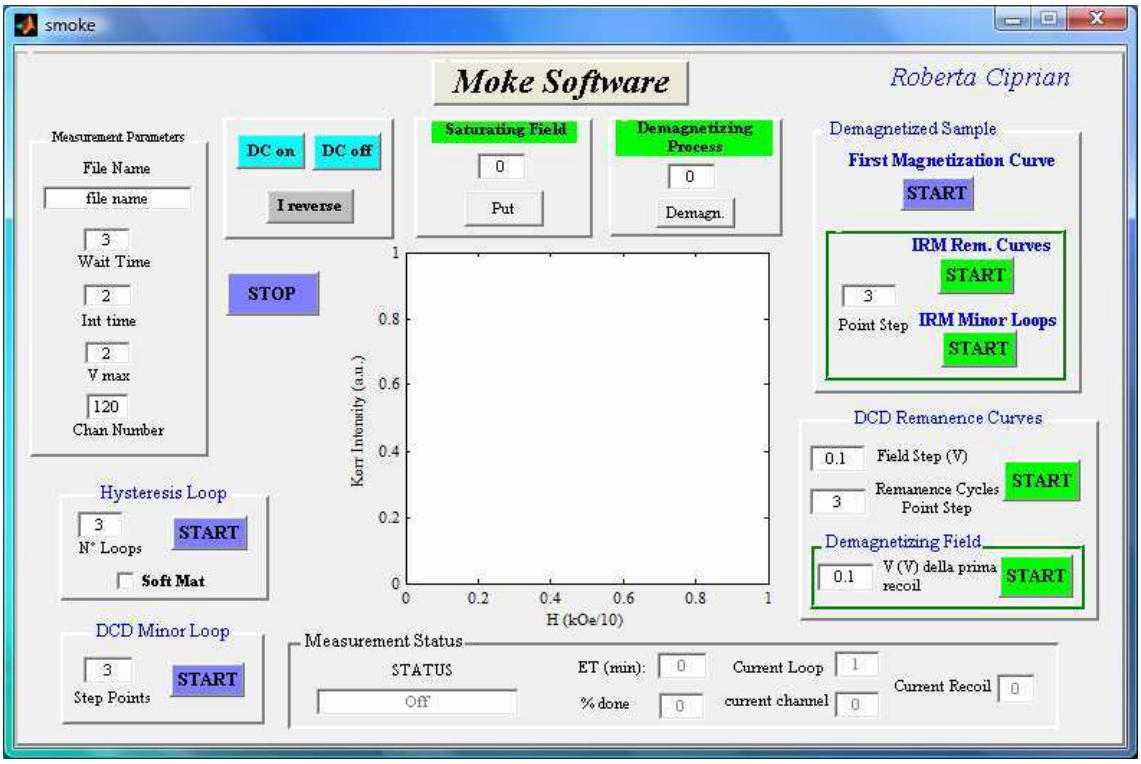

Figure 3.5 – MOKE acquisition software.

The **Measurement Parameters panel** allows setting a number of user-adjustable parameters. The main ones are:

- *File Name:* data are stored in txt files with the chosen filename followed by a number indicating the number of loop, recoil or minor loop taken. The possibility to save data after each measurement cycle allows to perform long-time consuming measurements avoiding the loss of all the work if a black-out occurs
- *Chan Number:* is the number of points acquired for each hysteresis loop, typically 124 points are taken. The only limitation to the number of points is given by the minimum voltage corresponding to the lowest sensitivity of the magnet power supply (0.02 V).
- *Wait-Time:* is the time in second that allows the stabilization of the applied field. This time is influenced by the time constant set on the lock-in, that determines the time necessary to the instrument to stabilize on the real value of the output signal. Moreover this time combined

with the point number determines the field sweep rate. If this time is not properly selected an overestimation or an underestimation of the time-dependent magnetic properties (in particular of the coercive field value) occurs.

- *Int. Time:* is the integration time i.e. the time of measurement for each point of the field ramp. Since the sampling frequency has been set at 1 kHz, the software makes an average of all the acquired data during the integration time. If this time is much greater an error occurs because of the electronic and thermal noise.
- *V max:* is the maximum voltage applied to generate the field ramp. Its value is only determined by the sample since it represents the field necessary to lead the sample in the saturated state.

The types of measurement that can be performed are:

Hysteresis Loops:

A number of hysteresis loops in sequence can be acquired allowing to reduce the electronic and thermal noise in the measurements.

Each loop starts with the sample in the saturated state that can be achieved through the **Saturating Field panel** that asks for the voltage to be applied. A flow diagram of the hysteresis loop measurements is reported in Fig. 3.6.

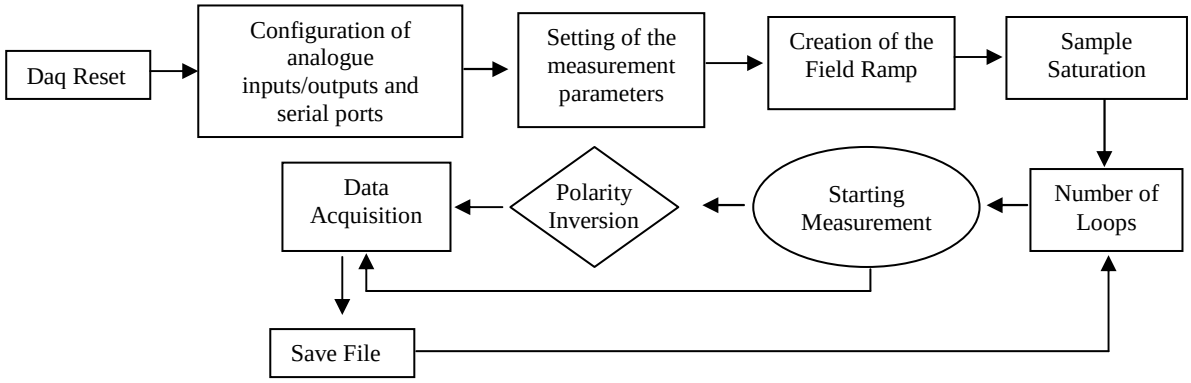

Figure 3.6 – Flow diagram of the hysteresis loop measurements.

First Magnetization Curves:

This type of analysis gives information about the mechanism controlling the coercivity (see 1.6.3 Section). Before starting the measurement process, the sample must be demagnetized. This can be done through the **Demagnetizing Process panel** after setting the starting voltage. The demagnetization process is performed by applying alternatively positive and negative fields of increasing intensity.

DCD Remanence Curves:

These curves are measured starting with the sample in the saturated state and then applying increasing negative field. The remanence is recorded after reducing the field to zero. The flow diagram is reported in Fig. 3.7. In the case of films with perpendicular anisotropy, a careful evaluation of the demagnetizing field is crucial for remanence curve analysis (see Section 3.4.1). For this reason a routine has been written (**Demagnetizing Field panel**) that allows to acquire the recoil curves until the sample returns in the saturated state [Fig. 3.8(a)]. This last procedure is much time consuming and can be avoided in the case of in-plane anisotropy.

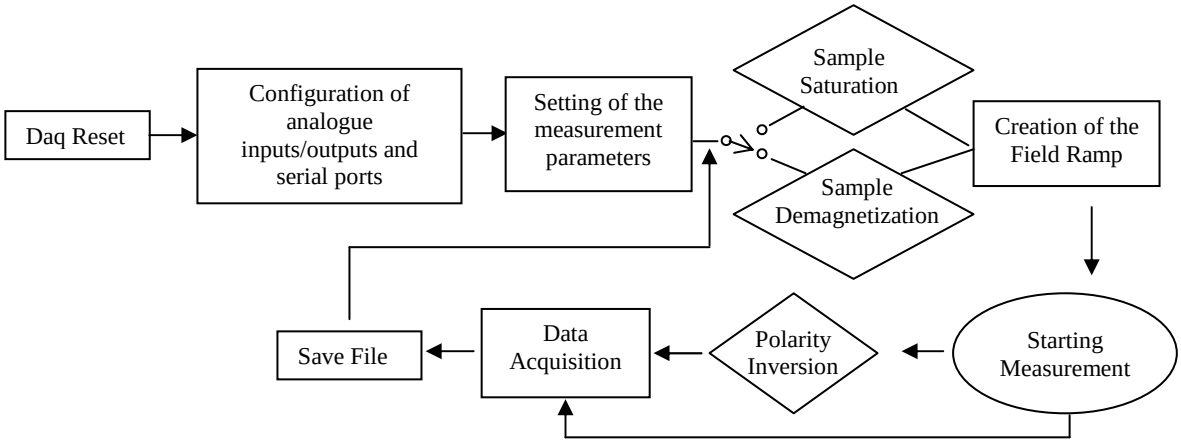

Figure 3.7 – Flow diagram of DCD and IRM remanence curve measurements.

IRM Remanence Curves:

The recoil curves are measured by applying successively larger applied fields to a previously demagnetized sample and measuring the remanence. By plotting the values of the remanence as a function of the maximum applied field for each recoil loop, the IRM remanence curve is obtained [Fig. 3.8(b) dotted curve].

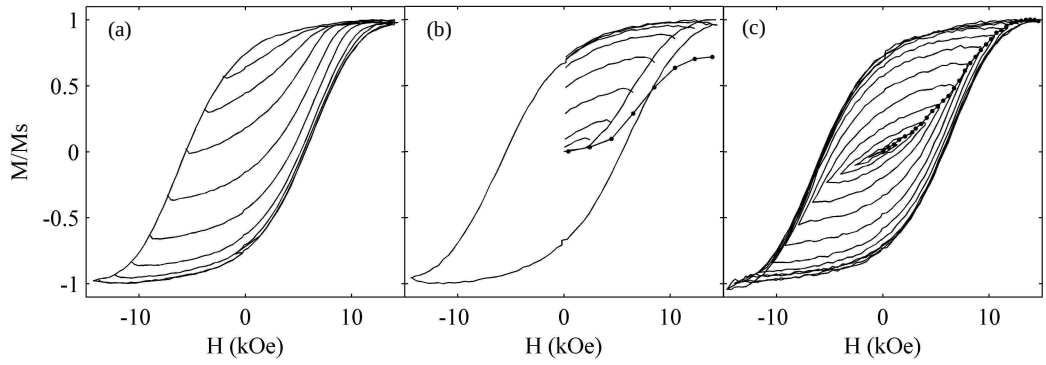

Figure 3.8 – (a) DCD recoil curves, (b) IRM recoil curves and the extrapolated IRM remanence curve (dotted line) and (c) minor loops recorded for a FePt sample with perpendicular anisotropy.

Minor Loops:

This measurement can be performed starting either from the saturated (**DCD Minor Loop**) or from the demagnetized state (**IRM Minor Loops**) of the sample. An example is reported in Fig. 3.8(c).

The **Measurement Status panel** gives:

- *STATUS*: indicates the software actions and the measurement status,
- *ET (min):* indicates the time for the whole measurement,
- *Current Loop:* shows the number of the loop that the program is performing,
- *%done:* is the hysteresis loop percent performed,
- *Current Channel*: is the point of the loop being measured and
- *Current Recoil:* is the recoil being performed during minor loop and remanence curve measurements.

3.3.3 Calibration of the Kerr Rotation Measurements

Two are the main methods to calibrate the Kerr rotation angle, which are referred as the *two-angle* and *the compensation methods*. They are used to determine the absolute values of the Kerr quantities. The method of two-angles involves intensity signals recorded at different time and therefore it has a strong sensitivity towards fluctuations of the light intensity. For this reason, this method has been discarded and the compensation method has been applied to all the measurements[29].

The phenomenological demonstration of the calibration procedure can be done by calculating the optical response of the MOKE setup through the Jones matrix formalism followed in the 3.3.1 Section. The only difference in this case is the angle α of the polarizer that is left variable.

The intensity of the reflected light I_{out}, in the case of polar configuration with perpendicular incidence, becomes:

$$I_{out} = I_0 + I_w \varepsilon_K \sin wt + I_{2w} \theta_K \cos 2wt \tag{3.9}$$

where:

$$\begin{aligned} I_0 &= A + BJ_0(\varphi_0)\theta_K \\ I_w &= 2CJ_1(\varphi_0) \\ I_{2w} &= 2BJ_2(\varphi_0) \end{aligned} \tag{3.10}$$

A, *B*, and *C* depend both on the Fresnel reflection coefficients and on the α angle of the polarizer:

$$\begin{aligned} A &= |r_{ss}|^2 + |r_{sp}|^2; \\ B &= \sin 2\alpha \left(|r_{ss}|^2 - |r_{sp}|^2 \right) - 2 r_{ss} r_{sp} \cos 2\alpha \\ C &= 2 r_{ss} r_{sp} \end{aligned} \tag{3.11}$$

The normalized lock-in signals at *f* and 2*f* directly yield the Kerr rotation and ellipticity respectively. By driving the PEM at the frequency of 50 kHz with an amplitude of 140° value, $J_0 = 0$ and $I_0 = A$.

Inspection of I_{2w} equation yields a procedure for a calibrated measurement of θ_K. In effect, by controlling the α angle of the polarizer, it becomes possible to compensate for I_{2w} i.e. $I_{2w} = 0$. Since $|r_{ss}|^2 >> |r_{sp}|^2$ and $\alpha \to 0$:

$$\frac{1}{2} \tan 2\alpha \approx \alpha = \theta_K \tag{3.12}$$

Equation 3.12 shows that the orientation α of the polarizer immediately yields θ_K. Absolutely calibrated hysteresis loops may thus be recorded point-by-point.

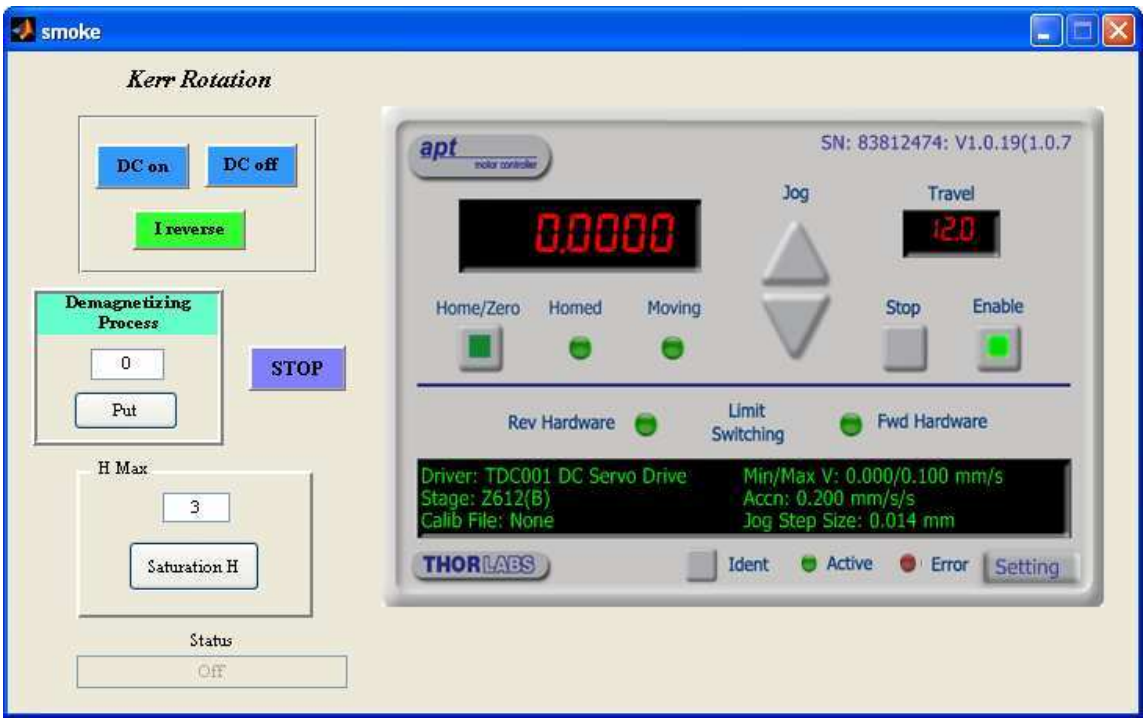

Figure 3.9 – Software for the calibration of the Kerr rotation angle

This procedure is totally unaffected from the signal amplification, from the filter and the amplification factors of the lock-in phase detector and from the fluctuations of the light intensity.

For the application of this procedure, the MOKE magnetometer has been equipped with a computer controlled micro-stepper rotator that allows an optimal control on the polarizer rotation. Dedicated software has been developed using MATLAB language that takes advantages of the "activex" controls provided with the micro-stepper (Fig. 3.9).

Since the micro-stepper rotation was calibrated by the manufacturer in mm, a correspondence between the position in mm and the rotation of the polarizer in degree has been found: 0.0275 mm ≡ 0.05°. Adjusting the acceleration and velocity through the proportional and integral blocks of the PID (proportional-integral-derivative controller) controlling the stepper-motor, the error during the measurements has been reduced to $\pm 0.001°$, allowing an optimal reproducibility. Within 1°, a linear relation has been found between the distance covered in mm and the rotation evaluated in degree (Fig. 3.10).

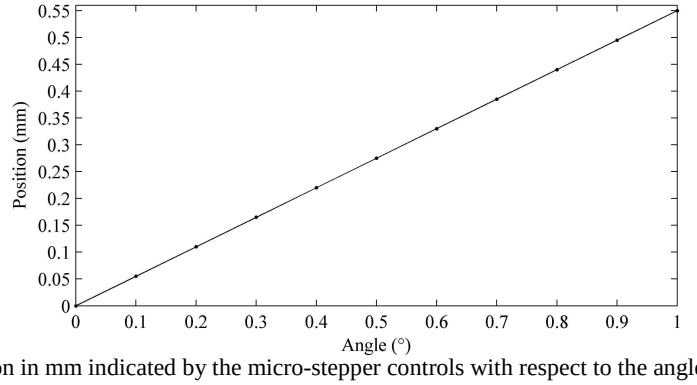

Figure 3.10 – Position in mm indicated by the micro-stepper controls with respect to the angle of rotation in degree.

Before each measurement, the samples are demagnetized (**Demagnetizing Process**). This allows to compare the Kerr rotation angles of different samples at fixed magnetic field values, also in the case of samples that cannot be led to the complete saturation because of their extremely hard magnetic properties.

Furthermore the Kerr rotation has been correlated to the values of the magnetization in emu/cm^3 measured with an AGFM magnetometer (IMEM-CNR) (Fig. 3.11). The samples used for the calibration are:

- $Fe_{52}Pt_{48}$ films, 30 nm thick, grown on Pt underlayers with different thickness: 2, 10, 50 and 100 nm
- Fe_xPt_{100-x} films grown on a 50 nm thick Pt underlayer, with x = 47, 50, 52, 58 at.%.

All the samples have been grown at 550°C with rf sputtering onto MgO (100) monocrystalline substrates. The values of the saturation magnetization as evaluated from AGFM and the corresponding Kerr rotation angles are reported in Table I.

Table I. Magnetization values (emu/cm^3) and polar Kerr rotation angles of sputtered FePt thin films measured with AGFM and MOKE magnetometers respectively

Samples	**M_s (emu/cm^3)**	**θ_k (°)**
$Fe_{52}Pt_{48}$/Pt(2 nm)	670	0.234
$Fe_{52}Pt_{48}$/Pt(10 nm)	625	0.200
$Fe_{52}Pt_{48}$/Pt(50 nm)	685	0.261
$Fe_{52}Pt_{48}$/Pt(100 nm)	411	0.105
$Fe_{47}Pt_{53}$/Pt(50 nm)	449	0.125
$Fe_{50}Pt_{50}$/Pt(50 nm)	523	0.148
$Fe_{58}Pt_{42}$/Pt(50 nm)	882	0.545

A few values found in literature[30-33] are also reported in Fig. 3.11. Since these data are related to samples not constituted by Fe and Pt, also measured in longitudinal geometry, the good agreement between these and our data allows to conclude that the anisotropy and its strength do not influence the Kerr rotation angle but only determines the shape of the hysteresis loops.

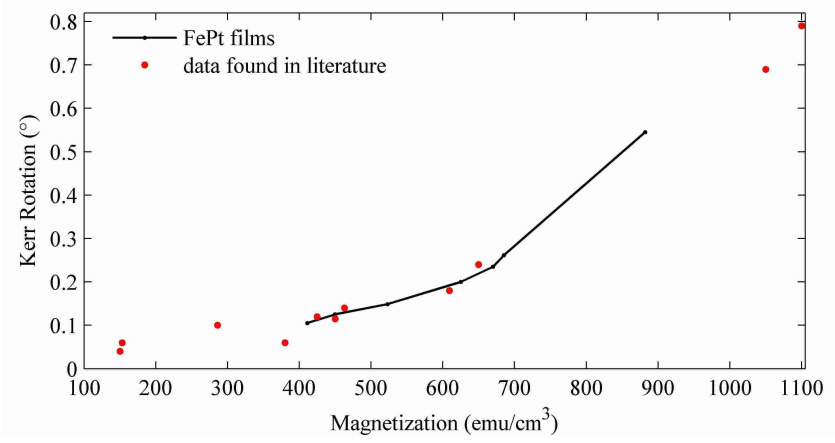

Figure 3.11 – Kerr rotation angle (°) with respect to the magnetization (emu/cm^3) measured for FePt films (—) and a few values found in literature (●)[30-33].

3.3.4 Data Processing

For the data analysis a dedicated software has been developed (Fig. 3.12). This software is subdivided into panels, i.e. hysteresis loop, DCD remanence curves, etc. that allow the post-processing of different types of data. In effect, data obtained from different types of

measurements need of proper and “ad-hoc-developed” routine for data normalization and averaging, allowing to eliminate thermal and electric noise. Moreover, this software automatically gives the coercive field, the remanence to saturation ratio and the demagnetizing field values.

The possibility to reject a few data and to perform a soft smoothing has also been included. The smoothing is preformed through a one-dimensional median filtering procedure, a nonlinear technique that applies a sliding window to a sequence. The median filter replaces the center value in the window with the median value of all the points within the window. This procedure allows to simultaneously reduce noise and preserve the edges and shapes of the hysteresis loops.

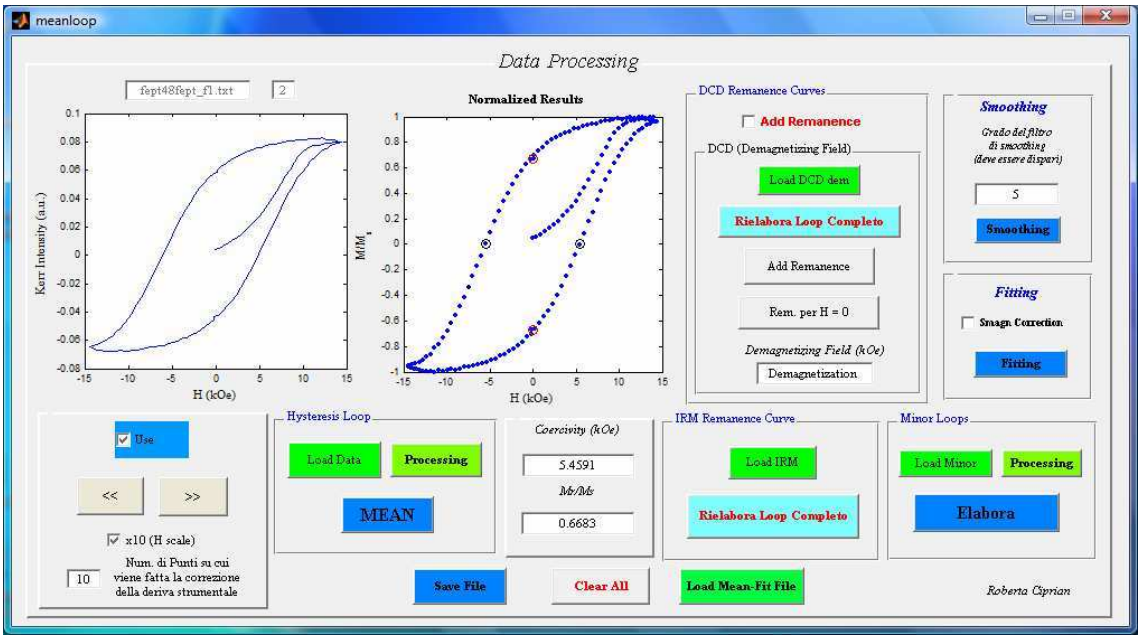

Figure 3.12 – Main window of the data processing software.

3.4 Remanence Curve Analysis

The remanence curves allow to study the degree of exchange-coupling among different magnetic layers and phases. In effect, the remanence obtained at a given value of field represents the sum of the magnetization components of the grains that have irreversibly switched into the field direction. Moreover from the differentiation of the DCD remanence curve the irreversible susceptibility can be obtained whose width at half maximum is a measurement of the switching field distribution:

$$SFD(H) = \left(\frac{\mathrm{d}M(H)}{\mathrm{d}H} \right) \cdot \frac{1}{H_c} \tag{3.13}$$

where $SFD(H)\mathrm{d}H$ is the fraction of magnetic particles and domains reversing their moments in the field range from *H* and *H*+d*H*. Since the starting state of the sample is the saturated one, where no domain walls are present, the irreversible susceptibility represents the energy barrier distribution to the nucleation of a reversed domain[34-35].

Contrary to the DCD remanence curve the irreversible susceptibility obtained by differentiating the IRM curve is a measurement of the energy barrier distribution to the domain wall pinning/depinning mechanism. This is due to the fact that the starting magnetic state of the sample is the demagnetized one where a multi-domain configuration is present, and therefore the irreversible susceptibility represents the strength of the pinning mechanisms to the wall motion.

The nature of interparticle interactions can be studied through the remanence curves since they are due to irreversible magnetization changes. The Wohlfarth relation:

$$M_r^{DCD}(H) = 1 - 2M_r^{IRM}(H) \tag{3.14}$$

which holds for any system of noninteracting single-domain particles, relates the isothermal remanence curve $M_r^{IRM}(H)$ to the DCD demagnetization remanence $M_r^{DCD}(H)$. Therefore interparticle interactions can be characterized through the *interaction-based deviation parameter* $\Delta M(H)$ as a function of the applied field:

$$\Delta M(H) = \frac{M_r^{DCD}(H)}{M_r} - \left[1 - 2\frac{M_r^{IRM}(H)}{M_r}\right] \tag{3.15}$$

where the remanence curves are both normalized to the saturation remanence magnetization M_r. The parameter ΔM is therefore, a direct measure of any deviation from the noninteracting case. Positive values of ΔM are a fingerprint of exchange interactions promoting the magnetized state whereas negative values are caused by interactions favouring the sample demagnetization[34-35].

3.4.1 Demagnetizing Field Influence on Magnetic Analysis

The demagnetizing fields strongly influence the magnetic properties of samples having perpendicular anisotropy. The result consists in a significant change of the total field value.

In principle it is possible to correct the magnetization curves by assuming that the demagnetizing field is $-4\pi M$. However in many films and multilayers this correction appears to be not applicable. The presence of strong intergranular exchange coupling and particle sizes result in cooperative reversal causing distorted hysteresis loops if the demagnetizing field is

taken at its maximum value[9]. Figure 3.13(a) shows a hysteresis loop as recorded (black line) and after the correction for demagnetizing effects (dotted blue line). Without this correction wrong information about magnetization reversal can be obtained.

In effect, the knowledge of the appropriate demagnetizing factor is crucial in the remanence curve analysis. These curves are evaluated from data recorded after the application and the subsequent removal of magnetic fields of different intensity, assuming the sample in the remanent state. However, when a significant demagnetizing field is present, the sample for zero applied field is not in the true remanent state, and the remanence curves are evaluated in the negative internal field ($-NM$) of the sample.

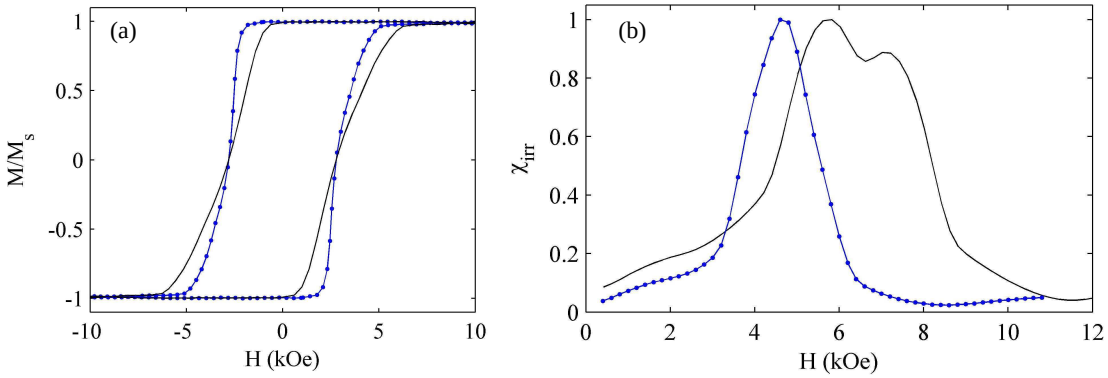

Figure 3.13 – (a) Hysteresis loop and (b) the irreversible susceptibility as obtained by differentiating the IRM remanence curve with respect the field as measured (—) and after the demagnetizing field correction (—●—).

The presence of this negative internal field also causes errors in the analysis of the grain interactions both by inducing negative values in the ΔM plots and by changing the irreversible susceptibility. For an incorrect *N*, the χ_{irr} width increases [Fig. 3.13(b)] and nonzero values are obtained for zero applied fields.

3.5 Comparison Between AGFM and MOKE

To check the performances and the resolution of the MOKE magnetometer, the magneto-optical measurements performed on FePt thin films with perpendicular anisotropy have been compared with those obtained by AGFM (Alternating Gradient Force Magnetometer) available at the IMEM-CNR. The AGFM has been chosen for its resolution greater than 10^{-8} emu and sensitivity that is thousand times greater than that of a VSM (Vibrating Sample Magnetometer).

The FePt films, 30 nm thick, have been grown by rf sputtering at 550°C on a Pt underlayer, previously deposited onto MgO (100) monocrystalline substrates. Both the thickness of the Pt underlayer and the stoichiometry of the FePt films were varied.

The magneto-optical and magnetic measurements have been carried out with the field applied both parallel and perpendicular to the film plane. The measurements performed with AGFM are reported in Fig. 3.14 and those measured with MOKE in Fig. 3.15.

The shapes of the hysteresis loops measured with the two magnetometers remain practically unchanged. The absence of distortions in the MOKE measurements and the presence of all the figures of merit of the loops measured with the AGFM suggest that the sensitivity and resolution of the MOKE is very high, allowing performances well comparable with those of an AGFM magnetometer.

It is to be noted that MOKE measurements performed with the field applied along the hard magnetization axis are often not reported in literature, since the small Kerr rotation and the increased intensity of the second order Kerr effects make very difficult to perform this type of measurements. Our MOKE allows measurements of the hysteresis loops with the field both perpendicular and parallel to the easy magnetization axis, giving satisfactory results (Fig 3.15).

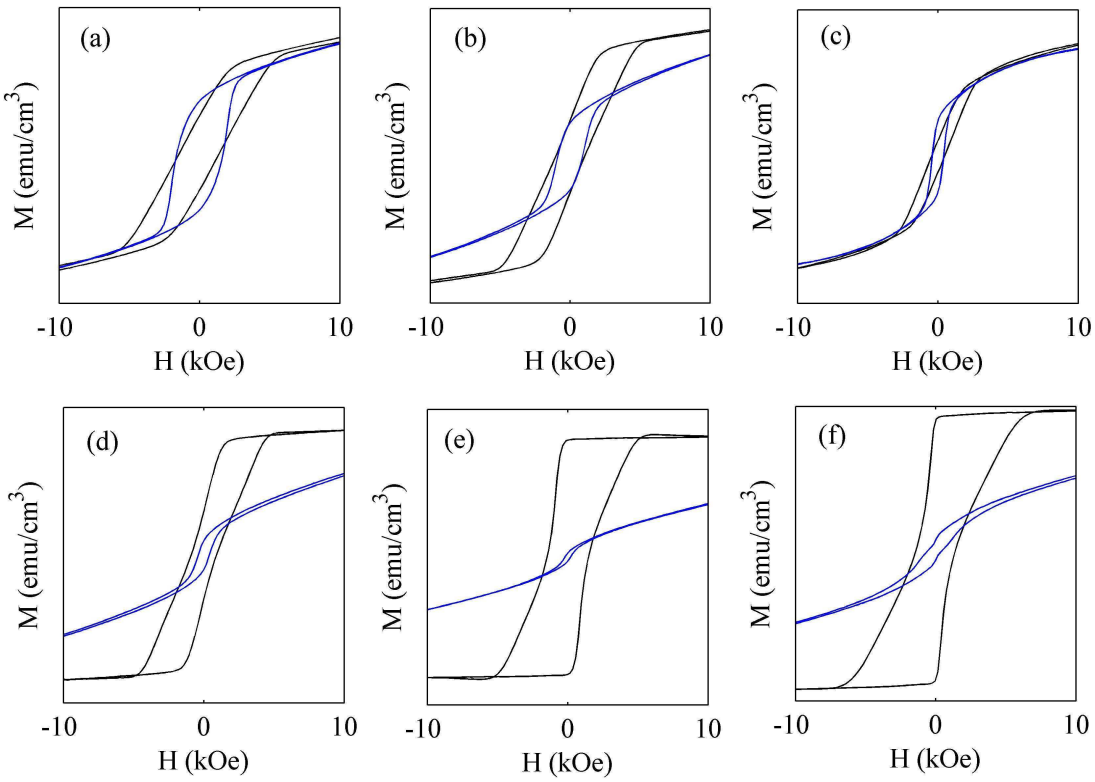

Figure 3.14 – Parallel (blue line) and perpendicular (black line) hysteresis loops performed with AGFM for FePt films, 30 nm thick, grown on a Pt underlayer deposited onto MgO monocrystalline substrates. (a) $Fe_{52}Pt_{48}$/Pt(2nm); (b) $Fe_{52}Pt_{48}$/Pt(10nm); (c) $Fe_{52}Pt_{48}$/Pt(100nm); (d) $Fe_{52}Pt_{48}$/Pt(50nm); (e) $Fe_{55}Pt_{45}$/Pt(50nm) and (f) $Fe_{58}Pt_{42}$/Pt(50nm)

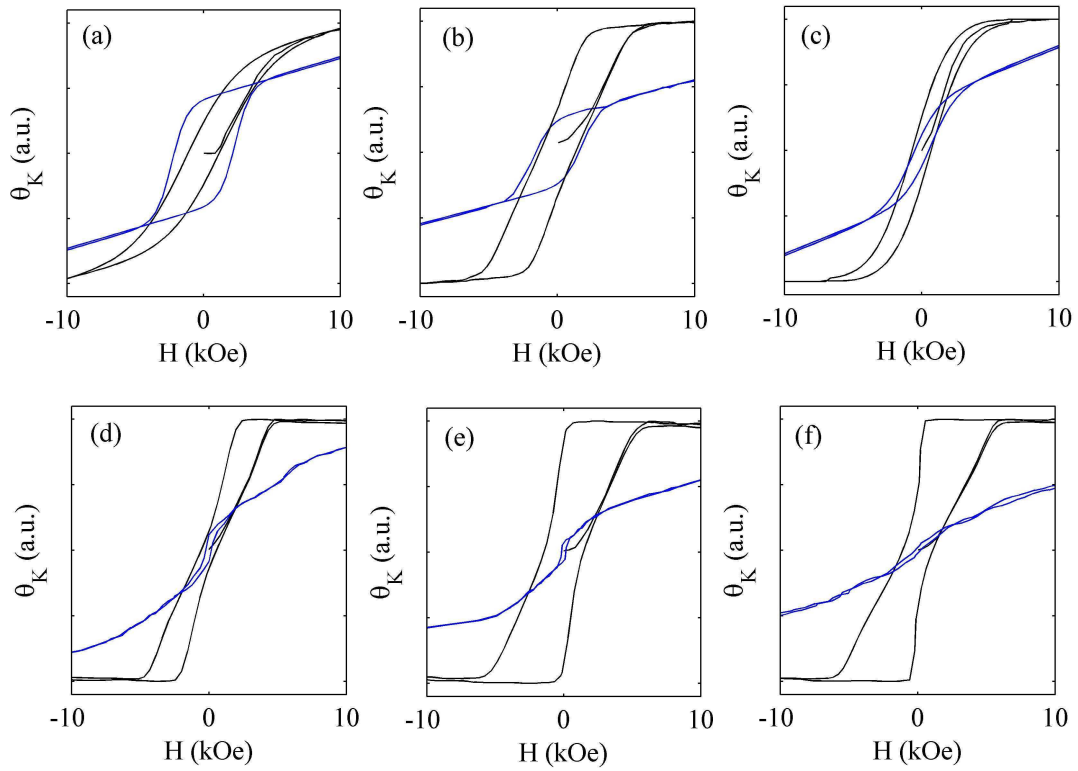

Figure 3.15 – Parallel (blue line) and perpendicular (black line) hysteresis loops performed with MOKE for FePt films, 30 nm thick, grown on a Pt underlayer deposited onto MgO monocrystalline substrates. (a) $Fe_{52}Pt_{48}$/Pt(2nm); (b) $Fe_{52}Pt_{48}$/Pt(10nm); (c) $Fe_{52}Pt_{48}$/Pt(100nm); (d) $Fe_{52}Pt_{48}$/Pt(50nm); (e) $Fe_{55}Pt_{45}$/Pt(50nm) and (f) $Fe_{58}Pt_{42}$/Pt(50nm)

A few differences can be observed in the loops reported in Figs. 3.14(c) and 3.15(c). These measurements concern the sample of $Fe_{52}Pt_{48}$ grown on a very thick Pt underlayer (100 nm). It is known that in AGFM measurements a strong contribution arises from both the diamagnetic substrate and the paramagnetic underlayer. Since the interest only concerns the magnetic behaviour of the FePt thin films, the correction of the magnetic measurements from these unwanted contributions becomes crucial. Indeed, the difference between AGFM and MOKE measurements can be attributed to the presence of these contributions in the AGFM measurements. In effect, the high thickness of the underlayer, much higher than the FePt film thickness, makes very difficult to rightly correct the loops from the underlayer contributions. On the contrary the MOKE signal arises only from the FePt film, since the penetration depth of the light can be estimated of the order of 40 nm. Therefore no data correction is necessary.

The values of the coercive fields evaluated from both AGFM and MOKE measurements are shown in Figs. 3.16(a) and 3.16(b) with respect to the Fe atomic concentration and the underlayer thickness respectively.

The difference in the measured coercivity is a combination of two effects: (i) the different field sweep rates used during the two types of measurements and (ii) the little change of film

composition near the surface. In effect while AGFM measurements are practically unaffected by surface contributions, MOKE measurements are strongly influenced from surface layers.

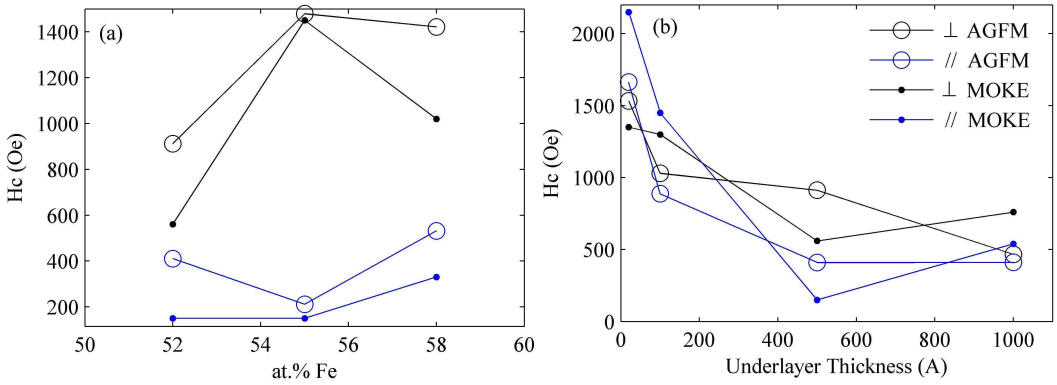

Figure 3.16 – Coercive field behaviours with respect to (a) the Fe atomic concentration and (b) the Pt underlayer thickness as evaluated from MOKE and AGFM measurements.

The sweep rate dependence of H_c is a well known phenomenon which arises because of the time dependence of the coercivity. The time-dependence phenomenon has its root in the thermal agitation of the magnetic moments of individual particles over local energy barrier provided by the magnetic anisotropy. The relationship between the time t for the magnetization to decay to zero and the applied field H is given by:

$$t = t_0 \exp\left(-\alpha \delta H\right) \tag{3.16}$$

where t_0 is the time corresponding to some field H_0 and $\delta H = H - H_0$.

The relationship between the time for the magnetization to decay to zero and the field sweep rate for a continuously measured hysteresis loop determines the relation:

$$t_{eff} = \frac{1}{R\alpha} \tag{3.17}$$

where t_{eff} represents the effective time which gives the same coercive force in a stepped field process as measured by the continuous process at a rate R (the field sweep rate). α is a constant dependent on the material that is defined as:

$$\alpha = \frac{\left(1 - h_c\right)\mu}{k_B T} \tag{3.18}$$

where h_c is the reduced coercivity, μ is the magnetic moment of the particles, T the temperature and k_B is the Boltzmann constant[36].

An increase of the coercive field values evaluated from MOKE measurements occurs if the sweep rate is greater than that used in AGFM measurements, while it is lower if the field sweep rate is lower.

For the samples grown on Pt underlayers of different thickness, the difference in the coercive field values becomes much more significant [Fig. 3.16(b)]. This can be attributed, again, to the correction of the AGFM data from the Pt and substrate contributions.

From the comparison of the hysteresis loops reported in Figs. 3.14(d) and 3.14(f) and those in Figs. 3.15(d) and 3.15(f) respectively, it is possible to deduce that MOKE measurements are more influenced from demagnetizing field effects respect to the AGFM measurements. A possible explanation can be the presence of the above mentioned surface layer having a different composition respect to inner parts of the FePt thin films. In particular the increase of the demagnetizing field strength suggests that near the surface an excess of Fe is present giving rise to a Fe-rich FePt compound.

Summarizing we have optimized the MOKE set-up reaching performances well comparable to those of an AGFM magnetometer. Also satisfactory is the calibration of the Kerr rotation angle that allows to estimate the direction and strength of the anisotropy, giving results practically equal to those obtained with AGFM. Moreover in many cases the magneto-optical signal is more reliable than the magnetic one, since the MOKE measurements are not influenced from the contributions due to underlayers and substrates and therefore no data correction must be performed.

Finally the use of both MOKE and AGFM magnetometer can be useful for the study of surface and volume contributions, analysis very important in particular in the case of exchange-spring and exchange-bias structures grown in the form of multilayers.

3.6 45° Light Incident Angle MOKE Magnetometer and Magneto-Ellipsometer

The electromagnet manufactured by the Walker Scientific Inc. and used in the MOKE apparatus allows to perform measurements in longitudinal geometry only with the light incident at very small angles (15°). Considering that the Kerr rotation in longitudinal geometry is directly proportional to the incident angle of the light, the measured signal is very small. This makes very difficult the direct comparison of perpendicular and parallel measurements and induces a lower (S/N) ratio. It is to be noted that when the incident angle is close to the normal incidence, second order effects become significant and the recorded signal loses its direct proportionality with the magnetization.

Moreover, since the electromagnet is controlled by an unipolar power supply, a few problems arise during low field measurements. These analyses are indispensable for the characterization of soft ferromagnetic samples, such as films of Fe, Co, FeCo, FeNi, etc. On these samples, the Kerr rotation is very small and a distortion in low field measurements can be observed around the zero value of the applied field. This distortion is only due to the inversion of the current polarity.

Taking into account these facts, we have decided to develop a second MOKE apparatus dedicated to low field measurements. The main requirements are the relatively small sizes and the possibility to have angles of light incidence and reflection of about 45°. Around this value, polar and longitudinal signals become of the same magnitude allowing a direct comparison of the acquired data.

This apparatus will be also used for the development of a new laboratory facility for magneto-ellipsometric measurements. These analyses will allow both the evaluation of the film thickness and the complete magneto-optical characterization of the materials, including the index of refraction and the optic and magneto-optic *Q* constants[37-38].

3.6.1 Electromagnet

The electromagnet is built with five parts all made of soft iron: the base-plate, two arms and two polar pieces.

The base-plate has two pass-holes for screws with rectangular shape for displacement of the arms for easy air-gap adjustment. The air-gap can be enlarged as far as 25 mm. The arms have two screw-holes in the bases for base-plate and polar-pieces hold. Around these arms the coils are directly wrapped. These are made with 500 turn of 1 mm diameter copper wire each, insulated by Kapton coating and connected in series. The polar pieces have a conical shape from 30 to 20 mm, this shape allows to enhance the magnetic field in spite of a small reduction of the uniform field region.

The approach followed for the electromagnet design is very easy, practical and does not consider the dispersed flux near the air gap.

If *w* is the width of the air-gap and *l* the mean perimeter of the soft iron having the same area along the whole magnetic circuit, *N* the number of turns, *I* the current in Amperes, the magnetic field *B* in Oe can be expressed as:

$$B = \frac{NI}{0.796 \cdot \left[w + \frac{l}{\mu} \right]} \tag{3.19}$$

where μ is the iron permeability that varies with the flux *B* and thus it can be evaluated from (*B*-*H*) curves of the iron. The air permeability is equal to 1. For simplicity the field in the air-gap was assumed to be equal to that in the iron core.

The magnet field response curves measured using a Gauss probe with an air-gap of 25 and 10 mm, show no saturation of the core or hysteresis loops (no remanence of the pole-pieces) for current up to 8 A.

3.6.2 Optical and Electronic Components

The electromagnet power supply is a Kepco Bipolar Operational Power Supply/Amplifier 20/20, providing positive and negative voltages and currents up to ± 20 V and ± 20 A respectively. The power supply is used in constant current mode and controlled through a PC NIDAQ card.

The optical components and set-up are very similar to those of the principal MOKE apparatus. The incident light, either *p*- or *s*-polarized, is provided by an intensity stabilized linearly polarized He-Ne laser (5 mW, 633 nm). After reflection on the sample the laser beam is modulated and measured through a Si photodiode.

Respect to the principal MOKE apparatus, the main differences are

- the possibility to adjust the light incident and reflection angles from 0° to 45° with respect to the normal to the sample plane;
- the possibility to analyze the in-plane anisotropy by applying the field along different crystallographic orientations. The study of the angular dependence of the coercive field allows a better comprehension of the magnetization reversal mechanism;
- values of the magnetic field of about 2.5 kOe allowing to perform only low-field measurements;
- the lower sensitivity in polar geometry. In the principal MOKE apparatus, the two polar pieces of the Walker Scientific electromagnet have a pass-hole allowing the light to impinge the sample normally during polar MOKE measurements. In effect, contrary to the longitudinal case, in polar geometry the Kerr rotation is a maximum for normal incidence of the light.

3.6.3 Early Tests

The early tests have been carried out with two polycrystalline samples of Co and $SmCo_5$ e-beam evaporated at room temperature on naturally oxidized (100)-Si and glass substrates

respectively. The thicknesses, controlled in-situ through a quartz microbalance, were 50 and 30 nm respectively. Both samples have been capped with a very thin Au layer, 5 nm thick.
The hysteresis loops recorded in longitudinal geometry are reported in Fig. 3.17.

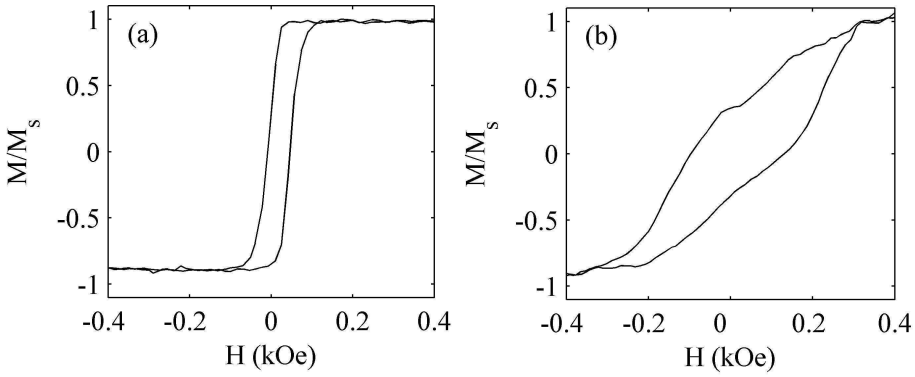

Figure 3.17 – Hysteresis loops measured in longitudinal geometry for (a) Co and (b) $SmCo_5$ samples.

No electronic drift correction or smoothing procedure has been performed on the data, an indication of the good stability of the MOKE apparatus and of the optimal (S/N) ratio. Both hysteresis loops are very difficult to measure with the principal MOKE magnetometer because of the very low Kerr signal and the appearance of strong second order effects due to the small angle of incidence of the light.

Thanks to the good resolution and performances of this apparatus, measurements of the in-plane magnetic texture become possible. The analyses have been performed for the $SmCo_5$ sample, by applying the field at different orientations with respect to the in-plane crystallographic directions (Fig. 3.18). Also in this case no correction of electronic drift or data smoothing have been performed. The results are quite satisfactory.

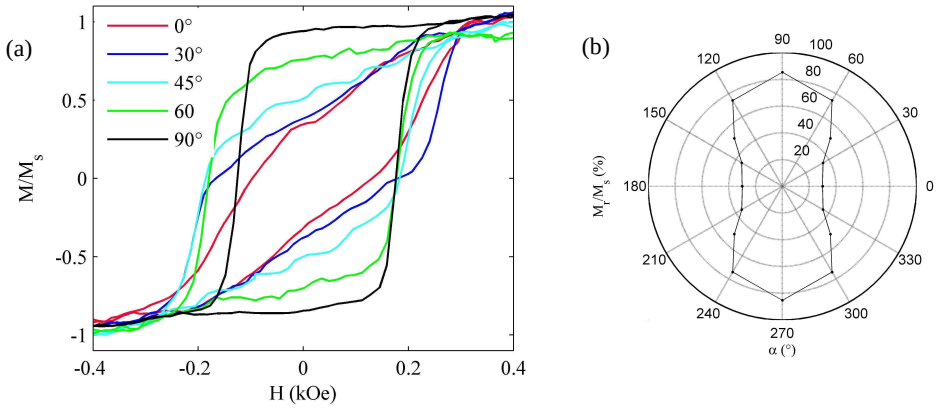

Figure 3.18 – (a) Hysteresis loops measured in longitudinal geometry with the field applied along different directions in the film plane for $SmCo_5$ sample and (b) the corresponding polar plot showing the angular dependence of the normalized remanent magnetization.

Due to the presence of an uniaxial anisotropy, the shape of the hysteresis loop is highly squared when the field is applied parallel to the easy axis. On the contrary, applying the field perpendicular to the easy axis, the loop tends to become almost a straight line. The polar plot of the remanence ratio as a function of the angle α between the in-plane applied field direction and the easy axis [Fig. 3.18(b)] shows a departure from the cosine-like behaviour typical of samples with simple in-plane anisotropy. The non-zero value of the remanence for $\alpha \approx 0°$ suggests the presence of a small out of plane component of the magnetization.

The angular dependence of the in-plane coercive field reported in Fig. 3.19, indicates that the magnetization reversal mechanism approaches that of the Stoner-Wohlfarth model of coherent rotation. The differences from the Stoner-Wohlfarth behaviour can be ascribed to the presence of contributions due to incoherent nucleation curling mode.

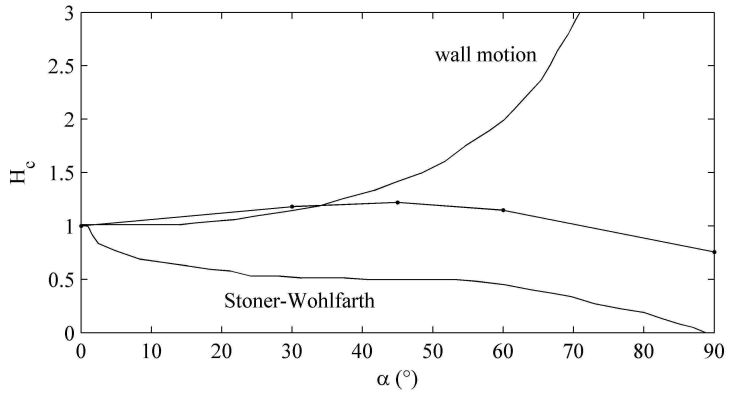

Figure 3.19 – Angular dependence of coercivity of $SmCo_5$ film. For α = 0° the applied field is parallel to the in-plane easy magnetization axis. The behaviours typical of domain wall motion mechanism and of the Stoner-Wohlfarth model are also shown.

The obtained results on Co and $SmCo_5$ samples indicate that the new MOKE apparatus allows to perform low-field measurements with a high (S/N) ratio, high resolution and reproducibility.

Chapter 4

$L1_0$-Ordered Systems

Binary alloys such as FePt, CoPt, FePd, and MnAl, around the equiatomic composition, are characterized by a high temperature phase transformation that induces a tetragonal distortion of the crystallographic lattice. The formation of the tetragonal $L1_0$ phase occurs through its nucleation and growth process inside the disordered phase. The ordering takes place simultaneously with a first-order cubic-tetragonal transformation, occurring through the shortening of the *c*-axes. This contraction is due to the formation of a structure constituted by alternate layers of the alloy elements. The ordering gives rise to the appearance of a strong magnetocrystalline anisotropy along the contracted axis (*c*-axis).

Table II summarizes the main intrinsic properties of the more common $L1_0$-ordered systems.

Table II. Main intrinsic properties of the $L1_0$-ordered systems[39].

	K_u (10^7 erg/cm^3)	M_s (emu/cm^3)	H_k (kOe)	T_c (K)
FePd	1.8	1100	33	760
FePt	6.6 - 10	1140	116	750
CoPt	4.9	800	123	840
MnAl	1.7	560	69	650

K_u is the first order magnetocrystalline anisotropy; M_s the saturation magnetization; H_k the anisotropy field and T_c the Curie temperature

In bulk systems the $L1_0$ phase is kinetically suppressed, and thermal annealing at temperatures higher than 1000 K is required to transform the material from the disordered to the ordered structure. However in thin films, the transformation temperature is significantly reduced due to the enhanced diffusion during the film growth on heated substrates.

Moreover in the form of thin films, these alloys can be grown epitaxially with the *c*-axis oriented along the perpendicular to the film plane. This oriented growth allows to obtain systems showing a strong perpendicular anisotropy.

This characteristic makes the $L1_0$-ordered compounds very interesting from the technological point of view since they are promising candidates for the development of ultra-high density recording media, MEMS (microelectromechanical systems) and permanent magnets.

The interest is in particular due to the fact that it is possible to tune the magnetic properties through the microstructure and morphology of the films whose characteristics are mainly determined by the deposition technique and the growing parameters (temperature and growth rate). The type of growing technique and the parameters set during the deposition determines the growth mode (layer by layer or 3D), the degree of epitaxy and chemical order of the samples.

Among the growing parameters the temperature is the most important, strongly influencing the phase transformation and the tetragonal distortion of the lattice. The annealing processes can be carried out either during or after the growth. In this last case the degree of chemical order is also influenced by the exposure time of the thermal treatments.

When the substrate is heated during the deposition, the process is governed by the surface adatom mobility and the phase transformation proceeds via a continuous-type reaction[40-41]. On the contrary films deposited at room temperature and subsequently annealed order through volume diffusion and the ordering proceeds via a discontinuous/first order reaction[42].

In the thinner films the transformation process is limited by the sample thickness and high temperatures and long annealing times are required for the ordering to proceed. In thicker films, the energy barrier to nucleation and growth of a new phase is lower and indeed lower temperatures are required for the ordering.

At the nanometric scale, another thermodynamic variable has to be considered: the particle size *D* which directly affects the order-disorder transition temperature. Computer simulations predict that the ordering would not take place if the particle size is below a critical value at which the more stable state is the disordered one.

Parameters such as the degree of chemical order and the tetragonal distortion strongly determine the strength of the magnetocrystalline anisotropy. The degree of chemical order[43] can be quantized through the *order parameter S* defined as:

$$S = \frac{r_{Pt} - x_{Pt}}{y_{Fe}} = \frac{r_{Fe} - x_{Fe}}{y_{Pt}} \tag{4.1}$$

where x is the atomic fraction of one atomic species in the sample, r the fraction of sites occupied by the right atomic species, and y the fraction of the second atomic specie.

The values of S range from 0 (completely disordered phase) to 1 (completely ordered phase). However the maximum value of S depends on the stoichiometry of the considered alloy: $S_{\max} = 1 - 2x$ where x is the deviation of the atomic composition from the equiatomic one. Generally real systems are not completely homogeneous and more than one phase can be present. In this case only an average value of the order parameter can be evaluated: $S_{av} = f_0 \times S_{ord}$ where f_0 is the volume fraction of the completely ordered phase.

The ordered volume fraction can be described by the standard Johnson-Mehl-Avrami equation:

$$f_0 = 1 - \exp\left(-kt^n\right) \tag{4.2}$$

where t is the time, k is a constant and n is the Avrami exponent. Both k and n depend on the nucleation and diffusion rates, which, in turn, depend on the activation energy and temperature through the Arrhenius equation, growth mechanism and spatial dimensionality of the growing region.

The degree of chemical order can be directly related to the tetragonal distortion of the lattice cell:

$$S^2 = \frac{1 - (c/a)}{1 - (c/a)_{eq}} \tag{4.3}$$

where (c/a) and $(c/a)_{eq}$ are respectively the lattice parameter ratios of the considered specimen and the perfectly ordered equiatomic alloy[44].

This order parameter can be derived directly from the ratio of the integrated intensity of the fundamental and superstructure reflections in the X-ray diffraction pattern[45]:

$$\frac{E(002)}{E(001)} \approx \frac{\left(FF^*\right)_{(002)} (LP)_{(002)}}{\left(FF^*\right)_{(001)} (LP)_{(001)}} \tag{4.4}$$

where E(hkl), F(hkl) and F^*(hkl) are the integrated intensity, the structure factor and its complex conjugate for the (hkl) diffraction peak, L and P are the Lorentz and the polarization factors.

For the $L1_0$ structure of a binary alloy AB:

$$\begin{aligned} \left(FF^*\right)_{(002)} &= 16\left[\left(x_A f_A e^{-M_A} + x_B f_B e^{-M_B}\right)^2 + \left(x_A \Delta_A e^{-M_A} + x_B \Delta_B e^{-M_B}\right)^2\right] \\ \left(FF^*\right)_{(001)} &= 4S^2\left[\left(f_B e^{-M_B} - f_A e^{-M_A}\right)^2 + \left(\Delta_B e^{-M_B} - \Delta_A e^{-M_A}\right)^2\right] \end{aligned} \tag{4.5}$$

where e^{-M} is the Debye-Waller correction and *f* and Δ are the real and imaginary parts of the atomic factors respectively. The increase of the order parameter and therefore of the tetragonality of the unit cell induces an increase of the anisotropy and coercivity of the alloy.

Under normal growth conditions, the films often possess (111)-preferred or random orientations. The crystallographic orientation of the *c*-axis along the perpendicular to the film plane can be induced and tuned through the choice of suitable substrates and buffer-layers, the optimization of the film thickness and composition, the growth rate and the annealing temperature.

In effect the growing parameters influence thermodynamic and kinetic factors (such as the relative growth rate of the grains and their successive coalescence), in this way, changing the surface and interface energies between substrate and film[46]:

$$E_a \cong x\left[\gamma_f(\chi,\alpha)+\gamma_{f/s}(\chi,\alpha)\right]+(1-x)\gamma_s \tag{4.6}$$

where *x* is the surface regions of the substrate covered by the film, γ_f and γ_s are the surface energies of the film and the substrate respectively and $\gamma_{f/s}$ is the film/substrate interface energy. χ and α are the azimuthal rotation and in-plane angles indicating the dependence of the surface and interface energies on the growth orientation. The minima of this energy determine the preferred directions of the grain growth, among these the more stable minimum is determined by kinetic factors. It is to be noted that the minima of the interface energy are mainly due to the stress relaxation through elongation and contraction of the unit cells and the formation of dislocations at the film/substrate interface.

As mentioned above, the growth of films at low temperature and high deposition rates induces a preferred orientation of the grains along the (111) direction. This direction represents a stable minimum of the surface energy and a local minimum of the interface energy. Indeed the phenomenon of the island coalescence can be helpful for the development of a (111) preferred growth orientation. In effect, the contact among neighbouring islands randomly oriented gives rise to grain boundaries that change to minimize the energies. The grains oriented along energetically favoured directions increase their sizes at expense of the grains having other orientations, in this way lowering the surface roughness of the film.

The (100) direction represents an absolute minimum of the interface energy and is favoured by high temperatures and low deposition rates.

Chapter 5

FePt Films

The phase diagram of the bulk Fe-Pt alloy is reported in Fig. 5.1. Iron and platinum are completely miscible in the solid state, and they can constitute an alloy in a large range of compositions. Three stable superstructures are present, the Fe_3Pt, the FePt and the $FePt_3$.

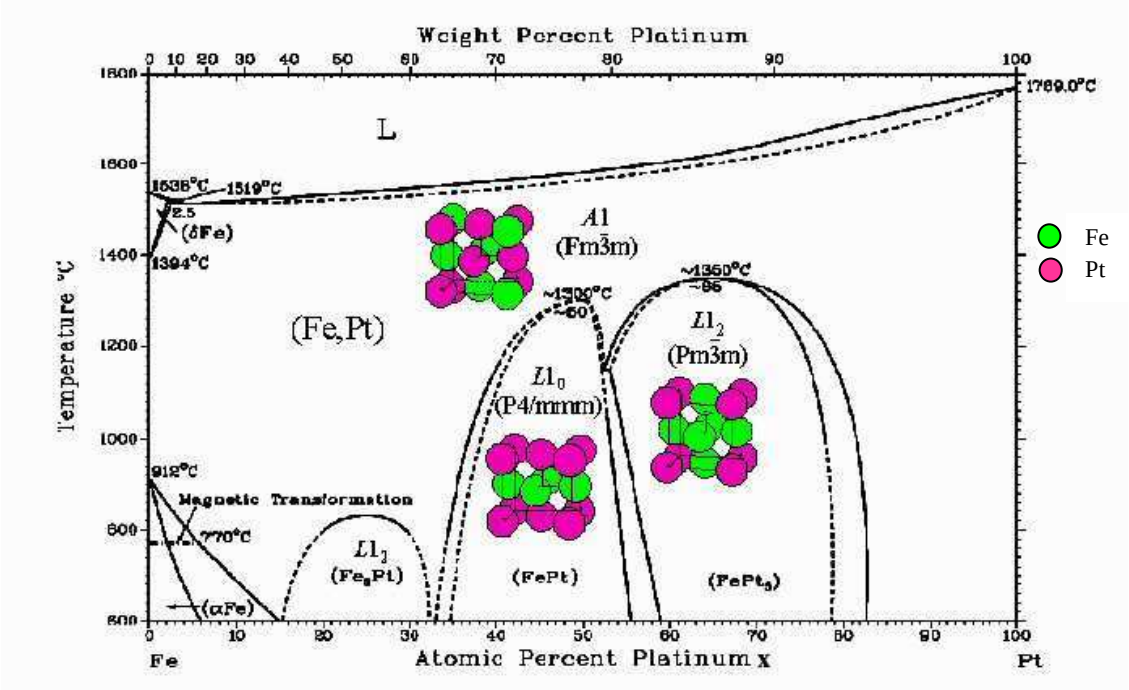

Figure 5.1 – Phase diagram of the Fe-Pt alloy.

In the disordered form (called γ or *A*1 phase), the Fe-Pt alloy shows a face centred cubic (fcc) structure with iron and platinum atoms randomly oriented in the unit cell. In this phase the alloy displays very soft magnetic properties and the mean magnetic moment linearly increases with the iron concentration (Fig. 5.2). At high temperatures and around the equiatomic composition (35 ÷ 55 at.% Pt), the alloy shows a structural transformation[47-49] with the

establishing of the $L1_0$-ordered phase (Fig. 5.1) and the development of a strong magnetocrystalline anisotropy ($K_{eff} \sim 7 \cdot 10^7$ erg/cm^3) oriented along the contracted *c*-axis.

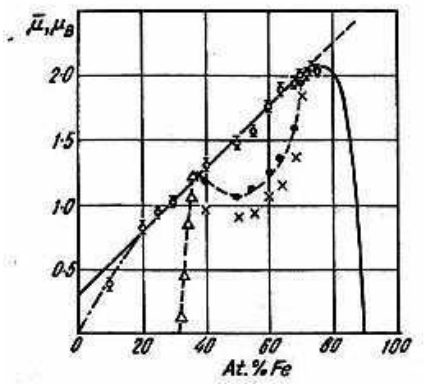

Figure 5.2 – Concentration dependence of the Fe-Pt mean magnetic moment in the disordered phase (**—** theory, ○ experimental) and for the ordered one: (Δ) Bacon and Crangle results; calculated values (×) from magnetization measurements in applied field of 12 kOe and (●) from the *law of the approach to saturation*[50].

For Fe-rich stoichiometry, the Fe_3Pt ordered phase is characterized by a cubic lattice, with soft ferromagnetic properties. This alloy shows the Invar effect and undergoes a martensitic transformation for temperature lower than the room temperature. This martensitic ordered phase is characterized by a bct structure. For the Pt-rich stoichiometry, the $L1_2$-ordered $FePt_3$ phase is paramagnetic at room temperature and can exhibit two types of antiferromagnetic order. This property is linked to the indirect exchange-coupling of the Fe moments through the non-magnetic Pt atoms (Fig. 5.3).

Around the equiatomic composition, the exchange-interaction is ferromagnetic between nearest and antiferromagnetic between next nearest Fe-Fe neighbours, the ferromagnetic interaction being greater in absolute value than the antiferromagnetic one[50].

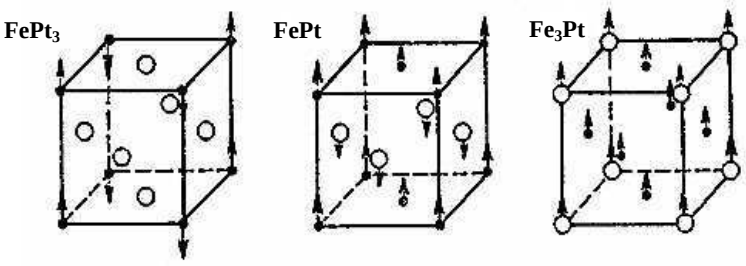

Figure 5.3 – Representation of the magnetic moments of the (●) Fe and (○) Pt atoms, the arrows indicate the spin direction.

In the ordered states, the linear dependence of the mean magnetic moment on the Fe concentration is completely lost (Fig. 5.2). In effect, the moment does not appear until 31 at.% Fe after which it abruptly increases reaching the curve corresponding to the disordered state. Then, around the equiatomic composition, a minimum of the moment value occurs. Above 50

at.% Fe the moment increases and around 70 at.% Fe its behaviour coincides with that of the disordered phase. This trend is due to the Pt atom polarization caused by the exchange-enhanced paramagnetism that is a well-know feature of the Pt metal.

5.1 $L1_0$-Ordered FePt Thin Films

In the form of thin film, the FePt phase transformation takes place to lower temperature values (300 ÷ 700 °C) and can be favoured by post-annealing treatments[51]. The structural transformation induces an increase of the *a*-axes, and a more evident contraction of the *c*-axes strongly influencing the strength of the anisotropy (Fig. 5.4).

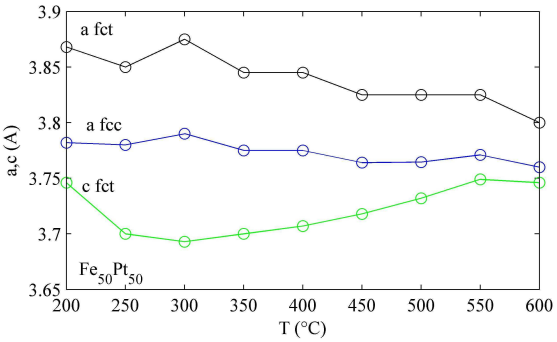

Figure 5.4 – Behaviour of the lattice constants with respect to the growing temperature for equiatomic FePt films in the ordered and disordered phase[41].

A strong perpendicular anisotropy develops by epitaxially growing the films with the *c*-axis oriented along the surface normal. This epitaxial growth can be favoured by the choice of suitable substrates, seed- and underlayer.

The most useful type of substrate is a MgO (100) single-crystal one. This substrate has a cubic lattice (a = 4.21 Å), is stable at very high temperature and is immiscible with the alloy constituents[52]. The lattice mismatch (~ 11%) induces a strain that favours the tetragonal distortion of the FePt unit cell by slightly enlarging its base and shrinking the *c*-axis. In this way, the energy barrier for the phase transition can be lowered and the temperature at which the ordering proceeds decreases, reaching value of 300°C[53,54].

The extent of the substrate-film mismatch drives the epitaxial direction of the film; this implies that by varying the lattice spacing of the substrate it is possible to tune the degree of epitaxy of FePt and the presence of *c*-axis orientation variants. With this aim it has been exploited the possibility to introduce a suitable underlayer. Among the different elements, the Pt is the most promising, because of its cubic structure and its lattice parameter of about 3.92 Å.

The epitaxial growth of the Pt underlayer on MgO is characterized by a "cube-on-cube" orientational relationship, i.e. a (100) growth. This can be obtain by the optimization of the Pt layer thickness[55-58], high temperature growth (~ 700°C)[55] and low deposition rate (~ 1 Å/sec).

The introduction of a thin seed-layer of Fe between the Pt layer and the substrate favours the complete disappearance of Pt grains oriented along the (111) direction at lower temperature than 700°C[58]. The deposition of Fe at room temperature (RT) on MgO substrates[52,59] induces an island growth. By increasing the film thickness, these islands coalesce giving rise to a tetragonal distortion of the Fe cubic lattice. The high temperature annealing deletes this distortion, causing the reappearance of an island structure.

As for the Fe_xPt_{100-x} alloy, its magnetic properties are strongly influenced by the microstructure, such as the crystallographic orientation, the chemical order and the epitaxial degree. These aspects are linked to the morphology and to the lattice mismatch between different layers. The optimization of the growing parameters, i.e. deposition rate, substrate temperature[41,45,51,60], underlayer thickness[40,61-62], the thickness[63-64] and stoichiometry of the FePt film[65-66] and the relative Fe/Pt layer thickness[67], allows to obtain the best hard magnetic properties in the alloy.

The contraction of the unit cell is strongly correlated to the working pressure[68], to the growth temperature[60] and to the stoichiometry of the film[66,69]. In particular, the growing temperature determines the surface mobility of the atoms, and its increase favours an enhancement of surface diffusion and a better intermixing between the Fe and Pt layers, increasing the chemical order and the surface roughness[41] of the film.

The chemical order can also be increased at moderate temperature by the growth of the film in the form of multilayer[44]. This is particularly true for Fe/Pt thickness ratio equal to 1, in this case the multilayer structure completely disappears and contemporary the ordering takes place for temperature of only 300°C. In effect, for equal thickness of the single-elemental layers a minimum of the activation energy for the ordering occurs.

The increase of the chemical order can also be favoured by the use of Fe-rich stoichiometry. This is due to the lower lattice parameter of the Fe atoms respect to that of the Pt ones, favouring an increase of the (c/a) ratio.

5.2 Sputtered FePt Thin Films

In this section, FePt films grown by rf sputtering, technique located at the *IMEM-CNR* of Parma, are investigated through X-ray diffraction (XRD), conversion electron Mössbauer

spectroscopy (CEMS), magneto-optical Kerr effect (MOKE) and magnetic force microscopy (MFM). The effects on the phase transformation of the annealing processes at high temperature performed during or after the growth have been analyzed. Moreover, the evolution of the magnetic properties of the FePt films has been studied in dependence on the film thickness and the introduction of a Pt underlayer.

$Fe_{52}Pt_{48}$ films 15 and 20 nm thick were deposited onto MgO (100) single crystal substrates by alternating ~ 0.1 nm thick layers of Fe and Pt, at room temperature [*RT-FePt(20)*] and at 550°C. The films grown at high temperature were deposited directly on the MgO substrates [*FePt(20)*] or onto a previously deposited buffer-layer constituted by a 20 nm thick Pt layer grown on a thin seed-layer of Fe, 1 nm thick [*Pt/FePt(15)* and *Pt/FePt(20)*]. The growth rates for Fe and Pt were 12.7 and 11.7 Å/min, respectively.

The RT-FePt(20) films were grown using the ^{57}Fe Mössbauer isotope and, subsequently, post-annealed in vacuum at 550°C and 850°C for 2h. On the contrary, the films grown at 550°C were deposited using natural iron.

It is to be noted that since normal sputtering targets are constituted by natural iron, for the growth of the RT-FePt(20) films, the Fe target was covered by a thick layer (200 nm) of Fe highly enriched with ^{57}Fe Mössbauer isotope. This layer has been grown at room temperature using the UHV e-beam evaporation technique (Surface Laboratory). Due to the high sizes (5 × 10 cm) and weight of the sputtering target, the assembly system of the evaporating chamber has been modified to assure the uniformity of the covering layer.

The X-ray diffraction (XRD) patterns were recorded at the University of Bologna, using a computer-controlled goniometer and Cu(K_α) radiation. Conversion Electron Mössbauer Spectroscopy (CEMS) measurements were carried out in high vacuum using a 55 mCi ^{57}Co(Rh) source. The γ-rays incident angle was 20°. The spectra were fitted using a least squares minimization routine with a combination of linear and nonlinear regressions. The isomer shifts, *IS*, are referred to α-Fe. The magnetic properties of the samples were measured using the Magneto-Optical Kerr Effect (MOKE) magnetometer, with *s*-polarized 633 nm He-Ne laser light. The domain patterns of the samples were recorded using a UHV Magnetic Force Microscopy (MFM) in tapping mode. In order to study the intergrain interactions, dc demagnetization (DCD) remanence and isothermal remanence (IRM) curves were collected. DCD remanence curves were recorded starting from a sample in the saturated state and then applying increasing negative fields. On the contrary for IRM remanence curves, the sample was initially demagnetized through successive minor loops and then subjected to increasing positive fields.

5.2.1 Effects of the Annealing Process Performed During or After the Growth

The magnetic properties of RT-FePt(20) films are typical of a soft ferromagnetic phase having a cubic symmetry (Fig. 5.5). The magnetization lies in the film plane because of the presence of a strong demagnetizing field along the normal to the film plane.

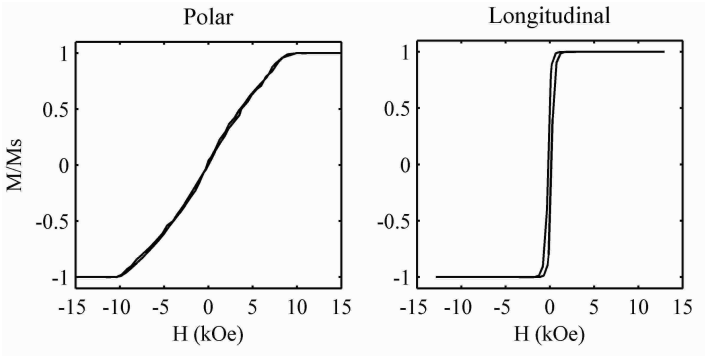

Figure 5.5 – Polar and longitudinal hysteresis loops for the RT-FePt(20).

The CEMS spectrum in Fig. 5.6 can be fitted with the superposition of three contributions whose hyperfine parameters are reported in Table III. Sextet ψ can be attributed to the *A*1-disordered FePt phase, because of the hyperfine field value (305 kOe) and the absence of a quadrupolar splitting indicating the presence of a cubic structure. On the contrary sextet τ, characterized by a lower hyperfine field and by a high quadrupolar splitting can be attributed to the $L1_0$-ordered FePt phase. The amount of this ordered phase as obtained from the area ratio in the CEMS spectrum is very low and therefore not able to appreciably affect the soft magnetic behaviour (Fig. 5.5). As for the main contribution to the spectra, sextet φ, the negligible quadrupolar splitting and the value of the hyperfine field which is in between those characteristic of the ordered and disordered phases, suggest that it can be due to an intermediate FePt phase showing a non completely ordered structure.

The analysis of the line intensity ratios of all contributions to the spectra indicates that the magnetization of the cubic phase (sextet ψ) is in-plane randomly oriented, while that of both tetragonal (sextet τ) and intermediate (sextet φ) phases are slightly tilted out of plane. This tilting is also confirmed by polar Kerr measurements (Fig. 5.5), showing that the sample can be led in the saturated state for relatively low applied fields.

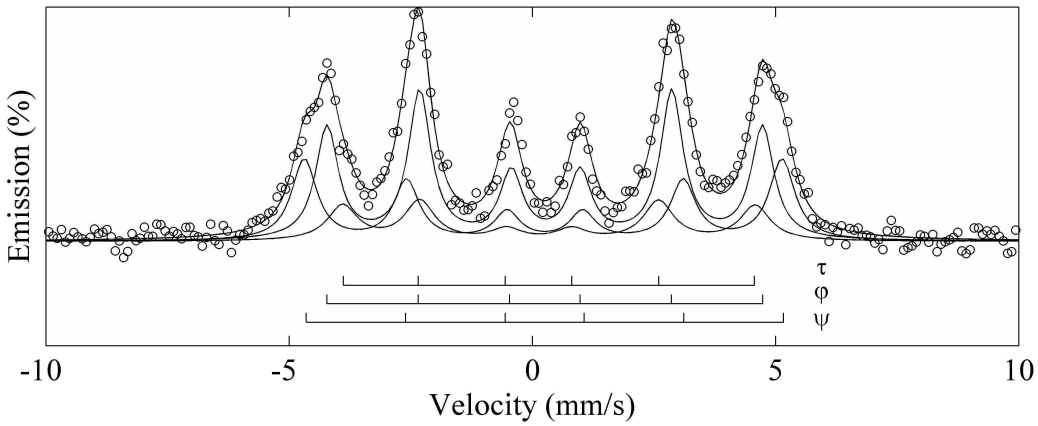

Figure 5.6 – CEMS spectrum of RT-FePt(20) film.

No relevant differences have been detected in the Mössbauer spectrum and in the magnetic measurements carried out after the post-annealing of the sample at 550°C for 2h. The presence of an intermediate (not-completely ordered) phase in the RT-FePt(20) (Fig. 5.6) that remains after the treatment at 550°C suggests that in FePt the ordering does not proceed via a simple first-order transformation. The disordered phase does not simply transforms into the ordered one but undergoes progressive modifications in the structure and local atomic environment before giving rise to the ordered $L1_0$-phase[46]. Atomic size differences, static atomic displacements and presence of short range order could influence the overall ordering rates when annealing is conducted at moderate temperatures.

The post-annealing of RT-FePt(20) at 850°C for 2h induces the phase transformation and a complete reorientation of the magnetization out of the film plane (Fig. 5.7). The polar hysteresis loop shows a decrease of the demagnetizing field and an increase of the coercivity that reaches a value of 214 Oe.

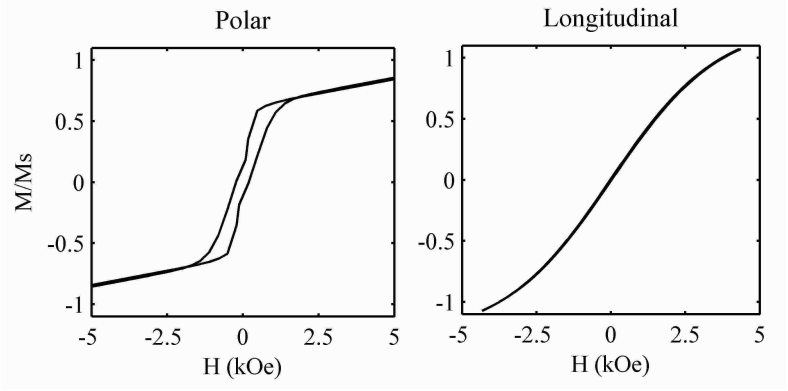

Figure 5.7 – Polar and longitudinal hysteresis loops for the RT-FePt(20) film subjected to a post-annealing process at 850°C for 2h.

The absence of coercivity and remanence in the longitudinal hysteresis loop and the difficulty to reach the saturation with the field applied perpendicular to the film plane (Fig. 5.7) suggest the presence of small particles showing a superparamagnetic behaviour.

In effect, the CEMS spectrum performed on this film is constituted by the superposition of a doublet τ_1 and a series of sextets τ_2 whose hyperfine field distribution is reported inside the Fig. 5.8. The hyperfine parameters are reported in Table III. The low value of the main peak of the hyperfine field distribution relative to the τ_2 contribution and the high quadrupolar splitting of the τ_1 doublet suggest that they can be due to the $L1_0$-ordered FePt. This phase is characterized by a distribution of particle sizes showing collapsing hyperfine magnetic fields (τ_2 contribution) up to the superparamagnetic limit (τ_1 doublet).

Table III. Hyperfine parameters of the contributions to the CEMS spectra reported in Figs. 5.6 and 5.8

	τ	**φ**	**ψ**	**τ_1**	**τ_2**
IS(mm/sec)	0.26	0.25	0.25	0.22	0.15
ΔE_Q(mm/sec)	0.29	0.04	-	0.50	-0.06
H_{hf} (kOe)	269	275	305	-	135[*)]

[*)]**Main peaks of the H_{hf} distribution**
IS: isomer shift relative to α-Fe; **ΔE_Q:** quadrupole splitting; **H_{hf}:** hyperfine field

The formation of superparamagnetic particles with a broad distribution of particle sizes occurs as a consequence of different thermal expansion coefficients between film and substrate. This difference gives rise to a strong tensile stress in the film plane that is realised through micro-cracks and the breaking of major islands into minor grains.

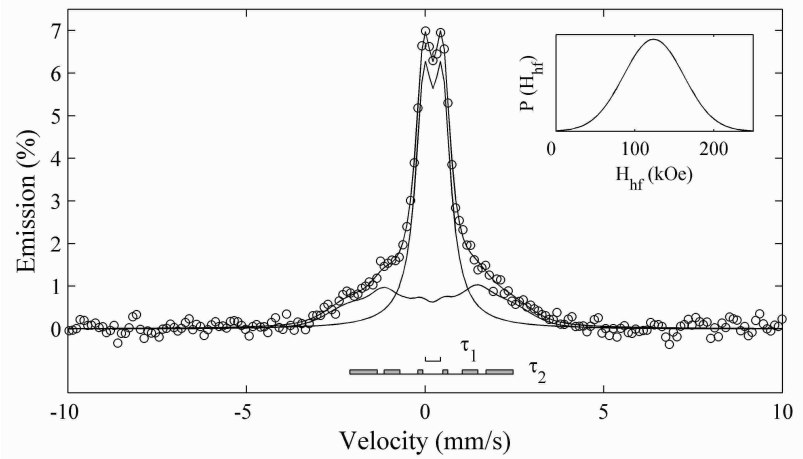

Figure 5.8 – CEMS spectrum of the RT-FePt(20) film post-annealed at 850°C for 2h.

In effect at low temperature the stress are induced by the lattice mismatch between film and substrate and they are released through the grain coalescence and the formation of an island

structure. At high temperature (> 650°C) thermal stresses overcome those due to the lattice mismatch. This type of stress can be released only by reducing the surface contact between film and substrate with the consequent disappearance of the islands and the formation of small particles.

A different situation takes place if the FePt film is grown at 550°C [FePt(20) sample]. While the XRD pattern of RT-FePt(20) [Fig. 5.9(a)] shows only the (200) reflection of the disordered cubic phase and only a broad contribution due to the (001) peak of the ordered one, the FePt(20) film [Fig. 5.9(b)] shows well defined (002) fundamental and (001) superstructure reflections typical of the $L1_0$-ordered phase. The presence of only these two reflections indicates that the film grew epitaxially with the *c*-axis oriented out of the film plane.

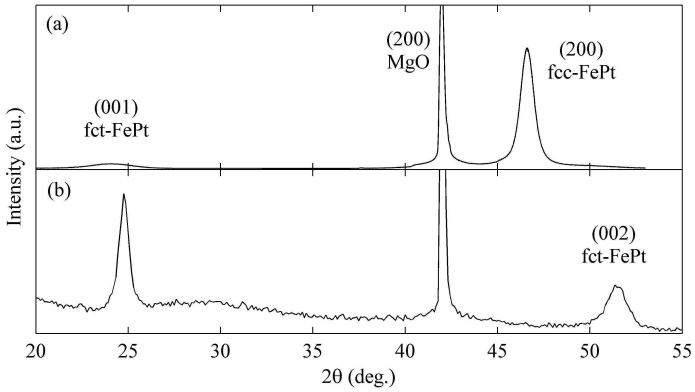

Figure 5.9 – XRD pattern of (a) RT-FePt(20) and (b) FePt(20).

The hysteresis loop measured in polar geometry (Fig. 5.10) shows the presence of a perpendicular anisotropy whose strength is not sufficient to completely overcome the demagnetizing effects. On the other hand, the loop measured in longitudinal geometry indicates that the easy axis is not perfectly oriented along the perpendicular to the film plane. This is probably due to a dispersion of the *c*-axis orientations along the (001) direction or to the presence of minor components not completely ordered favouring an in-plane orientation.

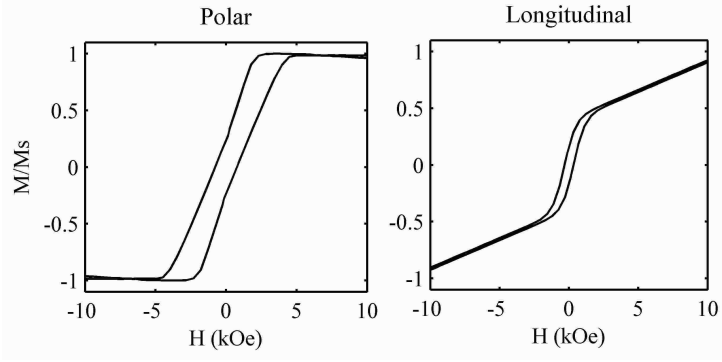

Figure 5.10 – Polar and longitudinal MOKE measurements for the FePt(20) film.

The differences found in the magnetic behaviour and phase transformation rate between high temperature grown and post-annealed FePt films are due to the fact that the $A1 \rightarrow L1_0$ phase transformation is a diffusion-driven process. The role of the temperature is to increase the kinetic factors, allowing the rearrangement of the atoms in thermodynamic regions where the stable phase is the tetragonal $L1_0$ phase and the disordered one becomes metastable. When the deposition takes place at RT, the transformation is driven by the volume diffusion and higher temperatures are required to give to the atoms the sufficient mobility for the ordering to proceed (T > 650°C). On the contrary, the growth on heated substrates allows the ordering to proceed at lower temperature thanks to a lower activation energy. In effect, in this case the process is driven by surface diffusivity that is orders of magnitude greater than the volume one[48,70-71].

5.2.2 Effects of a Pt Underlayer and of the Variation of the FePt Film Thickness

The effects of a buffer-layer on the magnetic properties of FePt films has been studied by growing the FePt(20) film onto a previously deposited Pt underlayer 20 nm thick and a Fe seed-layer 1 nm thick, Pt/FePt(20). Furthermore, the FePt film thickness has been varied from 20 nm to 15 nm, Pt/FePt(15).

In Fig. 5.11 the MOKE measurements of FePt(20), Pt/FePt(20) and Pt/FePt(15) samples are reported. Respect to the FePt(20) film [Fig. 5.11(a)], the Pt/FePt(20) sample [Fig. 5.11(b)] shows a better square-shaped loop and harder magnetic properties: the remanence ratio M_r / M_s reaches a value of 0.99 and the coercive field a value of 3.12 kOe.

The enhancement of the loop squareness suggests an increase of the anisotropy intensity due to a better epitaxial growth of the FePt film and to a lower dispersion of the *c*-axis along the perpendicular to the film plane. On the other hand, the increased hardness is due to a different microstructure of the FePt film induced by the Pt layer. In effect, the lattice mismatch between Pt and substrate is released through dislocations and defects in the Pt layer that induce an increase of defect density in the alloy. Moreover a strong tensile stress develops between Pt and FePt film whose relaxation gives rise to "twins" and anti-phase grain boundaries[62]. All these types of planar defects hinder the domain wall motion raising the coercivity of the FePt films.

The shape of the first magnetization curve [Fig. 5.11(b)] suggests that the main mechanism controlling the coercivity is the domain wall pinning. The more marked kink in the first magnetization curves of Pt/FePt(15) [Fig. 5.11(c)], suggests that a strengthening of the pinning mechanism occurs when the thickness of the FePt film is reduced from 20 to 15 nm. This strengthening gives rise to a strong increase of the coercivity. The increased hardness of the

Pt/FePt(15) film can be explain through a reduction of the grain sizes that induces an increase of grain boundaries hindering the domain wall motion[72].

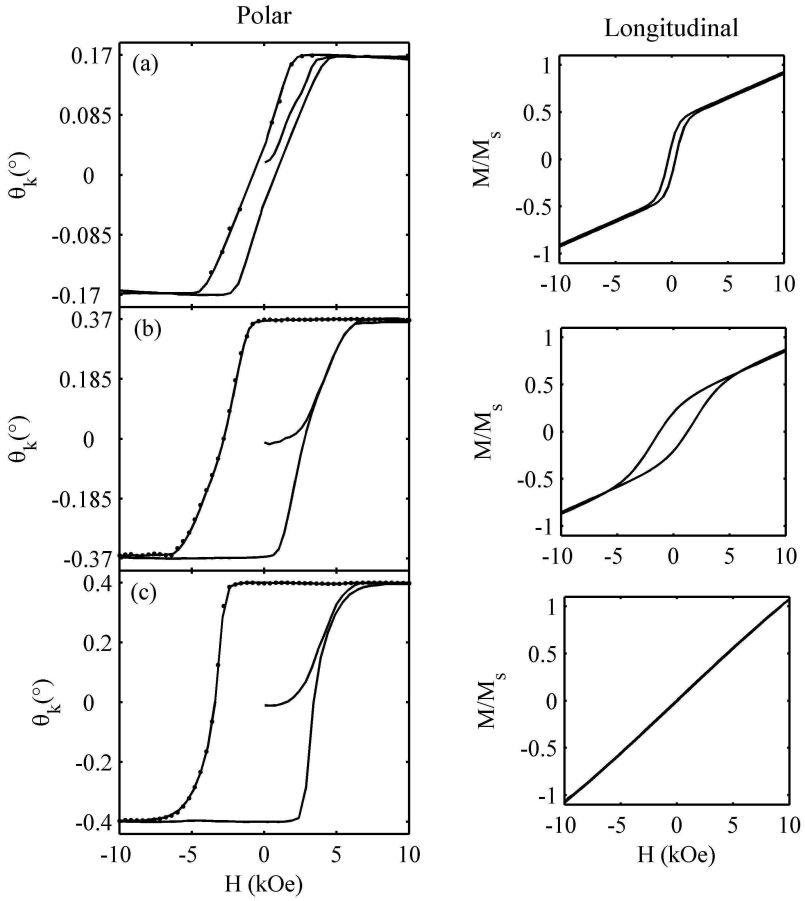

Figure 5.11 – Polar and longitudinal MOKE measurements for (a) FePt(20), (b) Pt/FePt(20) and (c) Pt/FePt(15). (—) Hysteresis loops and initial curves; (•) DCD remanence curves.

MFM image recorded for FePt(20) [Fig. 5.12(a)] shows a labyrinth-stripe domain configuration. The appearance of this magnetic pattern is due to the competition between magnetostatic and anisotropy energies[9].

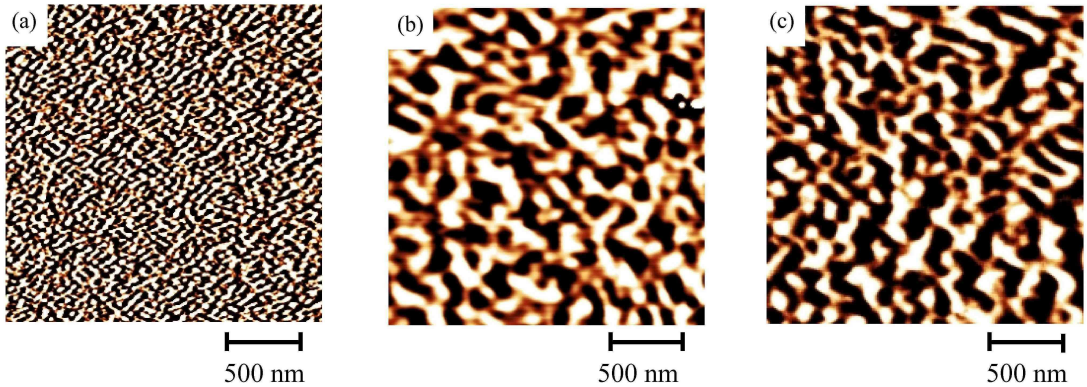

Figure 5.12 – MFM images for (a) FePt(20), (b) Pt/FePt(20) and (c) Pt/FePt(15).

The enhancement of the anisotropy induced by the Pt underlayer in Pt/FePt(20) sample causes an increase of the domain sizes and a change of the domain configuration into a maze-like pattern [Fig. 5.12(b)]. The reduction of the FePt film thickness induces only a slight increase of the domain sizes [Fig. 5.12(c)].

The shapes of the hysteresis loops for the Pt/FePt films suggest the presence of two correlated mechanisms for the magnetization reversal. Starting from the saturation and for applied external fields lower than the coercive field H_c, the magnetization abruptly decreases as a consequence of the nucleation of a reversed domain and of a cooperative reversal of the magnetic moments. Above H_c a rounding of the loop occurs due to the gradual unpinning of the domain walls.

This behaviour is characteristic of materials having a value of the nucleation field that lies into the energy barrier distribution for the domain wall pinning. This is confirmed by the DCD and IRM irreversible susceptibility curves, χ_{irr}^{DCD} and χ_{irr}^{IRM} respectively, reported in Fig. 5.13 for Pt/FePt samples. For both films, the two peaks of the χ_{irr}^{DCD} indicate the presence of two main mechanisms for the magnetization reversal. Moreover the maximum of χ_{irr}^{IRM} is in between those of the χ_{irr}^{DCD} curve suggesting that the energy barrier for the nucleation of a reversed domain lies within the energy barrier distribution for the wall pinning.

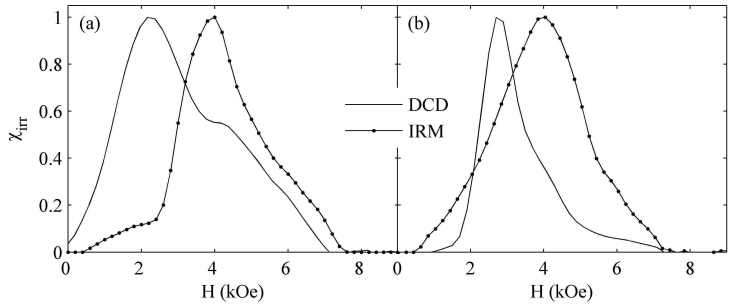

Figure 5.13 – Normalized DCD and IRM irreversible susceptibility for (a) Pt/FePt(20) and (b) Pt/FePt(15).

It is to be noted that by reducing the FePt film thickness a narrowing of χ_{irr}^{DCD} curve occurs and the main distance between the two maxima reduces. These two facts indicate an increase of the exchange interaction among the magnetic grains.

To study the nature and the strength of the interparticle interactions the ΔM curves have been evaluated (Fig. 5.14). The negative values of the ΔM curve for Pt/FePt(20) sample indicate the presence of interparticle magnetostatic interactions. On the contrary, in Pt/FePt(15) sample, the positive values of the ΔM curve indicate the presence of exchange-coupling interactions. These interactions drop suddenly to negative values during the magnetization reversal as a result

of the cooperative switching of the exchange-coupled grains. Therefore for fields higher than H_c the magnetostatic interactions become dominant.

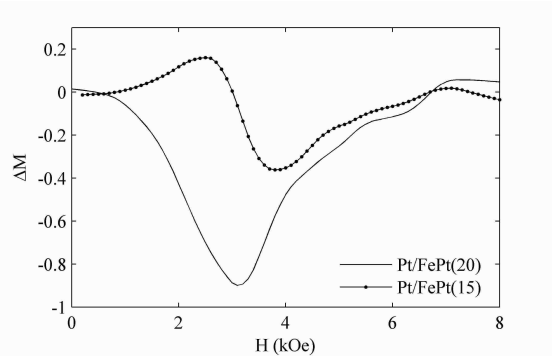

Figure 5.14 – Δ*M* plots for Pt/FePt(20) and Pt/FePt(15) samples.

The presence of exchange-coupling interactions among the grains and the more cooperative reversal of the magnetic moments in the thinner film cause the higher squareness of the hysteresis loop [Fig. 5.11(c)].

Chapter 6

FePt/Fe Bilayers

A key feature in the magnetic recording technology is the areal density $(BH)_{max}$ representing the maximum information density that can be stored in a media. Two factors can affect the achievement of a very high areal density: the superparamagnetic limit and the engineering factors connected to the writing and reading heads. The intrinsic properties of $L1_0$-ordered FePt alloy have attracted much interest making FePt the main candidate for next generation of ultrahigh density magnetic storage media.

Thin films of $L1_0$-ordered FePt alloy can develop a strong uniaxial magnetocrystalline anisotropy allowing to overcome the superparamagnetic limit also for particles of a few nanometers in size[73]. Moreover the possibility to induce a perpendicular anisotropy can favour a further enhancement of the areal density, thanks to a reduction of the bit width. As for the engineering factors a limit is imposed to the coercivity developed by the media that must be lower than 10 kOe. The possibility to control the microstructure of FePt films by adjusting the growing parameters allows to obtain media with moderate coercivity, preserving a high value of the anisotropy field.

In this regard, perpendicular exchange-spring magnets can allow a strong increase of the maximum energy product $(BH)_{max}$ and contemporary a moderate coercivity thanks to the presence of the soft phase that can increase the remanence to saturation ratio and reduce the magnetic hardness of the hard one, allowing the writability of information.

In the case of FePt-based nanocomposites, the presence of a finely dispersed mixture of ordered $L1_0$ and disordered $A1$ phases can be responsible for the high coercivity, inducing stresses and pinning sites which hinder the domain wall motion[64,74]. A significant enhancement of the remanence[75-79] can be obtained in systems containing both hard $L1_0$ and soft Fe_3Pt phases.

In recent years the attention has been addressed to the development of nanocomposites in the form of multilayers where the $L1_0$ phase is intercalated with a soft magnetic phase[80-82]. A multilayer is an intrinsically simple system whose nature and structure is well controllable and reproducible, moreover showing interesting aspects concerning basic physics related to interfacial phenomena[83-85].

The main difficulty concerns the requirement to maintain the crystallographic coherence when a soft magnetic layer is grown on the top of the hard film[10]. Another difficulty arises from the presence of strong demagnetizing fields that can reduce the remanence to saturation ratio and harm the exchange coupling interaction. In this regard, severe restrictions are to be observed about the ratio between soft and hard thickness values in order to obtain both a good exchange coupling between the intercalated phases and a sufficiently high nucleation field[13,73,80,86]. In particular, the size of the soft layer must be a few times the width of a Bloch domain wall of the hard phase (~4 nm for FePt[73]) with grain size lower than 30 nm[80].

Recent works concerning non-epitaxially grown Co/Fe multilayers[87] have shown that the low degree of intermixing at the interfaces, the surface flatness and the intimate contact between the layers are important factors for obtaining exchange-coupled magnets displaying a singular phase magnetic behaviour, in spite of a high value of the ratio between the thickness of the soft and hard phases. Moreover, these systems have shown a strong uniaxial in-plane anisotropy, a property which tends to weaken as the thickness of the Fe layer is increased, with a concomitant increase of the out of plane component of the magnetization[88]. The loss of coherence and the increased coercivity observed for increasing values of Fe thickness were attributed to enhanced effects of morphological disorder and defect density[89].

6.1 $L1_0$-FePt/Fe Bilayers Grown Using Two Different Growing Techniques

Taking into account all the difficulties concerning the development of well exchange-coupled spring magnets, we have decided to exploit two different growing techniques for the development of exchange spring magnets showing a single-phase magnetic behaviour.

$L1_0$-FePt/Fe bilayers were deposited using the rf sputtering and the UHV e-beam evaporation techniques for the growth of the hard and soft component respectively.

The rf sputtering growth processes are characterized by high energies that favour the formation of pinning sites in the alloy hindering the domain wall motion and promoting high

coercivity values. On the contrary, the e-beam deposition was adopted for the growth of the soft phase assuming that this technique can favour a good arrangement of iron atoms, low stresses at the interfaces and therefore the establishing of a strong exchange coupling between the magnetic phases.

The hard FePt sputtered films [FePt(20), Pt/FePt(20) and Pt/FePt(15)] were selected as the hard components. The soft phases are constituted by Fe highly enriched by ^{57}Fe isotope and were evaporated in ultra-high vacuum at room temperature on top of the hard sputtered films. The thicknesses were 7 and 14 nm. The growth rate of these outer layers was ~ 6 Å/min, the vacuum ~10^{-9} mbar. The layer thickness was measured "in situ" by a quartz micro-balance.
In the following these bilayers are called *FePt(20)/Fe(t)*, *Pt/FePt(20)/Fe(t)* and *Pt/FePt(15)/Fe(t)*, where t = 7 and 14 is the thickness of the soft Fe layer.

The interdiffusion phenomena occurring at the FePt/Fe interface have been studied by Mössbauer spectroscopy and related to the exchange coupling occurring between the different magnetic phases. In order to make Mössbauer measurements sensitive only to the soft phase and to the compounds eventually formed as a consequence of the Fe diffusion and reaction with the hard FePt film, iron highly enrich in ^{57}Fe isotope has been used for the growth of only the soft phase.

The magnetic measurements performed for the FePt(20) film covered by a 7 nm Fe layer, FePt(20)/Fe(7), are shown in Fig. 6.1(a).

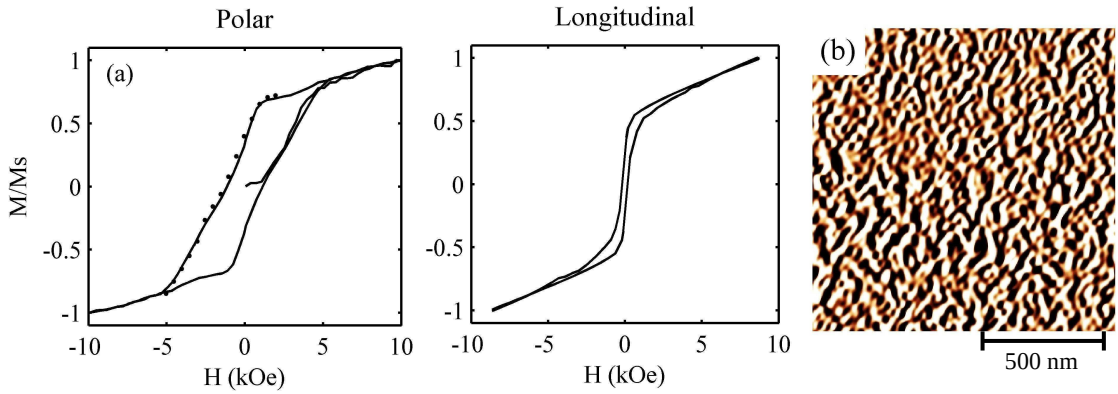

Figure 6.1 – (a) Polar and longitudinal hysteresis loops of the FePt(20)/Fe(7) bilayer. (—) Hysteresis loops and initial curves; (•) DCD remanence curves. (b) MFM image.

The hysteresis loops show in both geometries the difficulty to reach the complete saturation suggesting a tilting of the easy axis from the perpendicular to the film plane. This effect is due to the presence of the soft layer that enhances the demagnetizing effects lowering the anisotropy strength and favouring an in-plane orientation.

Taking into account the presence of the demagnetizing field during the extrapolation of the polar remanence curve, the complete overlapping between this curve and the hysteresis loop

indicates the establishing of a good exchange coupling between different magnetic phases. The magnetic properties are typical of an exchange-coupled magnet. The more marked kink in the first magnetization curve of the bilayer [Fig. 6.1(a)] with respect to that of the hard phase [Fig. 5.11(a)], suggests that a strengthening of the domain wall pinning mechanism occurs in the bilayer as a consequence of the iron deposition. This strengthening of domain wall pinning gives rise to a little increase of the coercive field.

The MFM image [Fig. 6.1(b)] for the bi-layer shows a stripe domain pattern as in the case of the FePt(20) film [Fig. 5.12(a)], with lower sizes and the presence of a better directionality. The lower sizes are due to the presence of the soft layer that reduces the anisotropy strength, while the better directionality can be attributed to the significant component of the magnetization preferentially oriented in the film plane.

The CEMS spectrum [Fig. 6.2(a)] can be interpreted as the superposition of two sextets, two doublets and a singlet whose hyperfine parameters are reported in Table IV.

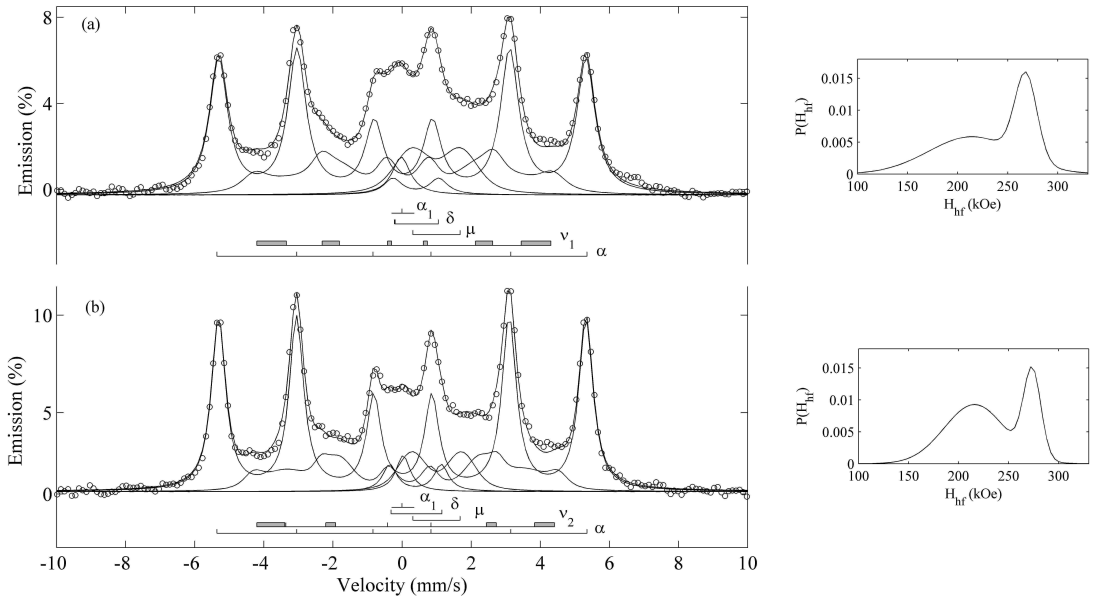

Figure 6.2 – CEMS spectra of (a) the FePt(20)/Fe(7) and (b) the FePt(20)/Fe(14) bilayers and the hyperfine field distributions relative to ν_1 and ν_2 sextets.

^{57}Fe easily diffuses into the FePt hard film along preferential path such as low density zones and grain boundaries giving rise to Fe in the form of superparamagnetic small particles (α_1 singlet). The δ and ν_1 contributions can be attributed to a ^{57}Fe-rich FePt compound characterized by a large grain size distribution, formed as a consequence of the reaction of the soft ^{57}Fe with the FePt hard film. In particular, doublet δ can be due to the ^{57}Fe-rich FePt compound in the form of small particles showing superparamagnetic properties, while ν_1 sextets

can be ascribed to larger particles showing a collapsing H_{hf} distribution[90-91] which decreases from the value typical for the tetragonal ordered phase.

Finally, the α contribution is due to ferromagnetic α-Fe while the μ doublet can be reasonably attributed to ^{57}Fe atoms which entered the MgO substrate[92] in zones which, remaining shielded by the substrate locking system during the rf sputtering growth, becomes available for a direct deposition of Fe during the subsequent e-beam evaporation.

Table IV. Hyperfine parameters of the contributions to the spectra reported in Fig. 6.2

	α_1	δ	ν_1	ν_2	α	μ
IS(mm/sec)	-0.01	0.39	0.11	0.15	-	0.98
ΔE_Q(mm/sec)	-	1.35	-0.1	-0.1	-	1.41
H_{hf} (kOe)	-	-	268, 214*	270, 215*	330	-

*Main peaks of the H_{hf} distribution

By increasing the thickness of the evaporated soft ^{57}Fe layer to 14 nm the α contribution increases, while the relative amounts of the other contributions remain substantially the same [Fig. 6.2(b)]. These facts suggest that the superparamagnetic-Fe and the ^{57}Fe-rich FePt compound form at the hard/soft interface. Taking into account the thickness of the ^{57}Fe evaporated layers and assuming a mean density for the FePt alloy, this interfacial region was about 2 nm thick.

The hysteresis loops performed on the FePt(20)/Fe(14) bilayer (Fig. 6.3) shows that a complete reorientation of the easy axis occurs. The in-plane anisotropy is due to the enhanced effect of the demagnetizing field along the normal to the film plane induced by the high thickness of the soft layer, that also makes the bilayer very soft.

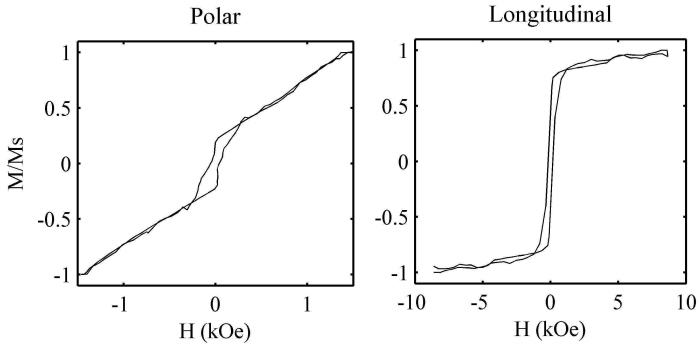

Figure 6.3 – Hysteresis loops of FePt(20)/Fe(14) bilayer.

A completely different situation takes place if the ^{57}Fe layer 7 nm thick is evaporated on top of Pt/FePt(20) film. The CEMS spectrum for Pt/FePt(20)/Fe(7) [Fig. 6.4(a)] shows the absence of the contribution due to ferromagnetic α-Fe. The evaporated iron easily diffuses

giving rise to superparamagnetic-Fe (α_1 singlet) and to the ^{57}Fe-rich FePt compound characterized by a large grain size distribution showing collapsing hyperfine magnetic fields (β contribution) [Fig. 6.4(b)] up to the superparamagnetic limit (ε doublet). The hyperfine parameters are reported in Table V.

The shape of the hysteresis loop and its good overlapping with the remanence curve [Fig. 6.4(c)] suggest that a good exchange coupling established between the hard and soft phases. In particular, the loop is characterized by only one critical field that coincides with the coercive field: by decreasing the applied external field the magnetization gradually decreases and only for field around H_c the rotation becomes irreversible giving rise to an abrupt transition. It is to be noted that in this case the exchange interaction develops between the hard FePt layer and the ^{57}Fe-rich FePt compound showing soft ferromagnetic properties.

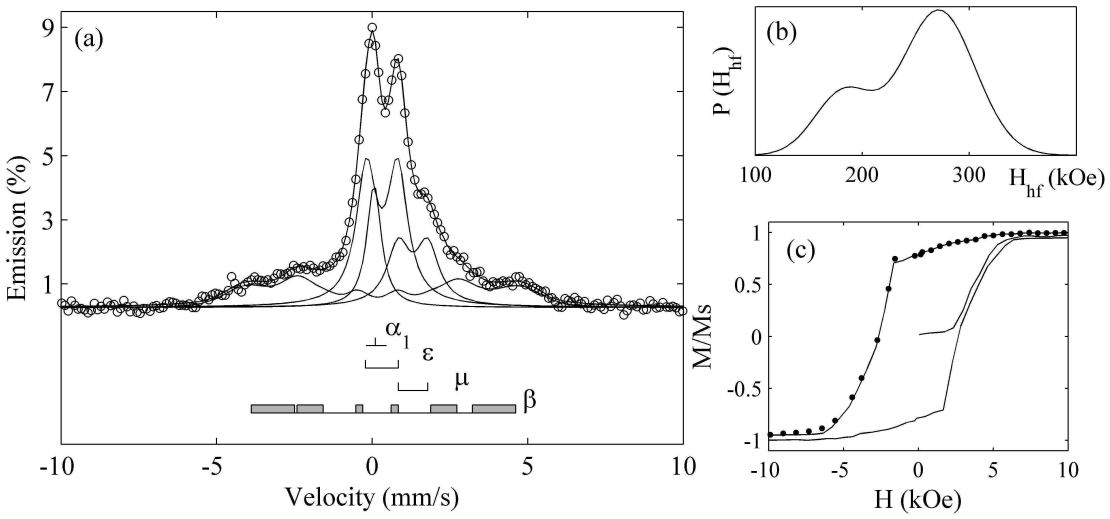

Figure 6.4 – (a) CEMS spectrum, (b) hyperfine field distribution relative to β contribution and (c) (—) hysteresis loop and (•) DCD remanence curves for Pt/FePt(20)/Fe(7) bilayer.

The first magnetization curve indicates that the main mechanism controlling the coercivity is the domain wall pinning. The more marked kink in this curve with respect to that of Pt/FePt(20) hard film [Fig. 5.11(b)] indicates a strengthening of this mechanism.

The presence of the soft layer gives rise to a reduction of the remanence ratio M_r/M_s, substantially without decreasing the value of the coercive field. The lower value of M_r/M_s and the difficulty to reach the complete saturation can only be linked to the presence at the hard/soft interface of a region constituted by Fe and ^{57}Fe-rich FePt compound showing superparamagnetic properties.

Table V. Hyperfine parameters of the contributions to the CEMS spectra reported in Figs. 6.4(a) and 6.5(a)

	α_1	ε	β	β_1	α	μ
IS(mm/sec)	0.01	0.38	0.24	0.11	-	0.99
ΔE_Q(mm/sec)	-	1.10	0.18	0.18	-	1.41
H_{hf} (kOe)	-	-	283, 194*	290, 243*	329.8	-

*Main peaks of the H_{hf} distribution

When the 7 nm thick iron layer is grown on top of the Pt/FePt(15) film, the CEMS spectrum [Fig. 6.5(a)] shows that:

- α-iron, which in Pt/FePt(20)/Fe(7) sample is only present in the form of small particles [Fig. 6.4(a)], in Pt/FePt(15)/Fe(7) is present both as small particles (singlet α_1) and as a normal ferromagnetic phase (sextet α), the last giving the prevailing contribution to the spectrum.
- The contribution from the ^{57}Fe-rich FePt superparamagnetic small particles (ε doublet) is considerably decreased with respect to that in the spectrum of Pt/FePt(20)/Fe(7).
- The H_{hf} distribution [Fig. 6.5(b)] for the ^{57}Fe-rich FePt compound (β_1 contribution) in Pt/FePt(15)/Fe(7) shows peaks which are better defined than that in Pt/FePt(20)/Fe(7) (β contribution) and shifted towards higher values. These facts suggest that this compound is present in Pt/FePt(15)/Fe(7) with a better defined stoichiometry and with a narrower particle size distribution.

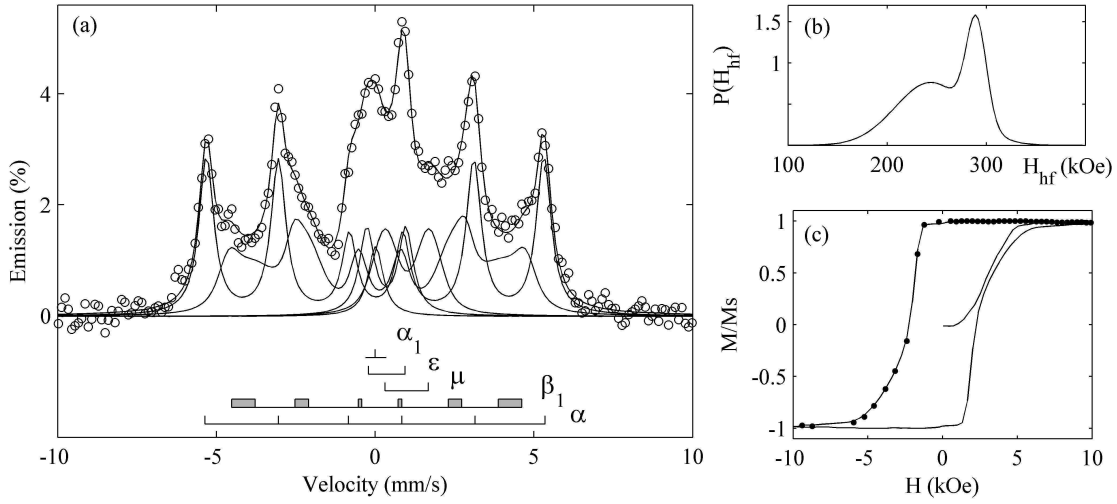

Figure 6.5 – (a) CEMS spectrum, (b) hyperfine field distribution relative to β_1 contribution and (c) (—) hysteresis loop and (•) DCD remanence curves for Pt/FePt(15)/Fe(7) bilayer.

The shape of the hysteresis loop [Fig. 6.5(c)] is typical of a single phase magnet. This is confirmed by (i) the complete overlapping of the remanence curve with the hysteresis loop and (ii) the presence of only one critical field for the magnetization reversal. Respect to

Pt/FePt(20)/Fe(7) sample, the bilayer reaches the complete saturation and the coercive field decreases with respect to that of the hard Pt/FePt(15) film [Fig. 5.11(c)].

The different degree of Fe diffusion into the hard Pt/FePt films can be due only to a different morphology of the hard FePt layers. In effect AFM images (Fig. 6.6) performed on the surfaces of Pt/FePt(20) and Pt/FePt(15) samples show very different morphologies. The thicker hard film is characterized by a very roughness and defective surface, indicating a low compactness allowing a high permeability to Fe diffusion.

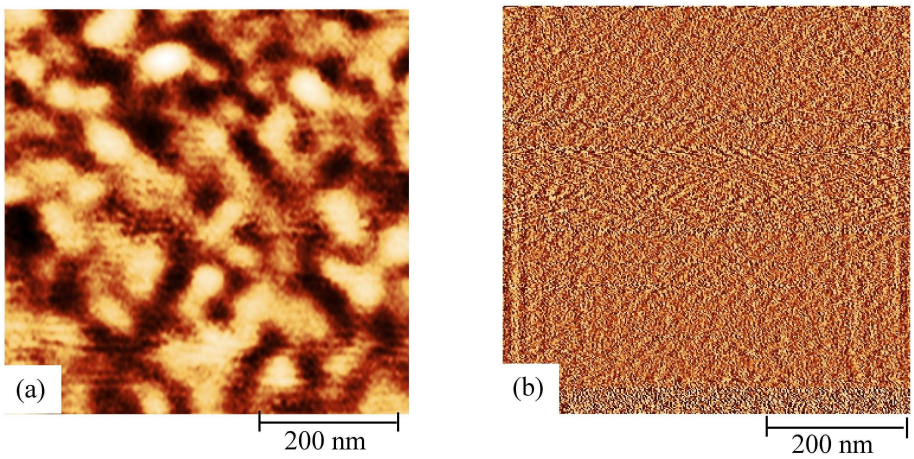

Figure 6.6 – AFM images for (a) Pt/FePt(20) and (b) Pt/FePt(15) sputtered hard films.

For the thinner film, no signal due to the interaction of the sample surface with the tip probe can be detected and the AFM image only shows electronic noise [Fig. 6.6(b)]. This indicates the presence of a very smooth surface with grains having sizes much lower than the resolution (< 20 nm) of the used microscopy. This higher compactness is the cause of the lower Fe diffusion into the hard FePt phase. The very smooth surface of the thinner sputtered film can be due to the fact that the lower FePt thickness favours the establishing of a lower temperature gradient between the substrate and the film surface during the growth process.

In both cases the ferromagnetic Fe and ^{57}Fe-rich FePt compound can grown only after the formation at the hard/soft interface of a layer constituted by Fe and ^{57}Fe-rich FePt compound in the form of superparamagnetic small particles. The strong exchange coupling between hard and soft layers seems to be ascribed to the formation of this interfacial region.

The increase of the soft Fe layer thickness to about 14 nm gives rise in the Mössbauer spectrum only to an increase of the relative area of the contribution due to ferromagnetic α-Fe [α sextet, Fig. 6.7(a)]. The H_{hf} distribution [Fig. 6.7(b)] for the ^{57}Fe-rich FePt compound becomes much more broad and more shifted to higher field values with respect to that reported in Fig. 6.5(b).

The easy magnetization remains oriented along the perpendicular to the film plane in spite of the strong effects due to dipolar interactions [Fig. 6.7(c)]. However, the impossibility to reach the saturated state indicates the presence of a magnetization component oriented in the film plane and characterized by a significant magnetic hardness. The shape of the hysteresis loop and the presence of a reversible magnetization component in the remanence curve indicate that the bilayer behaves as an exchange-coupled magnet.

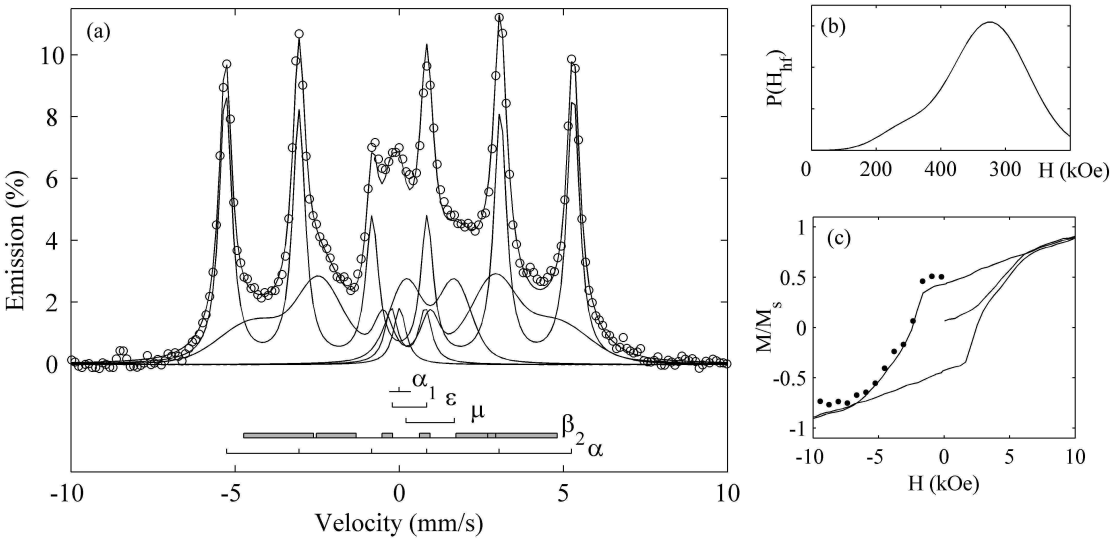

Figure 6.7 – (a) CEMS spectrum, (b) hyperfine field distribution relative to β_2 contribution and (c) (—) hysteresis loop and (•) DCD remanence curves for Pt/FePt(15)/Fe(14) bilayer.

The use of two techniques properly selected for the deposition of the soft and hard component can be promising in the development of exchange-spring magnets. The effectiveness of this choice is proved by the development of well exchange-coupled systems showing a single-phase magnetic behavior both in the case of a high soft/hard thickness ratio and in the presence of strong demagnetizing fields.

6.2 Interparticle Interactions

In the previous section, the behaviours of the bilayer remanence curves have been discussed. In particular, the shape of the recoil loops and their good overlapping with the hysteresis loops indicate a single-phase demagnetization behaviour, suggesting the establishing of a strong exchange-coupling among the different magnetic phases.

In materials consisting of particles in close contact with each other, magnetization reversal is also influenced by magnetic interactions among particles. These interactions can be of exchange or dipolar type and strongly influence the magnetic microstructure. Indeed the

magnetization processes can be cooperatives, in which two or more particles are involved (coherent rotation and curling), or non-cooperatives in the case of an ensemble of non-interacting particles.

A way to characterize the degree of cooperation of a system is to use the irreversible susceptibility χ_{irr}^{DCD}, obtained by differentiating the DCD remanence curve. This curve is a measurement of the switching field distribution (SFD) i.e. of the energy barriers that oppose to the magnetization reversal.

The irreversible susceptibilities for the Pt/FePt hard layers and Pt/FePt/Fe bilayers are reported in Fig. 6.8. They have been calculated after the remanence curves have been corrected for demagnetization effects. For all the samples, the magnetization reversal starts in positive applied fields as can be observed by the position of the main peaks of the SFD function. Moreover all these curves are characterized by two peaks indicating the presence of two correlated mechanisms for the magnetization rotation, an initial nucleation of a reversed domain followed by a slower depinning of the domain walls for applied field greater than the coercive field.

The narrowing of the full width at half maximum of the χ_{irr}^{DCD} curves for the bilayers with 7 nm thick Fe layer indicates a reduction of the energy barrier distribution to the magnetization reversal. Moreover the reduction of the height of the second kink and the lower distance among the two peaks of the χ_{irr}^{DCD} can be attributed to a more cooperative reversal of the magnetic moments, due to an increase of the strength of the exchange interactions among the grains.

By increasing the Fe layer to 14 nm, a broadening of the energy barriers occurs [Fig. 6.8(b)]. This broadening can be attributed to the presence of an in-plane oriented component of the magnetization as evidence by the shape of the hysteresis loop reported in Fig. 6.7(c).

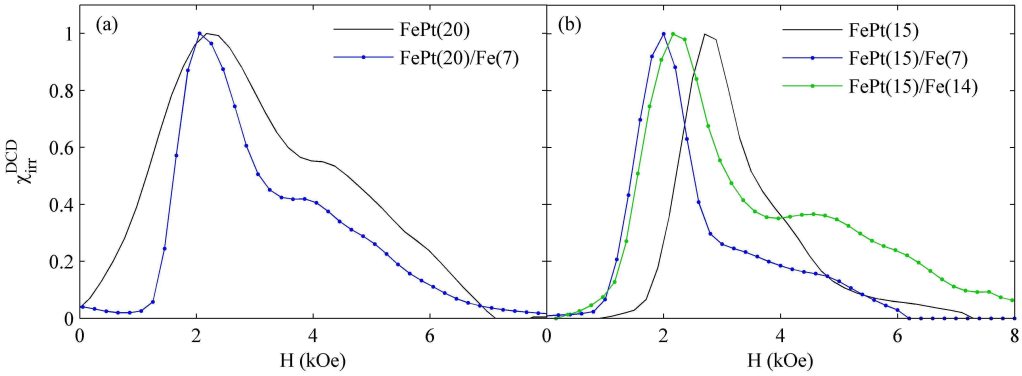

Figure 6.8 – χ_{irr}^{DCD} curves for (a) Pt/FePt(20) and Pt/FePt(20)/Fe(7) and (b) for Pt/FePt(15), Pt/FePt(15)/Fe(7) and Pt/FePt(15)/Fe(14) samples.

Another way to directly study the typology and the strength of the magnetic interparticle interactions consists in the analysis of the ΔM plots (Section 3.4). In particular $\Delta M = 0$, for an

assemblies of single-domain non-interacting particles, $\Delta M > 0$ if exchange-type interactions are present among the grains and $\Delta M < 0$ if the predominant interactions are of magnetostatic-type.

For all the bilayers the $\Delta M(H)$ plot has negative values, suggesting the presence among the grains of magnetostatic interactions. Only Pt/FePt(15) sample shows positive values of the $\Delta M(H)$, indicating the presence of interparticle exchange coupling interactions. The establishing of this type of interactions gives rise to the well square-shaped hysteresis loop in Fig. 5.11(c).

For Pt/FePt(20)/Fe(7) sample, the increase of the interparticle exchange interactions can be deduced by the lower negative values of the ΔM with respect to those of the corresponding hard phase. This increase is not able to significantly reduce the coercive field of the hard film [Fig. 6.8(a)] suggesting that some structural defects form in the bilayer hindering the domain wall motion.

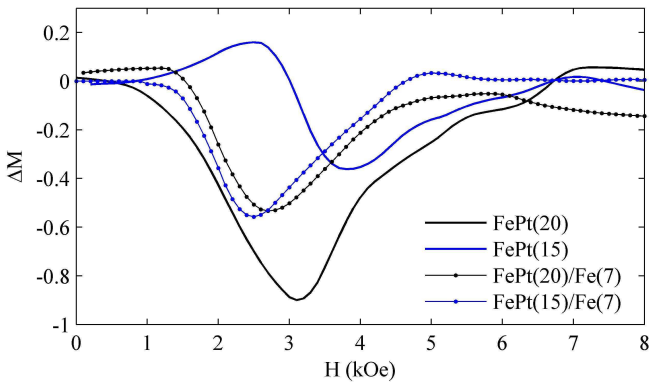

Figure 6.9 – ΔM plots for the Pt/FePt films and Pt/FePt(t)/Fe(t) bilayers.

In the case of Pt/FePt(15)/Fe(7) bilayer, the negative values of the $\Delta M(H)$ curve with respect to that of the corresponding hard layer [Pt/FePt(15)], can only be due to the formation of the superparamagnetic layer at the soft/hard interface. This layer constituted by very small particles of Fe and Fe-rich FePt compound, can favour a decoupling of the grains.

On the other hand, the presence of this superparamagnetic interfacial layer seems to favour the establishing of a strong exchange coupling among different magnetic phases. The bilayers show a single-phase magnetic behaviour both in the presence of strong demagnetizing fields and in the case of a high soft/hard thickness ratio. In effect, the narrowing of the SFDs and the decrease of the coercive field value with respect to those of the hard phases are possible only if the soft phase is strongly exchange-coupled to the hard one and in this way able to modify the switching behaviour of the hard magnetic grains.

Chapter 7

Ultra-Thin FePt Films and FePt/Fe Multilayers

The sputtering technique is the most commonly used growing technique for the deposition of hard FePt films, favouring the development of high values of the coercive field. This is due to the formation of a microstructure with a high density of defects acting as pinning sites for domain wall motion.

However the anisotropy strength and the magnetic hardness of the FePt films are strongly influenced by the degree of epitaxy and of the chemical order of the alloy that develops during the growth. Indeed FePt films have been grown using the UHV e-beam deposition technique, whose low energetic growing processes can favour good epitaxial growths. In particular the attention has been addressed to the study of the microstructural and magnetic properties of FePt films with ultra-thin thicknesses. In this regime surface and interface phenomena become significant and strongly influence the magnetic properties of the samples. These phenomena can be exploited for the development of exchange-spring magnets having a high soft/hard thickness ratio.

The aims of the study were (i) to study the effects on the magnetic properties of varying the thickness of $L1_0$-FePt ultra-thin films, and (ii) to investigate the possibility to realize ultra-thin FePt/Fe perpendicular exchange spring magnets with a high soft/hard thickness ratio.

7.1 UHV e-beam Evaporated FePt Ultra-Thin Films

FePt films, 3.6 and 4.8 nm thick [*FePt(36)* and *FePt(48)*], were e-beam evaporated in UHV (~ 10^{-9} mbar) at 700°C on MgO (100) monocrystalline substrates by alternating Fe and Pt layers

0.6 nm thick. The film thickness was measured “in situ” by an oscillating quartz microbalance. The estimated stoichiometry is $Fe_{56}Pt_{48}$.

The XRD patterns measured for FePt(36) and FePt(48) [Figs. 7.1(a) and 7.1(b)] show only the preferred (001) and (002) reflections typical of the $L1_0$-ordered FePt alloy epitaxially grown onto (100)-MgO substrates. By increasing the film thickness, the linewidths of both reflections decrease indicating that an improvement in epitaxy occurred, favouring a lower dispersion of the contracted *c*-axis along the perpendicular to the film plane.

The very good structural order is proved by the high value of the order parameter which was evaluated to be 0.96 for both films. Moreover, the absence of significant difference in the peak positions in the XRD patterns indicates that the tetragonal distortion of the lattice was unaffected by the film thickness.

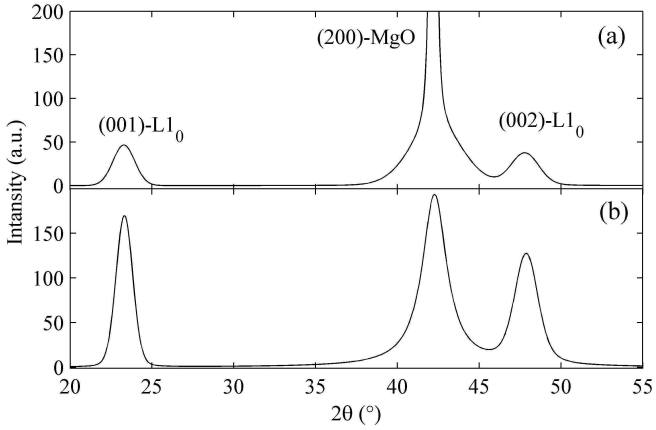

Figure 7.1 - XRD patterns measured for (a) FePt(36) and (b) FePt(48).

The shape of the hysteresis loop measured for FePt(36) [Fig. 7.2(a)] indicates that a strong perpendicular magnetocrystalline anisotropy develops as a consequence of the good epitaxial growth and chemical $L1_0$ order. The behaviour of the minor loops and the shape of the initial curve suggest that the domain wall pinning is the main mechanism controlling the coercivity. From the hysteresis loop obtained applying the maximum magnetic field of 15 kOe, a coercive field of 6.5 kOe was measured. The shape of this loop suggests that at 15 kOe the saturation magnetization is almost reached.

By increasing the film thickness up to 4.8 nm, a strong improvement of the magnetic hardness occurs, and only minor loops are allowed to be measured [Fig. 7.2(b)]. A coercive field of 9.5 kOe was measured applying in polar geometry the maximum magnetic field of 15 kOe. The saturation magnetization, evaluated from the Kerr rotation, was 520 in respect to that of 750 emu/cm^3 evaluated for the FePt(36). The lower value of M_s is in agreement with the fact that the complete saturation can be reached only at much higher values of applied fields.

The initial curve behaviour for FePt(48) indicates that for the thicker film a relevant strengthening of the domain wall pinning mechanism occurs. In effect, the first magnetization curve slowly rises with the applied magnetic field up to values closed to the coercive field, and then abruptly increases.

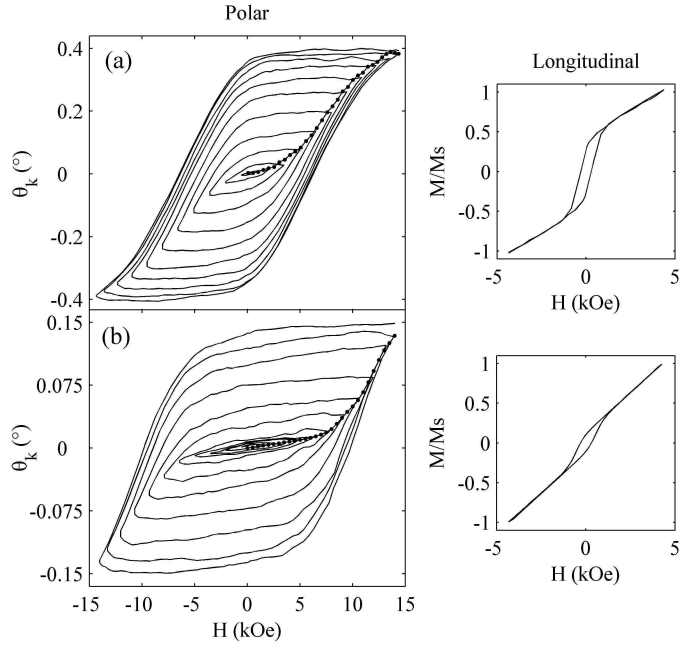

Figure 7.2 - MOKE measurements in polar (— minor loops and ••• initial magnetization curve) and longitudinal geometry for (a) FePt(36) and (b) FePt(48).

From the comparison between the longitudinal loops measured for FePt(36) and FePt(48) it follows that the last film is characterized by a better epitaxy and by a very good orientation of the *c*-axis along the normal to the film surface.

The improvement of the magnetic hardness can be related to the film morphology. The AFM images for FePt(36) and FePt(48) films are reported in Figs. 7.3(a) and 7.3(b) respectively. Both films show an island-like pattern, but, contrary to what expected, when increasing the film thickness, a reduction occurs of both the grain interconnection and the mean grain size. These facts may well cause the increase of coercivity of FePt(48) film.

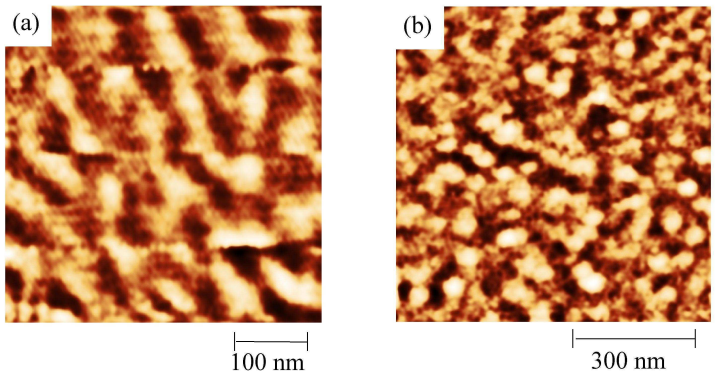

Figure 7.3 - AFM images recorded for (a) FePt(36) and (b) FePt(48) samples.

7.2 UHV e-beam Evaporated FePt/Fe/FePt Trilayers

FePt/Fe/FePt trilayers have been grown with the UHV e-beam evaporation technique on MgO monocrystalline substrates varying the thickness of the upper FePt layer. The hard FePt layers have been deposited at 700°C while the soft Fe layer has been grown at room temperature. The thicknesses of the Fe and of the FePt layer in contact with the substrate were fixed at 4.8 nm, while the thicknesses of the upper FePt layers were 1.2 and 4.8 nm. The obtained trilayers are respectively: *FePt(48)/Fe(48)/FePt(12)* and *FePt(48)/Fe(48)/FePt(48)*.

The minor loops and the initial magnetization curve, reported in Fig. 7.4(a) for FePt(48)/Fe(48)/FePt(12) sample, indicate that the trilayer is characterized by a strong perpendicular anisotropy and that, even for the maximum applied field of 15 kOe, no complete saturation was achieved. From the comparison with the measurements performed for the FePt(48) film [Fig. 7.2(b)], the trilayer shows a strong decrease of the squareness and of the coercive field (from 9.5 to 5.6 kOe) followed by an increase of the saturation magnetization (694 emu/cm^3 at an applied field of 15 kOe).

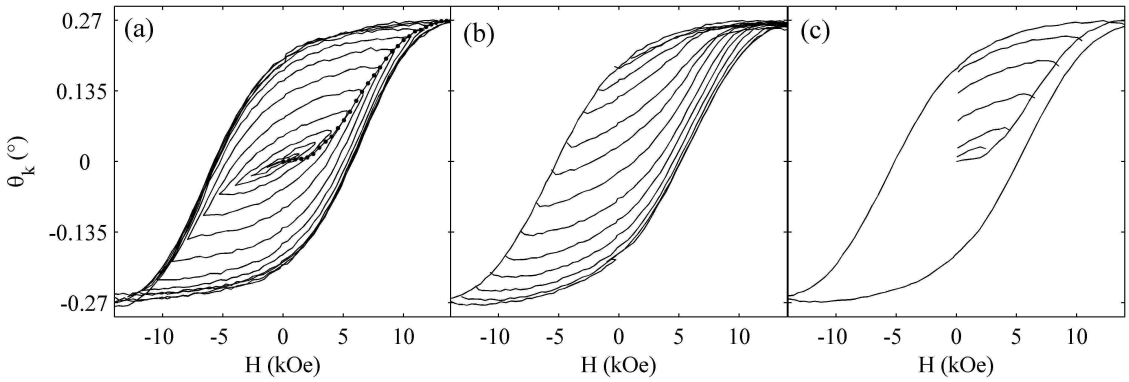

Figure 7.4 - (a) Minor loops, initial magnetization curve, (b) DCD and (c) IRM remanence curves for FePt(48)/Fe(48)/FePt(12) trilayer.

The DCD and IRM remanence curves measured for the trilayer and reported in Figs. 7.4(b) and 7.4(c) indicate that a significant reversible contribution to the rotation is present, reasonably due to the relevant amount of the soft phase present in the trilayer. On the other hand, the fact that the minor loops show only one critical field coinciding with the coercive field indicates that the trilayer behaves as a single phase magnet.

No significant changes were observed in the shape of the minor loops, coercivity and squareness when the thickness of the outer hard FePt layer is increased from 1.2 to 4.8 nm [FePt(48)/Fe(48)/FePt(48) sample].

The irreversible susceptibilities of the trilayers, obtained by differentiating the DCD and the IRM remanence curves with respect to the applied field [Figs. 7.5(a) and 7.5(b)], represent

the switching field distributions in both the magnetizing and demagnetizing mode. In particular, for the DCD case, the χ_{DCD}^{irr} represents a measurement of the energy barriers to domain nucleation, while in the IRM case, the χ_{IRM}^{irr}, is a measurement of the energy barriers to the domain wall propagation.

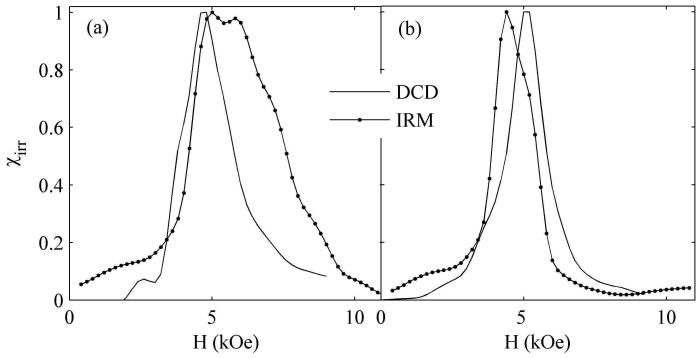

Figure 7.5 - Normalized irreversible susceptibility χ^{irr} obtained by differentiating the DCD and IRM curves with respect to the field for (a) FePt(48)/Fe(48)/FePt(12) and (b) FePt(48)/Fe(48)/FePt(48) trilayers.

The maximum of χ_{DCD}^{irr} for the trilayer with thinner top layer is shifted towards lower fields in respect to that of χ_{IRM}^{irr}, suggesting that the predominant coercivity mechanism is the domain wall pinning. On the contrary, for the trilayer with thicker top layer, the opposite behaviour of the two χ^{irr} suggests that the rotation of magnetization preferentially occurs by a coherent Stoner-Wohlfarth-like rotation of the moments. The two different mechanisms of magnetization reversal induced by the variation of the thickness of the upper FePt layer, suggests that in the thinner trilayer defects act as pinning sites for domain wall motion while in the thicker trilayer they act as preferential sites for the nucleation of a reversed domain.

Furthermore, the ΔM curves obtained from both the remanence curves (Fig. 7.6) indicate the presence in the trilayers of different intergrain interactions.

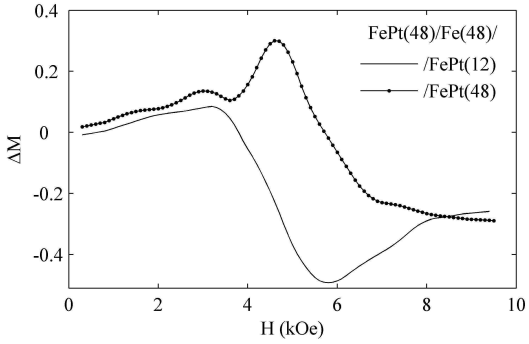

Figure 7.6 - ΔM curves for FePt(48)/Fe(48)/FePt(12) and FePt(48)/Fe(48)/FePt(48) trilayers.

For the thinner trilayer, interparticle interactions are mainly of magnetostatic type, while on the contrary for the thicker trilayer the positive values of the corresponding ΔM curve suggest

the presence of exchange-coupling interactions. The establishing of these exchange interactions among the particles in the thicker trilayer is also confirmed by the lower width of both χ^{irr} curves [Fig. 7.5(b)].

Figure 7.7(a) displays the AFM image recorded in tapping mode with a non-magnetic cantilever for the FePt(48)/Fe(48)/FePt(48) sample. The morphology of the surface is characterized by well defined islands with interconnected bases, elongated in shape and oriented along a preferred direction. Figure 7.7(b) in turn, shows the MFM image for the same demagnetized sample. The analysis was performed using a CoCr-coated magnetic tip in lift mode at a distance from the surface of 100 nm. The pattern is constituted by finely dispersed bubbles with dimensions three times larger than the average sizes of the islands. Moreover, these bubbles appear to be oriented along a preferential direction which is probably induced by the island orientation.

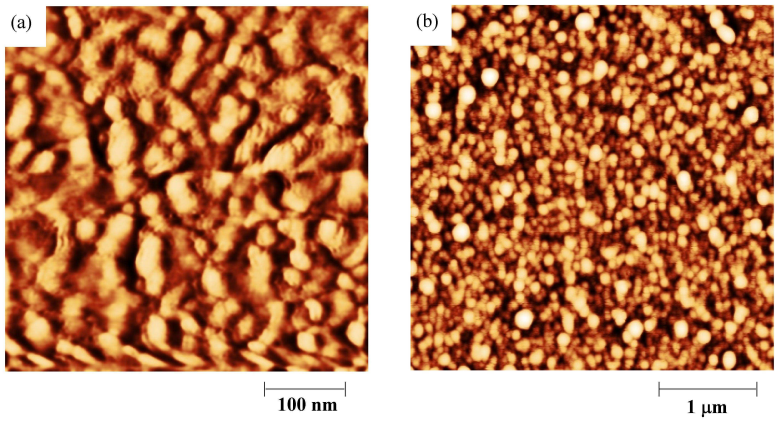

Figure 7.7 - (a) AFM and (b) MFM images for (48)/Fe(48)/FePt(48) trilayer.

These bubble domains belong to the greater family of interaction domains, which are characterized by sizes much higher than those of the islands. This characteristic, in agreement with the ΔM plot in Fig. 7.6, indicates the presence in the thicker trilayer of interparticle exchange interactions.

Chapter 8

FePd Films

The binary phase diagram of the Fe-Pd alloy (Fig. 8.1) is very similar to that of the Fe-Pt system (Fig. 5.1). Around the equiatomic composition the bulk FePd alloy shows a stable fcc disordered phase at high temperature and a tetragonal $L1_0$-ordered phase at temperature lower than 650°C. In the form of thin film, the disordered phase is stable also at room temperature, and the order-disorder phase transformation can occur at lower temperature than that reported for the bulk system (650°C). The tetragonal distortion induces a morphology transformation with the formation of twins that allow the accommodation of the strain and misfit energy formed during the process of ordering. As in the case of the Fe-Pt alloy, during the ordering there is a lowering of symmetry resulting in an increase of the lattice periodicity along the slip direction. This gives rise in the XRD pattern to superstructure reflections having twice the length of the fundamental ones.

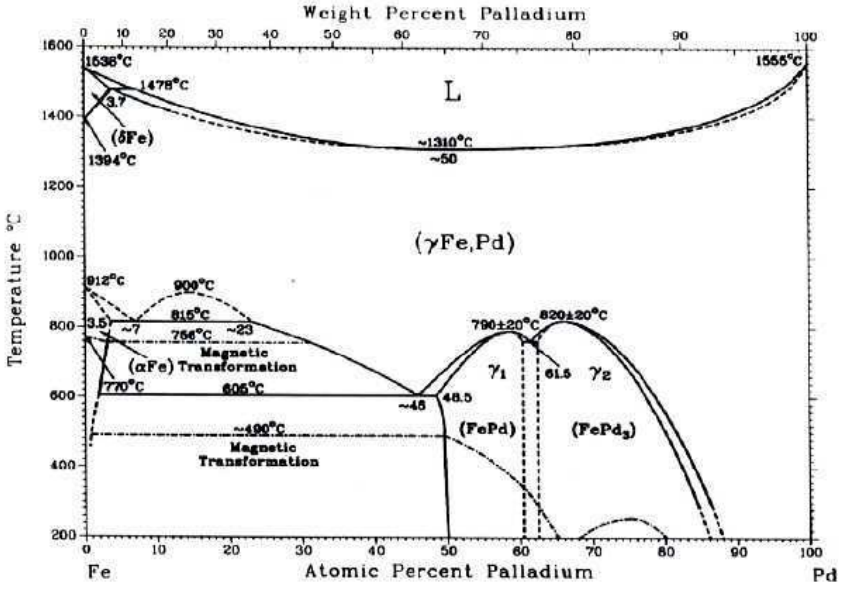

Figure 8.1 – Phase diagram of the Fe-Pd alloy.

Firstly this system has attracted attention because of its Invar behaviour around the Fe_3Pd composition; now it is studied as magnetic media and shape memory candidate.

To achieve long range order pure Fe and Pd planes must extend over large range and continuous flat regions, with a high lateral coherence and without defects. To favour long range order, a high temperature deposition is indispensable to promote 2D epitaxial growth mode, allowing the atoms to diffuse and adopt the correct position for the ordered phase. However from the technological point of view it is necessary to obtain nanostructured materials with a high degree of chemical order and strong magnetocrystalline anisotropy. In particular for application such as the magnetic recording, these nanostructures must be decoupled to minimize magnetic interactions among the grains since ideally each nanostructure would constitute a bit of information, whose magnetic state could be manipulate independently. In this case a 3D growth is preferable; this mode is favoured by high temperature growths and by high lattice mismatches[93].

The simultaneous presence of the long range order and 3D growth is challenging since the 3D growth inhibit the formation of long range order over large lateral scale.

MgO monocrystalline substrates exhibit a high lattice mismatch with FePd (10%) and the dielectric surface favours a 3D growth mode for the alloy. For this growth mode, molecular beam epitaxy is the most commonly used deposition technique[94-96]. Using different deposition techniques, involving different energies, and adjusting the growing parameters, it becomes possible to affect and control the growth mode, the degree of epitaxy, the morphology, the structure, the chemical ordering, the magnetic and magneto-optical properties of the alloy. For example FePd thin films grown with sputtering technique show a lower chemical order with respect to similar films grown with MBE, and the order can be obtain only for a narrow temperature range around 450°C[93].

Compared to the Fe-Pt alloy, the Fe-Pd system is characterized by a higher saturation magnetization, a lower order-disorder transition temperature, a lower perpendicular anisotropy ($K_u \sim 2 \div 3 \times 10^6$ erg/cm^3) and much lower coercivity values (hundreds of Oe). Moreover the hysteresis loops show in general a transcritical shape, due to the presence of strong demagnetizing fields overcoming the anisotropy one. A typical example is reported in Fig. 8.2, where the magnetic measurements have been performed on FePd thin films grown on (100)-MgO substrates using a molecular beam epitaxy (MBE) technique. The films have been deposited at 400°C and then subjected to post-annealing treatments for 1200 s at different temperature (400, 500 and 600°C).

Until now, better results, i.e. higher values of the coercive field, can only be obtained in nanostructured systems constituted by FePd nanoparticles with sizes lower than 10 nm[97]. The

control on the particle sizes is a hard task, which makes very difficult to obtain systems showing good chemical order and epitaxy. This hinders the establishing of a strong uniaxial anisotropy and contemporary favours the appearance of anisotropy components oriented in the film plane. Moreover the small particle sizes can induce superparamagnetic contributions, worsening the hard magnetic properties.

These difficulties have made the FePd system useful only for the study of magnetic domains and their dynamics.

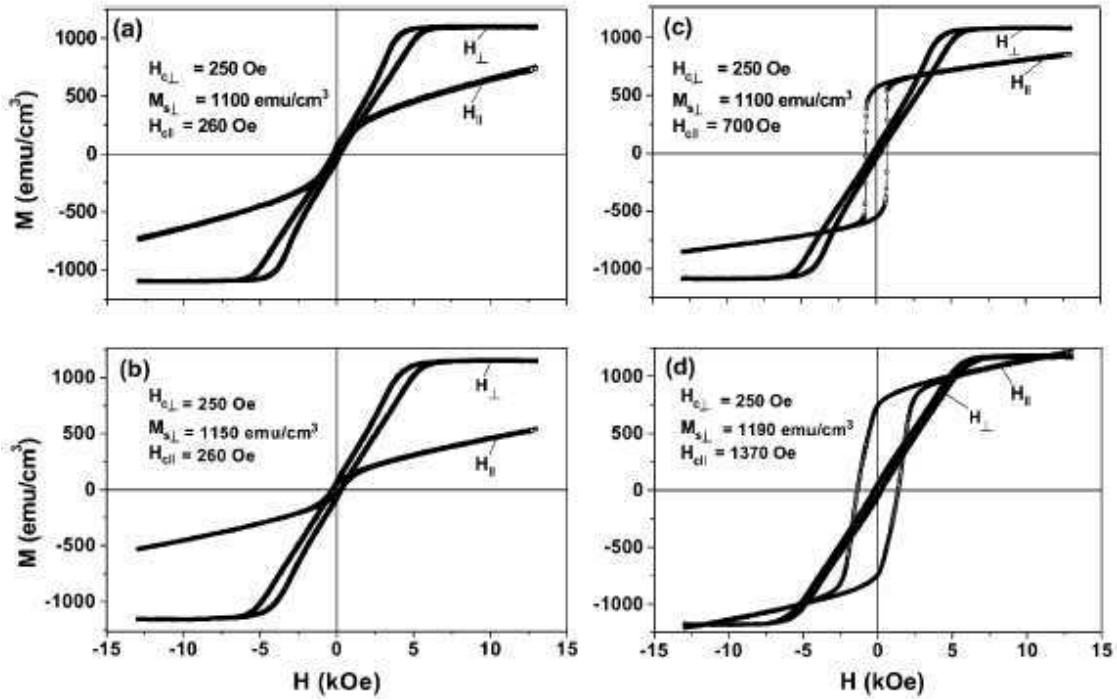

Figure 8.2 – Hysteresis loops for FePd thin films grown by MBE on MgO (100) monocrystalline substrates at 400°C. (a) As deposited; (b), (c), (d) post-annealed for 1200 s at 400, 500 and 600°C, respectively[98].

It is clear that it becomes very interesting to understand while the FePt and the FePd systems so similar from the structural point of view have such different magnetic behaviours.
Therefore ultra-thin films of FePd have been grown on MgO (100) monocrystalline substrates in UHV using the e-beam evaporation technique. The growth has been carried out by the alternated deposition of Fe and Pd thin layers, respectively 0.4 and 0.5 nm thick. The relative thicknesses of the single elemental layers have been adjusted to obtain a nominal composition of 50 at.% Fe. The total film thickness has been fixed to 4.5 nm, while the growing temperature was varied: room temperature, 300, 540 and 700°C. In the following these samples are indicated as *RTF*, *3F*, *5F*, *7F* respectively.

8.1 UHV e-beam Evaporated FePd Ultra-Thin Films

The hysteresis loops measured in polar geometry for FePd films 4.5 nm thick grown at RT and at 300°C, RTF and 3F samples respectively, are reported in Fig. 8.3. The RTF film shows magnetic properties typical of a soft ferromagnetic phase [Fig. 8.3(a)]. In spite of the room temperature growth, the film shows a good perpendicular anisotropy as can be deduced by the very low saturating field. This can be due to the easy intermixing at the Fe/Pd interfaces favoured both by the low thicknesses of the elemental layers and by the low growth rates (< 4 Å/min) that allow a good arrangement of the Fe and Pd atoms.

When the growth temperature is increased to 300°C, 3F film [Fig. 8.3(b)], an increase of the coercivity occurs with a concomitant strengthening of the demagnetizing field lowering the effect of the perpendicular anisotropy.

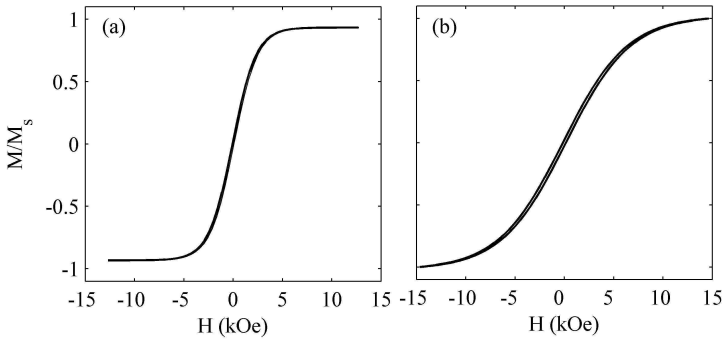

Figure 8.3 – Hysteresis loops of e-beam evaporated FePd films, 4.5 nm thick, grown at (a) room temperature (RTF) and (b) 300°C (3F).

The growing temperature induces an increase of the volume fraction of the ordered phase, but is not sufficient to induce a good (001) orientation of the *c*-axis. A possible tilting of the easy axis along the (111) direction can be argued.

The 5F film [Fig. 8.4(a)] shows a strong perpendicular anisotropy, with a coercive field of about 2.2 kOe and a remanence to saturation ratio $M_r / M_s = 0.9$. It is to be noted that despite that normally reported in literature (a main example is reported in Fig. 8.2), the effects due to the demagnetizing field are practically absent and no transcritical shape can be observed.

By growing the film at 700°C [Fig. 8.4(b)], a further enhancement of the magnetic hardness occurs. In effect for maximum applied fields of 15 kOe, only a minor loop can be measured. The coercive field reaches a value of 10.4 kOe and the squareness of the loop a value of 0.98.

By observing the first magnetization curve of 5F and 7F samples, the domain wall pinning is the main mechanism controlling the coercivity. By increasing the growing temperature a significant strengthening of this coercivity mechanism occurs, as can be deduced by the better

defined kink in the first magnetization curve of 7F sample. The magnetization remains practically zero until the applied field reaches the values of the coercive field, at which abruptly increases.

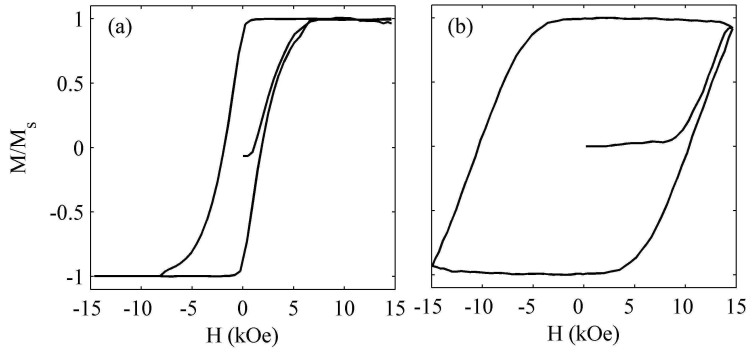

Figure 8.4 – Hysteresis loops and initial curves of e-beam evaporated FePd films, 4.5 nm thick, grown at (a) 540 and (b) 700°C, 5F and 7F samples respectively.

It is to be noted that, as reported at the beginning of this chapter, no data are reported in literature about coercive fields reaching these values (above 10 kOe) for FePd samples. In effect the hardness of 7F sample is well comparable with that of the FePt sample, 4.8 nm thick, grown at 700°C [Fig. 7.2(b)]. The hard magnetic properties and the strong magnetocrystalline anisotropy of FePt sample can be connected to the formation of a microstructure constituted by very small particles with sizes of ten nanometers in diameter that favour the development of high coercivity values [Fig. 7.3(b)].

The FePd film morphology is characterized by interconnected islands elongated in shape. In Figs. 8.5(a) and 8.5(b) AFM images for FePd samples grown at 540 (5F) and 700°C (7F) are reported. The low signal to noise ratio is due to the high smoothness of the surfaces that makes very difficult the image acquisition.

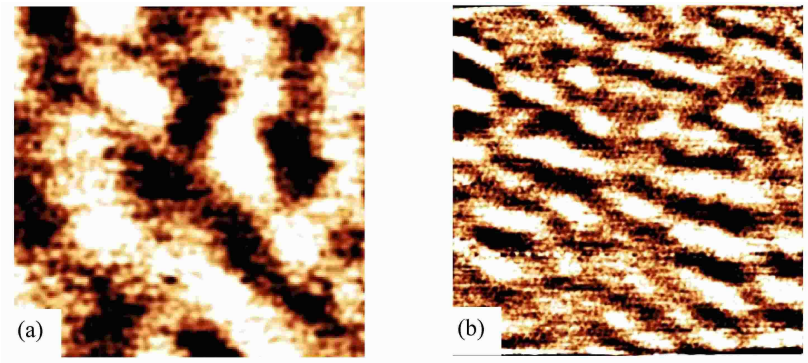

Figure 8.5 – AFM images (500 × 500 nm) recorded for FePd samples grown at (a) 540 and (b) 700°C.

By increasing the growing temperature, the islands decrease in size and tend to break, with the appearance of small grains with dimensions of ten nanometers. It is reasonable to suppose

that high temperature post-annealing treatments, could favour a further formation of small grains with a consequent improvement of the FePd hard magnetic properties.

The behaviours of the coercive field, of the M_r / M_s ratio, and of the saturation magnetization as a function of the temperature growth are reported in Fig. 8.6.

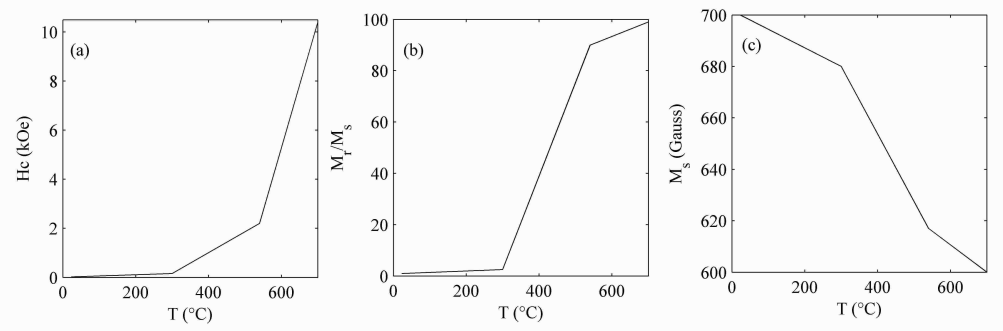

Figure 8.6 – (a) Coercive field H_c, (b) remanence to saturation ratio M_r/M_s and (c) saturation magnetization M_s behaviours as a function of the growing temperature.

The coercive field and the M_r / M_s ratio slowly increase for temperature lower or equal to 300°C, above which an abrupt increase occurs. The opposite behaviour is showed by the saturation magnetization [Fig. 8.6(c)] which decreases with increasing the temperature growth. This behaviour is due to the increasing volume fraction occupied by the ordered phase. The relatively low values evaluated for M_s are due to the very low thickness (4.5 nm) of the FePd films.

The measurement of the minor loops, that consists in recording the hysteresis loop for increasing applied fields, can be helpful for the identification in the sample of magnetic phases different from the predominant one.

The absence of kinks at low applied fields in the minor loops of 5F and 7F films (Fig. 8.7) suggests that these samples are magnetically homogeneous and constituted by only the hard $L1_0$-magnetic phase.

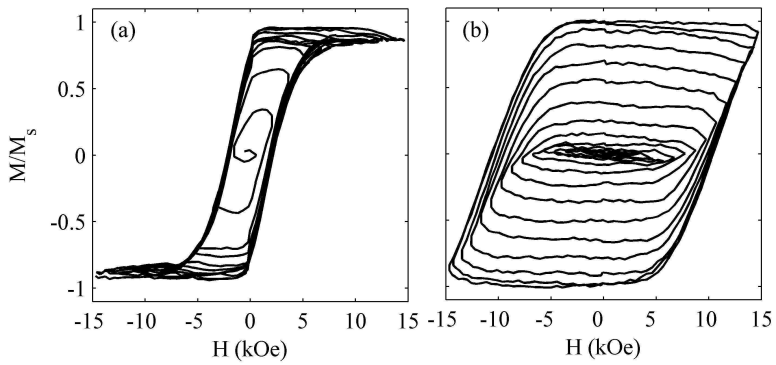

Figure 8.7 – Minor loops measured for (a) 5F and (b) 7F samples.

Moreover the absence of magnetization recovery in the recoil curves for these samples (Fig. 8.8) indicates that the moment reversal occurs only through irreversible switching of the magnetization.

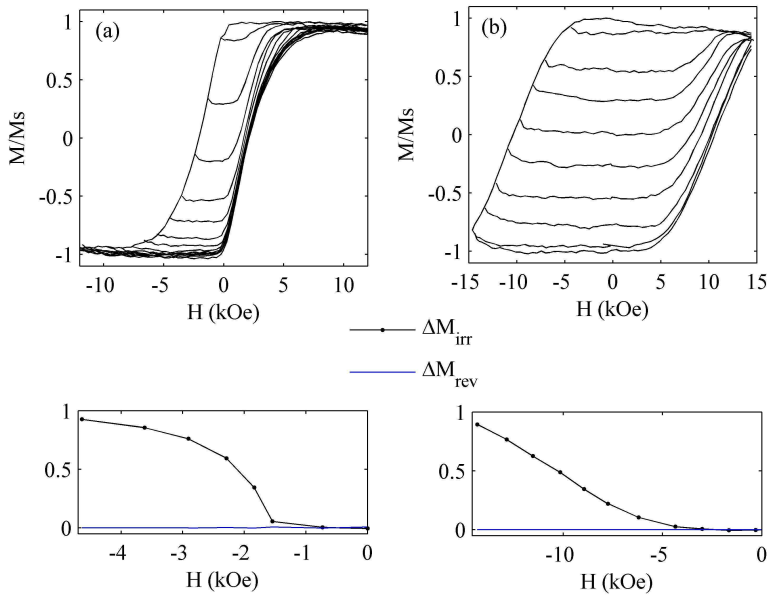

Figure 8.8 – Recoil curves measured for (a) 5F and (b) 7F samples, and the corresponding plots of the reversible and irreversible contributions to the magnetization rotation.

The reversible and irreversible contributions to the magnetization reversal process can be evaluated from the following equations:

$$\Delta M_{irr} = \frac{M_r^{DCD}(H) - M(H)}{M_r}; \quad \Delta M_{rev} = \frac{M_r - M_r^{DCD}(H)}{2M_r} \tag{8.1}$$

where $M_r^{DCD}(H)$ is the remanent value of the magnetization evaluated after the removal of the reversing field, M_r corresponds to the remanence for $H = 0$ and $M(H)$ is the demagnetization curve.

The results obtained using equations 8.1 are plotted in Fig. 8.8 below the recoil curves of 5F and 7F samples. The values of the reversible component are zero for all the applied reversing fields, and therefore the moment reversal occurs only through irreversible switching of the magnetization.

It is to be noted that for sample 7F the hysteresis loops performed in perpendicular [Fig. 8.4(b)] and in longitudinal geometry [Fig. 8.9(a)] show that the easy magnetization direction is intermediate between the parallel and perpendicular directions suggesting the presence of a 111-crystallographic texture. Also in longitudinal configuration, the hysteresis loop measured up to 15 kOe is only a minor loop, as the high anisotropy of this film makes the approach to the saturation very slow.

To confirm the hypothesis of a 111-texture of this sample the hysteresis loop has also been measured by applying the magnetic field at 45° from the surface normal [Fig. 8.9(b)]. The loop appears to be a little rotated because of the presence of both a polar and longitudinal contribution to the magnetization during the moment rotation.

The facts that (i) in this configuration the sample easily reaches the saturation state and (ii) the loop shows a perfect closure at the highest applied field indicate that the easy magnetization axis preferentially lies along the (111)-direction. XRD measurements are in progress in order to verify the presence of only the ordered $L1_0$-phase and the (111)-texture of these samples.

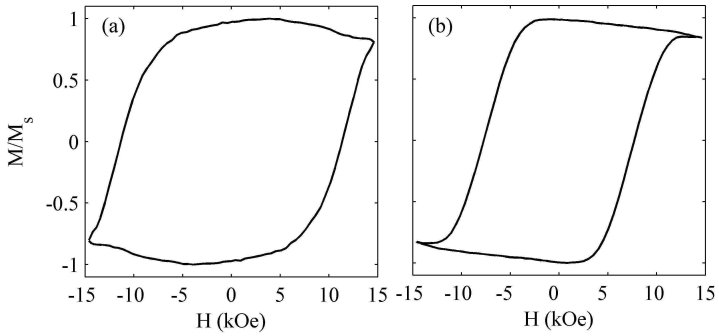

Figure 8.9 – Hysteresis loops measured in (a) longitudinal geometry and (b) with the field applied at 45° respect to the film normal of 7F sample.

The angular dependences of the coercivity for 5F and 7F films are reported in Fig. 8.10. The profile for 5F film seems to be due to the combination of the domain wall motion mode and the rotational/nucleation mode, while that of the 7F film is characterized by a behaviour typical of the domain wall motion mechanism. These behaviours confirm the strengthening of the domain wall pinning mechanism by increasing the growing temperature and suggest the disappearance of the exchange-type interactions among particles, in agreement with the presence of a more particulate morphology for 7F sample [Fig. 8.5(b)].

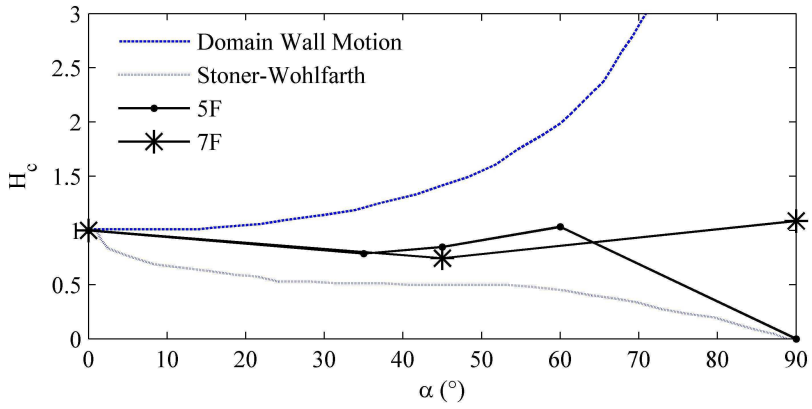

Figure 8.10 – Angular dependence of the coercivity for 5F and 7F samples. The zero angle refers to the film normal direction.

Conclusions

The activity presented in this thesis is focused on the growth and characterization of (i) thin and ultra-thin films whose ordered phase is the $L1_0$-structure and (ii) exchange-spring magnets showing a strong perpendicular anisotropy. The analyzed systems are the FePt and the FePd alloys that, grown at high temperature and around the equiatomic composition, show an order-disorder transformation followed by the appearance of a tetragonal lattice and a strong uniaxial anisotropy along the contracted *c*-axis. These alloys are suitable candidates for the development of perpendicular exchange-spring magnets.

Factors such as substrates, bufferlayers and the growing parameters become fundamental to induce a perpendicular orientation of the easy magnetization axis. Moreover the magnetic properties of these systems are strongly dependent on the type of growing technique used for the deposition. In effect, the different energies of the growing processes allow to tune the growth mode (layer by layer or 3D) and the morphology of the samples, influencing the degree of chemical order and epitaxy.

For these reasons, FePt thin films have been grown both by rf sputtering and UHV e-beam evaporation technique. The rf sputtering favours the development of high coercive films promoting a high density of defects that act as pinning sites for domain wall motion. On the contrary the e-beam evaporation technique allows to obtain hard films with a strong perpendicular anisotropy favouring a better epitaxial growth and a high degree of chemical order.

In the case of sputtered FePt films a reduction of the film thickness favours an improvement of the magnetic properties while in the evaporated samples the hardness and the anisotropy can be strengthened by increasing the film thickness. In effect, the increase of the thickness induces a morphology constituted by well decoupled nanometric grains causing a significant improvement of the magnetic hardness.

The presence of a Pt underlayer can be helpful to further enhance the magnetic hardness of these films. This type of underlayer allows to reduce the lattice mismatch between film and

substrate favouring a better epitaxial growth and contemporary increases the defect density in the alloy, in this way promoting high coercive values.

The effects of the growing temperature on the magnetic properties have also been studied. Respect to post-annealing processes, the growth at high temperature proves to be more effective for the development of ordered FePt films. This is due to the fact that the ordering is a diffusion controlled process. In effect, during the high temperature growth the ordering occurs through the surface diffusion while during the post-annealing processes the ordering takes place through volume diffusivity orders of magnitude lower than the surface one.

In the case of FePd ultra-thin films, the increase of the growing temperature induces an improvement of the magnetic properties with a strong enhancement of the perpendicular anisotropy. Surprisingly the obtained films do not show transcritical-shaped hysteresis loops as generally reported in literature, indicating that the e-beam evaporation technique and the growing parameters set during the deposition allow to obtain films with anisotropy strong enough to overcome the demagnetizing field. Moreover, of particular interest is the fact that by growing the films at 700°C very high values of the coercive field can be obtained (well above 10 kOe). If these samples are compared to similar FePt films grown at 700°C, it can be argued about the formation of a nanostructured morphology induced by the e-beam evaporation technique allowing to obtain thin films with very hard magnetic properties.

Moreover, during the Ph.D. period, FePt/Fe exchange-spring magnets grown in the form of bilayers and trilayers have been studied.

In the case of FePt/Fe bilayers, two different growing techniques have been used: the rf-sputtering for the hard layer and the e-beam evaporation technique for the soft one. The innovative use of two growing technique properly selected for the deposition of the different magnetic phases proves to be very promising for the development of well exchange-coupled spring magnets showing a single phase magnetic behaviour in spite of the presence of strong demagnetizing fields and a high soft/hard thickness ratio.

On these samples Mössbauer spectroscopy has been used to study the hard/soft interface phenomena and their influence on the strength of the exchange interaction that develops between different magnetic phases. The establishing of a strong exchange coupling interaction is linked to the degree of interface intermixing and seems to be due to the formation of a thin interfacial region, 2 nm thick, constituted by Fe and a Fe-rich FePt compound both in the form of small particles showing superparamagnetic behaviour.

In the case of FePt/Fe/FePt trilayers grown by the e-beam evaporation technique, by varying the thickness of the upper FePt layer from 1.2 to 4.8 nm it is possible to change the main mechanism controlling the coercivity. For the thinner upper layer, defects act as pinning

sites for the domain wall motion, while, with increasing the upper layer thickness, the defects become preferential sites for the nucleation of reversed domains, in this way, favouring the reversal of magnetization. This effect is due to the appearance of exchange-coupling interactions among the grains that favour a more cooperative reversal of the magnetic moments.

Moreover the thicker trilayers show a morphology constituted by elongated islands having a preferred direction of elongation. This preferred direction induces a preferred directionality in the magnetic domain configuration. The domain pattern is constituted by finely dispersed bubble domains with sizes much greater than those of the islands. For this reason, these domains belong to the family of interaction domains whose characteristics are mainly determined by the strength of the exchange-coupling interactions that develop among the grains.

Bibliography

[1] B.D. Cullity: Introduction to Magnetic Materials, Addison Wesley, Reading, Mass. 1972

[2] C. Kittel, *Revs. Mod. Phys.* **21**, 541-583 (1949)

[3] C. Kittel and J.K. Galt, *Solid State Physics* **3**, 437-565 (1956)

[4] E.C. Stoner, F.R.S. and E.P. Wohlfarth, *IEEE Trans. Magn.* **27**, 3475-3518 (1991).

[5] D. Sellmyer and D.B. Shomsky: Advanced Magnetic Nanostructures, Springer 2006

[6] H. Kronmüller, K.D. Durst, M. Sagawa, *J. Magn. Magn. Mater.* **74**, 291-302 (1988)

[7] M.T. Johnson, P.J.H. Bloemen, F.J.A. den Broeder, J.J. de Vries, *Rep. Prog. Phys.* **59**, 1409-1458 (1996)

[8] M.S. Cohen, "Ferromagnetism in films" in Thin film phenomena pp.608-711, McGraw-Hill 1969

[9] C. Kooy, U. Enz, *Philips Res. Repts.* **15**, 7-29 (1960)

[10] E.F. Kneller, R. Hawing, *IEEE Trans. Magn.* **27**, 3588-3600 (1991).

[11] D. Chumakov, R. Schäfer, D. Elefant, D. Eckert, L. Schultz, S.S. Yan, J.A. Barnard, *Phys. Rev. B* **66**, 134409(1-5) (2002)

[12] O. Hellwig, J.B. Kortright, K. Takano, E. Fullerton, *Phys. Rev. B* **62**, 11694-11698 (2000)

[13] S. David and D. Givord, *J. All. Compounds* **281**, 6-11 (1998)

[14] T. Leineweber, H. Kronmüller, *J. Magn. Magn. Mater.* **176**, 145-154 (1997)

[15] E.E. Fullerton, J.S. Jiang, M. Grimsditch, C.H. Sowers, S.D. Bader, *Phys. Rev. B* **58**, 12193-12200 (1998)

[16] T. Nagahama, K. Mibu, T. Shinjo, *J. Phys. D: Appl. Phys.* **31**, 43-49 (1998)

[17] R. Fischer, T. Leineweber, H. Kronmüller, *Phys. Rev. B* **57**, 10723-10732 (1998)

[18] M. Ohring: Materials Science of thin films, Academic Press (2001)

[19] M. Carbucicchio: "Mössbauer spectroscopy", in Physics of Metals, pp.108-138, Eds. E. S. Giuliano & C. Rizzuto, World Sci. Publ. Co. Pte. Ltd. Singapore, 1988

[20] M. Dreyer, R.D. Gomez, I.D. Mayergoyz, *IEEE Trans. Magn.* **36**, 2975-2977 (2000)

[21] H.S. Bennett, E.A. Stern, *Phys. Rev* **137**(A2), A448-A461 (1965)

[22] J.L. Erskine, E.A. Stern, *Phys. Rev. B*, **8**, 1239-1255 (1973)

[23] J.L. Erskine, E.A. Stern, *Phys. Rev. B*, **12**, 5016-5024 (1975)

[24] B.R. Cooper, *Phys. Rev*. **139** (A5), A1504-A1514 (1965)

[25] J. Zak, E.R. Moog, C. Liu, S.D. Bader, *J. Mag. Magn. Mater*. **89**, 107-123 (1990)

[26] J. Zak, E.R. Moog, C. Liu, S.D. Bader, *Phys. Rev. B* **43**, 6423-6429 (1991)

[27] J. Zak, E.R. Moog, C. Liu, S.D. Bader, *J. Mag. Magn. Mater*. **88**, L261-L266 (1990)

[28] K. Sato, *Jpn. J. Appl. Phys.* **20**, 2403-2409 (1981)

[29] W.S. Kim, M. Aderholz, W. Kleemann, *Meas. Sci. Technol.* **4**, 1275-1280 (1993)

[30] E.Th. Papaioannou, M. Angelakeris, N.K. Flevaris, P. Fumagalli, Ch. Mueller, A. Troupis, A. Spanou, V. Karoutsos, P. Poulopoulos, V. Kapaklis, C. Politis, *J. Appl. Phys.* **101**, 023913(1-6) (2007)

[31] J.U. Thiele, M.E. Best; M.F. Toney; D. Weller, *IEEE Trans. Magn.* **37**, 1271-1273 (2001)

[32] J.U. Thiele, L. Folks, M.F. Toney, D.K. Weller, *J. Appl. Phys.* **84**, 5686-5692 (1998)

[33] W.B. Zeper, F.J.A.M. Greidanus, P.F. Carcia, C.R. Fincher, *J. Appl. Phys.* **65**, 4971-4975 (1989)

[34] K. O'Grady, R.W. Chantrell, L.L. Sanders, *IEEE Trans. Magn.* **29**, 286-291 (1993)

[35] D.M. Donnet, V.G. Lewis, J.N. Chapman, K. O'Grady, H.W. Kesteren, *J. Phys. D: Appl. Phys.* **26**, 1741-1745 (1993)

[36] R.W. Chantrell, G.N. Coverdale, K. O'Grady, *J. Phys. D: Appl. Phys.* **21**, 1469-1471 (1988)

[37] A. Berger, M.R. Purfall, *J. Appl. Phys.* **85**, 4583-4585 (1999)

[38] S. Višňovský, K. Postava, T. Yamaguchi, R. Lopušník, *Appl. Opt.* **41**, 3950-3960 (2002)

[39] D. Weller, A. Moser, L. Folks, M.E. Best, W. Lee, M.F. Toney, M. Schwickert, J.U. Thiele, M.F. Doerner, *IEEE Trans. Magn.* **36**, 10-15 (2000)

[40] R.F.C. Farrow, D. Weller, R.F. Marks, M.F. Toney, S. Hom, G.R. Harp, A. Cebollada, *Appl. Phys. Lett.* **69**, 1166-1168 (1996).

[41] M.G. Kim, S.C. Shin, *J. Appl. Phys.* **90**, 2211-2215 (2001).

[42] R.A. Ristau, K. Barmak, K.R. Coffey, J.K. Howard, *J. Appl. Phys.* **86**, 4527-4533 (1999)

[43] M.F. Toney, W.Y. Lee, J.A. Hedstrom, A. Kellock, *J. Appl. Phys.* **93**, 9902-9907 (2003).

[44] Y. Endo, K. Oikawa, T. Miyazaki, O. Kitakami, Y. Shimada, *J. Appl. Phys.* **94**, 7222-7226 (2003).

[45] B. Bian, D.E. Laughlin, K. Sato, Y. Hirotsu, *IEEE Trans. Magn.* **36**, 3021-3023 (2000).

[46] P.C. McIntyre, C.J. Maggiore and M. Nastasi, *Acta Mater* **45**, 869-878 (1997).

[47] T. Shima, T. Seki, K. Takanashi, Y.K. Takahashi, K. Hono, *J. Magn. Magn. Mater.* **266**, 142-154 (2003).

[48] Y.K. Takahashi, K. Hono, T. Shima, K. Takanashi, *J. Magn. Magn. Mater.* **267**, 248-255, (2003).

[49] T. Mahalingam, J.P. Chu, J.H. Chen, C.L. Chiang, S.F. Wang, *Materials Chemistry and Physics* **82**, 335-340, (2003).

[50] A.Z. Men'shikov, Y.A. Dorofeyev, V.A. Kazantsev, S.K. Sidorov, *Fiz. Metal. Metalloved* **38**, 505-519 (1974)

[51] F. Casoli, F. Albertini, L. Pareti, S. Fabbrici, L. Nasi, C. Bocchi, R. Ciprian, *IEEE Trans. Magn.* **41**, 3223-3225 (2005).

[52] A. di Bona, C. Giovanardi, S. Valeri, *Surface Science* **498**, 193-201 (2002).

[53] K. Barmak, J. Kim, L.H. Lewis, K.R. Coffey, M.F. Toney, A.J. Kellock, J.U. Thiele, *J. Appl. Phys.* **98**, 33904(1-10) (2005)

[54] F.E. Spada, F.T. Parker, C.L. Platt, J.K. Howard, *J. Appl. Phys.* **94**, 5123-5134 (2003)

[55] P.C. McIntyre, C.J. Maggiore and M. Nastasi, *J. Appl. Phys.* **77**, 6201-6204 (1995).

[56] P.C. McIntyre, C.J. Maggiore and M. Nastasi, *Acta Mater* **45**, 879-887 (1997).

[57] J. Narayan, P. Tiwari, K. Jagannadham, O.W. Holland, *Appl. Phys. Lett.* **64**, 2093-2095 (1994).

[58] B.M. Lairson, M.R. Visokay, R. Sinclair, S. Hagstrom, B.M. Clemens, *Appl. Phys. Lett.* **61**, 1390-1392 (1992).

[59] J.F. Lawler, R. Schad, S. Jordan, H. van Kempen, *J. Magn. Magn. Mater.* **165**, 224-226 (1997).

[60] A. Cebollada, D. Weller, J. Sticht, G.R. Harp, R.F.C. Farrow, R.F. Marks, R. Savoy, J.C. Scott, *Phys. Rev. B* **50**, 3419-3422 (1994).

[61] A. Martins, M.C.A. Fantini, A.D. Santos, *J. Magn. Magn. Mater.* **265**, 13-22 (2003).

[62] M.H. Hong, K. Hono, M. Watanabe, *J. Appl. Phys.* **84**, 4403-4409 (1998).

[63] M.R. Visokay, R. Sinclair, *Appl. Phys. Lett.* **66**, 1692-1694 (1995).

[64] Y. Ide, T. Goto, K. Kikuchi, K. Watanabe, J. Onagawa, H. Yoshida, J.M. Cadogan, *J. Magn. Magn. Mater.* **177/181**, 1245-1246 (1998).

[65] M. Watanabe, M. Homma, T. Masumoto, *J. Magn. Magn. Mater.* **177**, 1231-1232 (1998).

[66] R.F.C. Farrow, D. Weller, R.F. Marks, M.F. Toney, D.J. Smith, M.R. McCartney, *J. Appl. Phys.* **84**, 934-939 (1998).

[67] B.M. Lairson, M.R. Visokay, R. Sinclair, B.M. Clemens, *Appl. Phys. Lett.* **62**, 639-641 (1993).

[68] T. Shima, T. Moriguchi, T. Seki, S. Mitani, K. Takanashi, *J. Appl. Phys.* **93**, 7238-7240 (2003).

[69] T. Seki, T. Shima, K. Takanashi, Y. Takahashi, E. Matsubara, *Appl. Phys. Lett.* **82**, 2461-2463 (2003).

[70] Y.K. Takahashi, K. Hono, *Scripta Mater.* **53**, 403-409 (2005)

[71] R. Kozubski, S. Czekaj, M. Kozłowski, E. Partyka, K. Zapała, *J. All. Comp.* **378**, 302-307 (2004)

[72] J.U. Thiele, L. Folks, M.F. Toney, D.K. Weller, *J. Appl. Phys.* **84**, 5686-5692 (1998).

[73] T. Klemmer, D. Hoydick, H. Okumura, B. Zhang, W.A. Soffa, *Scr. Metall. Mater.* **33**, 1793-1805 (1995).

[74] S. Simizu, R.T. Obermyer, B. Zande, V.K. Chandhok, A. Margolin and S.G. Sankar, *J. Appl. Phys.* **93**, 8134-8136 (2003).

[75] J. Lyubina, I. Opahle, K.H. Müller, O. Gutfleisch, M. Richter, M. Wolf, L. Schultz, *J. Phys.: Condens. Matter* **17**, 4157-4170 (2005).

[76] Y. Liu, J.P. Liu, D.J. Sellmyer, *Nanostructured Materials* **12**, 1027-1030 (1999).

[77] C.B. Rong, V. Nandwana, N. Poudyal, J.P. Liu, M.E. Kozlov, R.H. Baughman, Y. Ding, Z.L. Wang, *J. Appl. Phys.* **102**, 23908(1-7) (2007).

[78] J. Zhou, R. Skomski, X. Li, W. Tang, G.C. Hadjipanayis, D.J. Sellmyer, *IEEE Trans. Magn.* **38**, 2802-2804 (2002).

[79] C.B. Rong, H.W. Zhang, X.B. Du, J. Zhang, S.Y. Zhang, B.G. Shen, *J. Appl. Phys.* **96**, 3921-3924 (2004).

[80] Y. Gu, D. Zhang, X. Zhan, Z. Ji, Y. Zhang, *J. Magn. Magn. Mater.* **297**, 7-16 (2006).

[81] R.F. Sabiryanov, S.S. Jaswal, *J. Magn. Magn. Mater.* **177/181**, 989-990 (1998).

[82] Y.K. Takahashi, T.O. Seki, K. Hono, T. Shima, K. Takanashi, *J. Appl. Phys.* **96**, 475-481 (2004).

[83] J.M.D. Coey and R. Skomski, *Physica Scripta* **T49**, 315-321 (1993).

[84] R. Skomski, *J. Appl. Phys.* **76**, 7059-7064 (1994).

[85] M. Carbucicchio and M. Rateo, *Hyperf. Interact.* **156/157**, 581-593 (2004).

[86] F. Casoli, F. Albertini, S. Fabbrici, C. Bocchi, L. Nasi, R. Ciprian, L. Pareti, *IEEE Trans. Magn.* **41**, 3877-3879 (2005).

[87] M. Carbucicchio, C. Grazzi, L. Lanotte, M. Rateo, G. Ruggiero, G. Turilli, *Hyperf. Interact.* **139/140**, 553-559 (2002).

[88] M. Carbucicchio, M. Rateo, *Hyperf. Interact.* **141/142**, 441-446 (2002).

[89] M. Carbucicchio, S. Bennett, F. J. Berry, M. Prezioso, M. Rateo, G. Turilli, *J. Appl. Phys.* **93**, 7631-7633 (2003).

[90] J.A. Christodoulides, M.J. Bonder, Y. Huang, S. Stoyanov, G.C. Hadjipanayis, A. Simopoulos, D. Weller, *Phys. Rev. B* **68**, 054428(1-7) (2003)

[91] M. Tilbrook: Mössbauer and Magnetisation Measurements of FePt Nanoparticles for Magnetic Recording Media Department of Physics, Thesis, University of Western Australia, 2000

[92] K. Potzger, H. Reuther, S. Zhou, A. Mücklich, R. Grötzschel, F. Eichhorn, M.O. Liedke, J. Fassbender, H. Lichte, A. Lenk, *J. Appl. Phys.* **99**, 08N701(1-3) (2006)

[93] C. Clavero, J.M. García-Martín, J.L. Costa Krämer, G. Armelles, A. Cebollada, Y. Huttel, R.A. Lukaszew, A.J. Kellock, *Phys. Rev. B* **73**, 174405(1-10) (2006)

[94] P. Kamp, M. Belakhovski, C. Boeglin, H.A. Dürr, G. van der Laan, P. Schille, A. Rogalev, J. Goulon, V. Gehanno, A. Marty, B. Gilles, *Phys. B* **248**, 127-132 (1998)

[95] O. Klein, Y. Samson, A. Marty, S. Guillous, M. Viret, C. Fermon, H. Alloul, *J. Appl. Phys*. **89**, 6781-6783 (2001)

[96] P. Kamp, A. Marty, B. Gilles, R. Hoffmann, S. Marchesini, M. Belakhovski, C. Boeglin, H.A. Dürr, S.S. Dhesi, G. van der Laan, A. Rogalev, *Phys. Rev. B* **59**, 1105-1112 (1999)

[97] H. Naganuma, K. Sato, Y. Hirotsu, *J. Magn. Magn. Mater*. **310**, 2356-2358 (2006)

[98] Ch. Issro, W. Püschl, W. Pfeiler, P.F. Rogl, W.A. Soffa, M. Acosta, G. Schmerber, R. Kozubski, V. Pierron-Bohnes, *Scripta Mater*. **53**, 447-452 (2005)

Publications

- M. Carbucicchio, R. Ciprian, G. Palombarini: “On the phenomena occurring at the interface between iron and iron–platinum thin films”, *Hyper. Interact.* **185**, 1-7 (2008)

- M. Carbucicchio, R. Ciprian, G. Palombarini: “Morphological and microstructural study of $L1_0$-ordered FePt and $L1_0$-FePt/Fe ultrathin films grown by UHV e-beam evaporation technique”, submitted to *J. Magn. Magn. Mater.* (2008)

- M. Carbucicchio, R. Ciprian, G. Turilli: “Exchange-spring magnets based on $L1_0$-FePt ordered phase”, submitted to *Hyper. Interact.* (2008)

- G. Sambogna, G. Palombarini, M. Carbucicchio, R. Ciprian: “Borosiliciding of Fe-Ni alloys and evaluation of their resistance to abrasive wear”, *Hyper. Interact.* **187**, 131-136 (2008)

- G. Palombarini, A. Casagrande, M. Carbucicchio, R. Ciprian: “Protection against corrosion of iron alloys by aluminized coatings produced using two different processes”, *Hyper. Interact.* **187**, 125-130 (2008)

- M. Carbucicchio, R. Ciprian, F. Ospitali, G. Palombarini: “Morphology and phase composition of corrosion products formed at the zinc–iron interface of a galvanized steel”, *Corros. Sci.* **50**, 2605-2613 (2008)

- G. Palombarini, M. Carbucicchio, G. Sambogna, R. Ciprian: “Formation and characterization of boride coatings thermochemically grown on the $Fe_{64}Ni_{36}$ alloy”, submitted to *Hyper. Interact.* (2008)

- M. Carbucicchio, G. Palombarini, S. Tosto, M. Rateo, G. Sambogna, R. Ciprian: “Interfacial microstructure and properties of dissimilar steels joined by high energy beam melting processes”, submitted to *Hyper. Interact.* (2008)

- R. Ciprian, M. Carbucicchio, F. Fermi: “Lossless compression methods for spectral images”, submitted to *Color Res. Appl.* (2008)

- F. Casoli, F. Albertini, L. Pareti, S. Fabbrici, L. Nasi, C. Bocchi, R. Ciprian: “Growth and characterization of epitaxial FePt films”, *IEEE Trans. Magn.* **41**, 3223-3225, 2005

- F. Casoli, F. Albertini, S. Fabbrici, C. Bocchi, L. Nasi, R. Ciprian, L. Pareti: “Exchange-coupled FePt/Fe bilayers with perpendicular magnetization”, *IEEE Trans. Magn.* **41**, 3877-3879, 2005

Acknowledgements

Prima di tutti, ringrazio il mio supervisore Massimo Carbucicchio, per il suo indispensabile supporto, per avermi incoraggiata e stimolata, aiutandomi senza limitare la mia indipendenza.

Vorrei ringraziare tutti gli amici e colleghi che hanno condiviso con me questa esperienza. Li ringrazio per i momenti di relax e per aver riportato il buon umore in giornate “nuvolose”.

Ringrazio anche tutte quelle persone che hanno contribuito scientificamente al lavoro svolto durante questo dottorato chiarendo i miei dubbi e supportandomi.

Ringrazio anche tutti gli amici della Sezione di Chimica, Esplosivi ed Infiammabili del RIS che hanno accompagnato quest’avventura ricordandomi sempre di “crederci”. Grazie della vostra amicizia.

Ringrazio la mia famiglia semplicemente perché mi sopporta, supportandomi in scelte che a volte non condividono.